Mathematical models of light transport in biological tissues for quantitative clinical diagnostic applications

by

Robert H. Wilson

A dissertation submitted in partial fulfillment
of the requirements for the degree of
Doctor of Philosophy
(Applied Physics)
in The University of Michigan
2012

Doctoral Committee:

Professor Mary-Ann Mycek, Chair
Professor Michael D. Morris
Professor James M. Scheiman
Professor John C. Schotland

Acknowledgements

I would like to thank all of the people who have helped and supported me during my time as a graduate student. I thank my advisor Prof. Mary-Ann Mycek for giving me the opportunity to pursue my Ph. D. in her research group. I also thank all of the members of my dissertation defense committee, candidacy exam committee, and research group, as well as all of our collaborators, for making it possible for me to reach this point: Prof. Michael Morris, Prof. James Scheiman, Prof. John Schotland, Prof. Barbara McKenna, Prof. Diane Simeone, Prof. Jeremy Taylor, Prof. Anita Mahadevan-Jansen, Prof. Steven Goldstein, Prof. Stephen Feinberg, Prof. Zhen Xu, Dr. Karthik Vishwanath, Dr. Malavika Chandra, Dr. Ching-Wei Chang, Dr. Dhruv Sud, Dr. Matthew Keller, Dr. Mekhala Raghavan, Dr. Julianne Purdy, Oliver Lee, Bill Lloyd, Leng-Chun Chen, Seung Yup Lee, Emma Salomonsson, Kehan Zhang, and Viola Schweller. I thank Prof. Brad Orr, Cynthia McNabb, Charles Sutton, and all of my classmates from the Applied Physics Program for their support during my time in graduate school. In addition, I thank all of the organizations whose funding made it possible for me to pursue my graduate research. These funding acknowledgements are listed separately at the end of the dissertation.

Finally, I would like to give a special thank-you to all of my friends and family, especially my mother, father, sister, and grandparents. Thank you for all of your support.

Table of Contents

List of Figures

List of Tables

Abstract

This dissertation focuses on the development and implementation of several novel mathematical models of light transport in biological tissue for use as quantitative diagnostic tools to assess tissue viability and detect diseased tissue. This work includes semi-empirical models of reflectance and fluorescence for pancreatic cancer diagnostics, computational models of inelastic (Raman) scattering in layered tissues for non-invasive bone tissue assessment and breast tumor margin detection during surgery, and computational models of light propagation for tissues with irregular geometries.

A novel photon-tissue interaction (PTI) model of reflectance and fluorescence was developed and employed to extract biophysically-relevant tissue parameters (mean size of cell nuclei, percentage contribution of collagen to fluorescence) from measured optical spectra of freshly-excised human pancreatic tissues. The mean cellular nuclear size was statistically significant for distinguishing adenocarcinoma sites from non-cancerous (pancreatitis and normal) sites. The percentage contribution of collagen was statistically significant for distinguishing between all three tissue types included in the study (adenocarcinoma, pancreatitis, normal). When these parameters were included in a statistically-rigorous tissue classification algorithm that accounted for intra-patient correlations in the data, adenocarcinoma was distinguished from the non-cancerous tissues with an area of 0.906 under the receiver operating characteristic (ROC) curve and

a sensitivity, specificity, positive predictive value, and negative predictive value of 87.5%, 89.0%, 77.8%, and 94.2%, respectively.

A novel Monte Carlo (MC) model of inelastic (Raman) scattering in layered tissues was developed and employed to characterize the effects of tissue and fiber-probe properties on the detected Raman signal. This MC model was employed to assist with two biomedical applications: bone tissue diagnostics and breast tumor margin assessment. For the tumor margin assessment application, it was predicted that the smallest detectable tumor thickness using spatially-offset Raman spectroscopy would be 100 microns under a 0.5 mm margin or 1 mm under a 2 mm margin.

The models described in this dissertation provide accurate, versatile, and quantitative analysis of the effects of fiber-optic probe design and biophysical tissue properties on the detected optical signal and can be employed in a wide range of tissue diagnostic applications.

Chapter 1

Introduction

1.1 Optical spectroscopy of biological tissues

Methods involving the use of visible light to probe the structure and function of human tissue have become increasingly prevalent over the past two decades [1, 2]. One main application area for these optical techniques is cancer diagnostics, where reflectance and fluorescence spectroscopies have shown potential to assist with the detection of cancer in human tissue [3-27].

In a typical tissue reflectance spectroscopy measurement, white light is delivered to tissue via an optical fiber, the light undergoes a series of elastic scattering events [16], and the backscattered or diffusely scattered light is detected with one or more fibers and sent to a spectrometer or spectrograph to produce a wavelength-resolved reflectance spectrum [28, 29]. Reflectance measurements typically yield information about the sources of absorption and scattering in the tissue [5, 10]. The principal absorbers of visible light in human tissue are oxygenated and deoxygenated hemoglobin [5, 30], beta-carotene [9], and melanin (in skin) [31]. Scattering of visible light by human tissue is largely attributed to collagen fibers and sub-cellular organelles [32, 33].

For fluorescence spectroscopy, light of a specific wavelength is delivered to tissue and when this light is absorbed, it may excite endogenous molecules known as fluorophores, which then re-emit the light as fluorescence at a longer wavelength [34]. The re-emitted light that returns to the tissue surface is detected by one or more optical fibers and sent to a spectrometer or spectrograph to produce a wavelength-resolved fluorescence spectrum [9, 28, 35]. The remitted fluorescence can also be time-resolved [36, 37], or measured as a combination of wavelength- and time-resolved data [38]. Fluorescence measurements provide information about the relative concentrations of endogenous tissue fluorophores such as collagen, keratin, elastin, retinol, NADH, and FAD [7-10].

Raman spectroscopy detects photons that have been inelastically scattered. Inelastic, or Raman, scattering refers to the process in which the scattered photons are shifted in energy and wavelength from the incident photons. The difference in energy corresponds to a molecular vibration of a component of the specimen [39]. The observed change in photon energy (i.e. optical frequency) and wavelength is specific to the molecular vibration from which the photon was Raman-scattered [39].

1.2 Mathematical models assist with disease diagnostics

When disease is present in tissue, the absorption, scattering, fluorescence, and Raman scattering properties often undergo significant changes due to alterations in tissue composition, vasculature, morphology, and metabolic function. Accurate mathematical models of optical spectroscopy processes can be highly useful for disease diagnostics in human tissue, because they provide a means of extracting quantitative values of

biologically-relevant parameters from noninvasive optical spectroscopy measurements [5-10].

Over the past two decades, a variety of mathematical methods have been employed to model human tissue reflectance and fluorescence spectra in terms of biologically significant parameters [5, 8-10]. These methods include the diffusion approximation (DA) [5], Monte Carlo (MC) simulations [8], semi-empirical models [10], photon migration models [9], and look-up table algorithms [40]. This dissertation will primarily focus on the application of a semi-empirical model for pancreatic cancer diagnosis and Monte Carlo models of fluorescence and Raman scattering for disease diagnostics in bone tissue, breast tissue, and tissue-engineered constructs. The DA will be discussed in this introduction for completeness.

A number of studies have used DA or MC models of reflectance from human tissues to extract optical parameters relevant to cancer diagnostics [5, 23, 25, 41-46]. In these studies, the tissue is often approximated as a homogeneous slab of infinite extent in the *x*- and *y*- directions (with thickness *d* in the *z*-direction and uniform optical absorption and scattering coefficients (μ_a, μ_s) throughout the medium (Figure 1.1)), or as a stack of homogeneous slabs. Photons that undergo many scattering events (solid line) can be treated as diffuse, but photons that only undergo a few scattering events (dashed line) cannot be treated as diffuse [47, 48]. The thickness *d* is usually assumed to be much larger than the penetration depth of the light into the tissue, thereby neglecting

transmittance. In this case, the reflectance model will typically be a function of μ_a, μ_s, and the source-detector separation ρ of the fiber-optic probe.

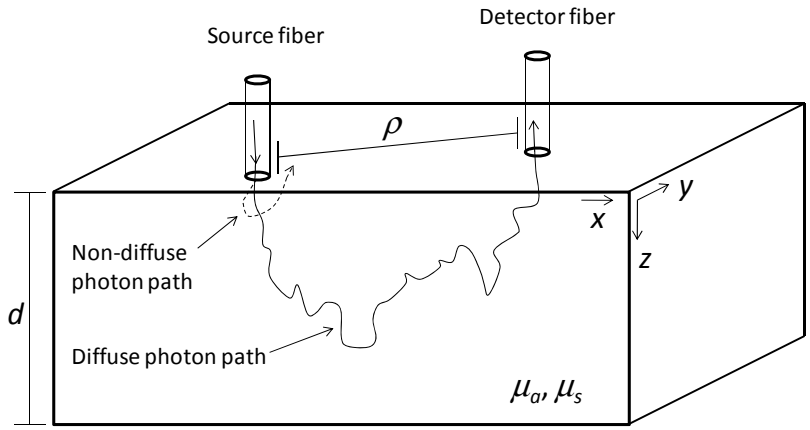

Figure 1.1 Typical homogeneous tissue model used in biomedical optics [3]. The tissue is represented as a slab with absorption and scattering coefficients μ_a and μ_s. Photons are launched into the tissue via the source fiber, and they are collected by the detector fiber at a distance ρ from the source. Photons that undergo many scattering events can be treated as diffuse (solid line), but photons that only undergo a few scattering events (dashed line) cannot be treated as diffuse. Here, the diffuse photon path (solid line) is detected and the non-diffuse photon path (dashed line) is not detected.

When the model is fit to a measured reflectance spectrum $R(\lambda)$ acquired with a fiber-optic probe with source-detector separation ρ, the absorption and scattering coefficients μ_a and μ_s of the tissue can be determined. From the absorption coefficient, the concentrations of the principal absorbers in the tissue (such as oxy-hemoglobin, deoxy-hemoglobin, beta-carotene, and retinol) can be determined. The blood-oxygen saturation of the tissue can be determined by dividing the oxy-hemoglobin concentration by the total hemoglobin concentration [5]. The scattering coefficient, the concentration and mean size of the scatterers in the tissue can be determined from Mie theory [49], either by a power-law approximation of the form $\mu_s(\lambda) = A\lambda^{-b}$ [9, 50], or by the Van de Hulst approximation

[32, 51]. In the power-law approximation, the parameter A is related to the concentration of the scatterers [9], and the parameter b is related to the scatterer size [52]. Both equations are based on the assumption that the scattering particles in the tissue are spherical; to model scattering from collagen fibers, a term for cylindrical scatterers can be added [33]. Recent work has also been done to model scattering from spheroidal cell nuclei [53]. The absorption and scattering parameters extracted from a reflectance model can subsequently be put into a classification algorithm to distinguish between different tissue types [9].

DA and MC models of fluorescence have also been employed for cancer diagnostics in human tissues [7, 54-58]. The main goal of the fluorescence models is to extract the relative concentrations of intracellular and extracellular tissue components that provide information about tissue morphology and metabolism. For excitation in the near-UV and visible regions of the electromagnetic spectrum, the predominant tissue components that fluoresce are collagen, elastin, keratin, NADH, FAD, tryptophan, porphyrins, and retinol [7-9, 32]. Measured fluorescence spectra $F(\lambda)$ of human tissues are often modeled as a linear combinations of the spectra of the individual fluorophores in the tissue [32, 50]. The best fit of the model to the measured fluorescence spectrum extracts the relative contribution of each tissue fluorophores to the tissue fluorescence. The spectra of the individual fluorophores can be measured in advance, so that they are known when the model is fit to the measured tissue fluorescence spectrum. However, since the measurements of individual fluorophores are typically performed on samples that are not within the same biochemical environment as human tissue, the spectra may have to be

shifted or corrected [9]. Furthermore, the measured tissue fluorescence spectrum contains artifacts from absorption and scattering; these artifacts are typically removed to produce an "intrinsic" fluorescence spectrum [32], or a fluorescence model that corrects for them is developed [59].

The diffusion approximation (DA) [48, 60-65] provides an analytical solution to the radiative transfer equation for simple geometries in the limits that the absorption of the tissue is negligible compared to the scattering and that the delivery and detection of light occur far enough apart (in space and in time) that the photon trajectories can be treated as diffuse (see Figure 1.1). Higher-order versions of the DA (such as the P_3 and P_N approximations [66, 67] offer increased accuracy for short source-detector separations; however, the mathematical expressions are more complicated. In the forward DA model, the measured reflectance, as a function of wavelength λ and distance ρ between the source and detector fibers, can be modeled with the equation [5, 61]:

$$R(\lambda,\rho) = \frac{z_o}{4\pi}\frac{\mu_s'}{\mu_s' + \mu_a}\left[\left(\mu + \frac{1}{r_1}\right)\frac{e^{-\mu r_1}}{r_1^2} + \left(1 + \frac{4}{3}A\right)\left(\mu + \frac{1}{r_2}\right)\frac{e^{-\mu r_2}}{r_2^2}\right]. \quad (1)$$

In Eq. (1), $z_o = (\mu_a + \mu_s')^{-1}$, $\mu = [3\mu_a(\mu_a + \mu_s')]^{1/2}$, $r_1 = (z_o^2 + \rho^2)^{1/2}$, and $r_2 = [z_o^2(1 + (4A/3))^2 + \rho^2]^{1/2}$. The parameter A is a function of the tissue refractive index n; for biological tissue, n is typically approximated to be 1.4, which gives a value of around 3.2 for A [5]. By fitting Eq. (1) to a measured reflectance spectrum $R(\lambda)$ acquired with a fiber-optic probe with source-detector separation ρ, the absorption and reduced scattering coefficients μ_a and μ_s' of the tissue can be extracted. In order to obtain the scattering

coefficient μ_s, the reduced scattering coefficient μ_s' must be divided by (1 - *g*), where *g* is the anisotropy (a quantity related to the directionality of the scattering) and is often approximated as 0.9 for biological tissue [37].

A number of studies have employed inverse DA models of reflectance in the aforementioned manner to extract biologically-relevant parameters for classification of benign and malignant human tissues *in vivo*. Zonios *et al.* [5] conducted a study of this type on colon tissue *in vivo* for patients undergoing colonoscopy. In this study, reflectance spectra were acquired from adenomatous (pre-cancerous) colon polyps and normal colon tissue from 13 patients. A homogeneous-slab DA model was fit to the measured reflectance spectra, and the total hemoglobin concentration, blood-oxygen saturation, scatterer concentration, and scatterer size were extracted from the best fits. Georgakoudi *et al.* [23] performed a similar study for esophageal tissue, in which reflectance spectra were acquired *in vivo* from patients just prior to biopsy. All of the 16 patients in the study had a condition known as Barrett's esophagus; many cases of lower esophageal adenocarcinoma originate in patients with this condition. The measured reflectance spectra were fit to a homogeneous-slab DA model to extract the tissue absorption and scattering coefficients. At a wavelength of 400 nm, the mean reduced scattering coefficient was found to be 28% lower in high-grade dysplasia than in low-grade dysplasia, and the mean reduced scattering coefficient of low-grade dysplasia was found to be 40% lower than that of non-dysplastic Barrett's esophagus. Inverse diffusion models of reflectance have also been employed to extract reduced scattering coefficients

in vivo from human cervical tissues [25] and to extract hemoglobin concentration and blood-oxygen saturation values *in vivo* from human colon tissues [30].

Although DA models are commonly employed for analysis of reflectance spectra, they are inaccurate in situations where the photon paths cannot be approximated as diffuse. This can occur when the distance ρ between the source and detector fibers is less than $1/\mu_s$' [68] and when the tissue absorption is non-negligible compared to the scattering [69]. In these cases, a modified equation for the reflectance must be used in order to maintain the accuracy of the model. Several groups have developed such expressions and applied them to cancer diagnostics in human tissues. Garofalakis *et al.* [70] used an improved homogeneous-slab diffusion equation that was applicable to small tissue geometries, and employed the inverse model in an *ex vivo* study to distinguish between normal and cancerous breast tissues. Fawzy *et al.* [71] used a bi-layered diffusion model to describe the reflectance from photons that spent a significant amount of time in a superficial tissue layer, and applied the inverse model to distinguish malignant from benign lung tissue in an *in vivo* study. These results suggest that modified diffusion models have the potential to accurately describe tissue reflectance spectra with analytical equations in situations where the commonly-used DA models are inaccurate.

Inverse DA models of fluorescence have been employed for cancer diagnostics of human tissues. Nair *et al.* [55] used an inverse DA model of spatially-resolved fluorescence in a homogeneous medium to distinguish between normal breast tissue, benign breast tumors, and malignant breast tumors in an *ex vivo* human study. Chang *et al.* [7, 35, 54] employed

a two-layered inverse fluorescence model in which the DA was used to model fluorescence in the bottom layer, for distinguishing between normal tissue and pre-cancer *in vivo* in the human cervix. In [7], normal and dysplastic cervical tissues from 292 patients were interrogated *in vivo* to obtain a total of 493 fluorescence spectra. Best fits of the model developed in [54] provided information about relative concentrations of keratin, NADH, FAD, enzymatically activated collagen crosslinks, and glycosylation-activated collagen crosslinks in the tissues.

Monte Carlo (MC) simulations are frequently used in biomedical optics because they are considered to be the "gold standard" for accurately modeling photon propagation in biological tissues with a wide range of tissue optical properties and fiber-probe geometries [37, 72-82]. The accuracy of MC simulations is due to the fact that the MC method treats the path of each individual photon in the tissue independently and then combines the results at the end of the simulation to obtain expressions for the total detected reflectance or fluorescence as a function of space and/or time. The drawback to this technique is that it requires large numbers of photons (roughly 10^7 to 10^8) to be simulated, and therefore can often require high computation times. The computation time becomes an especially significant drawback for simulations involving tissues with high scattering and low absorption coefficients. Recently, advances in computing technology, such as the use of graphics processing units (GPUs), have shown great potential for significantly decreasing the computation time required for MC simulations [83-85]. Semi-analytical "scaling" methods [86-89] have also been employed to reduce

computation time. Thus, MC simulations have the potential to provide rapid and accurate quantitative models of photon propagation in biological tissues.

In forward MC simulations (Figure 1.2) tissues are typically modeled as stacks of homogeneous slabs, with each slab having a different absorption coefficient, scattering coefficient, and anisotropy [37, 75-77]. For each step of a given photon path, a probability distribution function involving the scattering coefficient is sampled to obtain the distance that the photon travels on that particular step [37, 75-77]. A probability distribution function involving the anisotropy and tissue phase function is sampled to obtain the angle at which the photon will scatter during that step [37, 75-77]. To model absorption, all photons typically enter the tissue with a "weight" of 1, which is then attenuated at each step according to the Beer-Lambert Law [37, 75-77]. For fluorescence simulations, the absorption of a photon by a fluorophore is determined by sampling another probability distribution involving the fluorophore absorption coefficient μ_{afx} in the tissue layer in which the photon is located [37, 76, 77]. Since the absorption coefficient, scattering coefficient, and anisotropy are wavelength-dependent, MC reflectance simulations are usually run for one specific wavelength at a time. MC fluorescence simulations are typically run for a discrete set of wavelengths including only the wavelength of the incident laser light and the peak emission wavelength of each fluorophore. However, recent work has been done to use the MC technique to simulate entire spectra at once [90].

Inverse MC simulations involving both homogeneous and layered tissues have been employed to model reflectance for cancer diagnostic applications in human tissues. Palmer *et al.* [43] and Zhu *et al.* [91] employed a MC model of reflectance from a homogeneous slab to extract optical properties for distinguishing between malignant and benign human breast tissues *ex vivo*. Reflectance measurements from 85 tissue samples (50 benign, 35 malignant) were analyzed with the MC model to extract beta-carotene concentration, hemoglobin concentration, blood-oxygen saturation, and mean reduced scattering coefficient. The beta-carotene concentration, hemoglobin concentration, and mean reduced scattering coefficient were all statistically significant ($p < 0.05$) for distinguishing between malignant and benign tissues. The sensitivity and specificity of the MC-based classification algorithm were comparable to those of a partial least-squares technique [91]. Chang *et al.* [44] employed a MC reflectance model with homogeneous slab geometry for diagnosing pre-cancers *in vivo* in the human cervix. Salomatina *et al.* [45] used a homogeneous MC reflectance model for skin cancer diagnostics in an *ex vivo* study. Arifler *et al.* [46] employed MC simulations of reflectance in a bi-layered tissue model to analyze the reflectance from the epithelium and stroma of the human cervix for an *in vivo* study to distinguish severe dysplasia and carcinoma (47 sites, 42 patients) from normal tissue (129 sites, 115 patients).

Inverse MC simulations of fluorescence have also been used for cancer diagnostics in human tissues. Drezek *et al.* [56] employed a MC model of fluorescence in layered slab geometry to distinguish between squamous epithelial lesions and normal tissue in an *in vivo* study in the cervix. Pavlova *et al.* [57, 58] used layered MC models to distinguish

between pre-cancerous, neoplastic, and normal oral tissue *in vivo*. Vishwanath and Mycek [37] developed layered MC simulations to characterize the effect of tissue and probe properties on the time-resolved fluorescence measured *in vivo* from normal and pre-cancerous human colon tissues . As these studies demonstrate, MC simulations are a powerful tool for modeling fluorescence in layered tissues because they enable quantitative description of light transport in complex media with multiple layers and different principal fluorophores in each layer.

DA and MC models are also frequently employed to correct fluorescence spectra for artifacts related to tissue absorption and scattering. As mentioned previously, the main goal of fluorescence modeling is to extract the relative concentrations of each tissue fluorophore, but the presence of absorption and scattering artifacts in the measured fluorescence spectra complicates this process. Therefore, it is common to take the extracted tissue absorption and scattering coefficients from a reflectance model and use those properties in a model that either directly "corrects" the fluorescence spectra (such as a semi-empirical model) or implicitly accounts for attenuation (such as a MC model). DA models of fluorescence can incorporate the absorption coefficient, scattering coefficient, and anisotropy of the tissue into the fluorescence equations to explicitly account for attenuation. In MC models, the tissue absorption and scattering properties are used as inputs to the code, so that the fluorescence detected in the code has already been corrected for attenuation. For semi-empirical models, a Beer-Lambert factor of the form $exp(-(\mu_a+\mu_s')\langle L\rangle)$, where $\langle L\rangle$ is the average total path length of a fluorescence photon in the tissue, can be employed to correct the measured fluorescence for attenuation.

In an *ex vivo* study of human breast tissues (17 patients, 104 sites, 202 spectra), Volynskaya *et al.* [9] used a homogeneous-slab DA model of reflectance to extract tissue scattering parameters (*A* and *b* from the equation $\mu_s' = A\lambda^{-b}$) and relative contributions of oxy-hemoglobin and beta-carotene to the tissue absorption. These parameters were then employed to correct the measured fluorescence for attenuation. The resulting intrinsic fluorescence spectra were modeled to extract relative contributions of NADH and a "collagen-like" fluorophore. All of the extracted reflectance and fluorescence parameters except for *b* were statistically significant for distinguishing between tissue types. Zhu *et al.* [8, 92] employed homogeneous-slab MC models of both reflectance and fluorescence in an *ex vivo* study to distinguish malignant from non-malignant breast tissue. The inverse MC reflectance model was employed to extract absorption and scattering properties of the tissue, and these parameters were then input into the MC fluorescence model to account for attenuation artifacts in the measured fluorescence spectra. The parameters extracted from the inverse reflectance and fluorescence MC models were then employed for tissue classification. Redden Weber *et al.* [59] used MC and diffusion models for analysis of 748 *in vivo* reflectance and fluorescence measurements of human cervical tissue. A bi-layered MC model was employed to determine that the detected reflectance was primarily from the stromal layer, so a homogeneous P_3-hybrid diffusion model (developed in [66]) was used for analysis of reflectance data. The stromal absorption and scattering coefficients extracted from the reflectance model were then input into an analytical fluorescence model to determine the fluorophore concentrations and epithelial scattering coefficient. The extracted parameters were employed to distinguish between

several types of normal cervical tissue, grade 2 cervical intraepithelial neoplasia, and grade 3 cervical intraepithelial neoplasia and cancer.

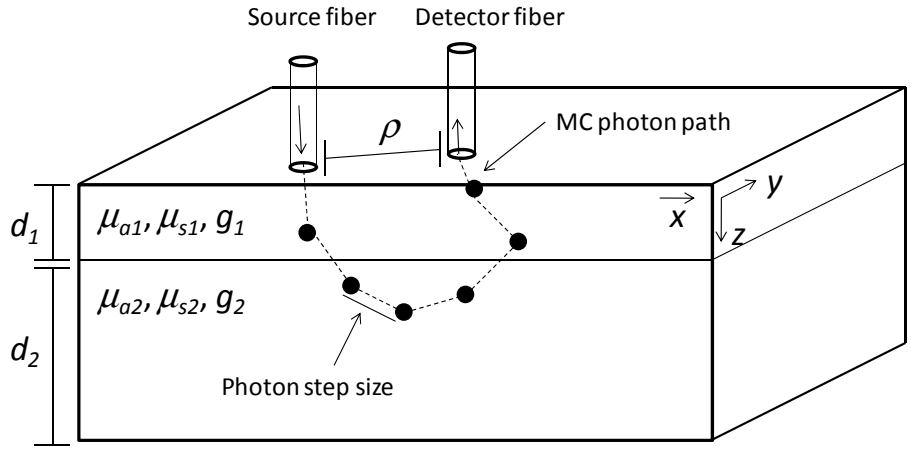

Figure 1.2 Monte Carlo (MC) model of photon propagation in tissue [3]. The tissue is typically modeled as a stack of homogeneous slabs, with each slab having its own optical properties (μ_a, μ_s, g) and thickness (d). The photon's path is modeled as a series of scattering steps with step size and scattering angle sampled from probability distributions.

In addition, several groups have recently developed semi-empirical models to extract absorption and scattering parameters from reflectance measurements on human tissue. These models typically have two main characteristics: they are simple analytical functions of the tissue absorption and scattering coefficients, and they implicitly account for the geometry of the fiber-optic probe. The combination of these two features makes semi-empirical models useful, because they can be more accurate than DA models while avoiding the long runtimes associated with MC simulations.

Reif *et al.* [93] developed a forward semi-empirical model of reflectance from a homogeneous tissue slab, for use with small source-detector separations, and used the inverse model to study the effect of probe pressure on reflectance measurements acquired

in vivo from the thigh muscles of mice [52]. The forward model was based on three assumptions: (i) the reflectance is proportional to the reduced scattering coefficient, (ii) the attenuation of the reflectance can be described by a Beer-Lambert factor ($exp(-\mu_a<L>)$, where $<L>$ is the mean total path length of a photon in the tissue) and (iii) the mean total path length $<L>$ of a photon in the tissue is inversely proportional to both the absorption coefficient and the reduced scattering coefficient. The resulting semi-empirical reflectance equation is:

$$R_{emp}(\lambda) = a\mu_s'(\lambda)\exp\left[-C_{corr}\mu_a(\lambda)\frac{b}{\left[C_{corr}\mu_a(\lambda)\mu_s'(\lambda)\right]^c}\right]. \quad (2)$$

In Eq. (2), the factor C_{corr} accounts for the confinement of blood into cylindrical blood vessels. The values of a, b, and c are related to the properties of the fiber-optic probe and can be determined from MC simulations or reflectance measurements on tissue phantoms.

Zonios and Dimou [69] developed a forward semi-empirical model of reflectance from a homogeneous tissue and used the inverse model to extract absorption and scattering properties of normal skin and melanocytic nevi from *in vivo* reflectance measurements. Marchesini *et al.* [94] employed an inverse semi-empirical, homogeneous-slab model to assess the melanin content of skin lesions (including 288 melanomas and 424 dysplastic nevi) from multispectral images acquired *in vivo*.

Inverse semi-empirical models of reflectance and fluorescence have been developed for cancer detection in human pancreatic tissues [10, 32]. In order to study the reflectance

and fluorescence spectra of human pancreatic tissues, a photon-tissue interaction (PTI) algorithm was developed by Wilson *et al.* [10, 32]. The PTI algorithm, which will be described in detail in Chapter 2, mathematically modeled the measured reflectance and fluorescence spectra to extract biophysically-relevant parameters related to tissue morphology and biochemistry from normal pancreatic tissue, chronic pancreatitis, and adenocarcinoma.

Since each of the models described in this dissertation is based on a different set of assumptions, it is important to consider the limits of validity of the model being used. Figure 1.3 shows a comparison between DA and MC models of spatially-resolved reflectance for two different scattering coefficients within a range expected [37, 69] for human tissue. In these simulations, the absorption coefficient was 0.1 cm^{-1}, the anisotropy was 0.9, the photons were launched perpendicular to the tissue surface, and all photons within a numerical aperture of 1.0 that reached the surface at a distance of less than or equal to 3.05 cm from the source were detected. The photons were binned in detector annuli of 1 mm thickness, except for the first detector, which was a circle of radius 0.5 mm. When the scattering coefficient of the tissue is 280 cm^{-1}, the DA and MC models agree well (mean error < 4%, maximum error < 15%) for all source-detector separations (Figures 1.3(a) and 1.3(c)). When the scattering coefficient of the tissue is significantly lower (75 cm^{-1}), the two models agree well (mean error < 3%, maximum error < 13%) for source-detector separations of 3mm and greater, but there is significant discrepancy (mean error > 38%) between the two models for source-detector separations of less than 3 mm (Figures 1.3(b) and 1.3(d)). This difference in agreement arises from the fact that when the tissue scattering coefficient is higher, the photon undergoes more scattering

events over a given distance, thereby causing the paths of the photons to become diffuse over a relatively short length scale. When the scattering coefficient is lower, the photon undergoes fewer scattering events over that same distance, so it is only valid to employ the DA if the length scale is increased to the point where the photon paths can once again be approximated as diffuse. Therefore, it is important to carefully consider the validity of the DA for the specific probe geometry employed in a given study, especially when using a DA model to extract quantitative values of tissue parameters. In general, the DA is valid when the source-detector separation of the fiber-probe is greater than $1/\mu_s'$ [68]. By contrast, MC simulations are valid for any set of tissue and probe properties (although they are limited by large computation times). Semi-empirical models are valid as long as they have been appropriately calibrated (using either MC simulations or measurements on tissue-simulating phantoms) for the tissue and probe properties of interest [93].

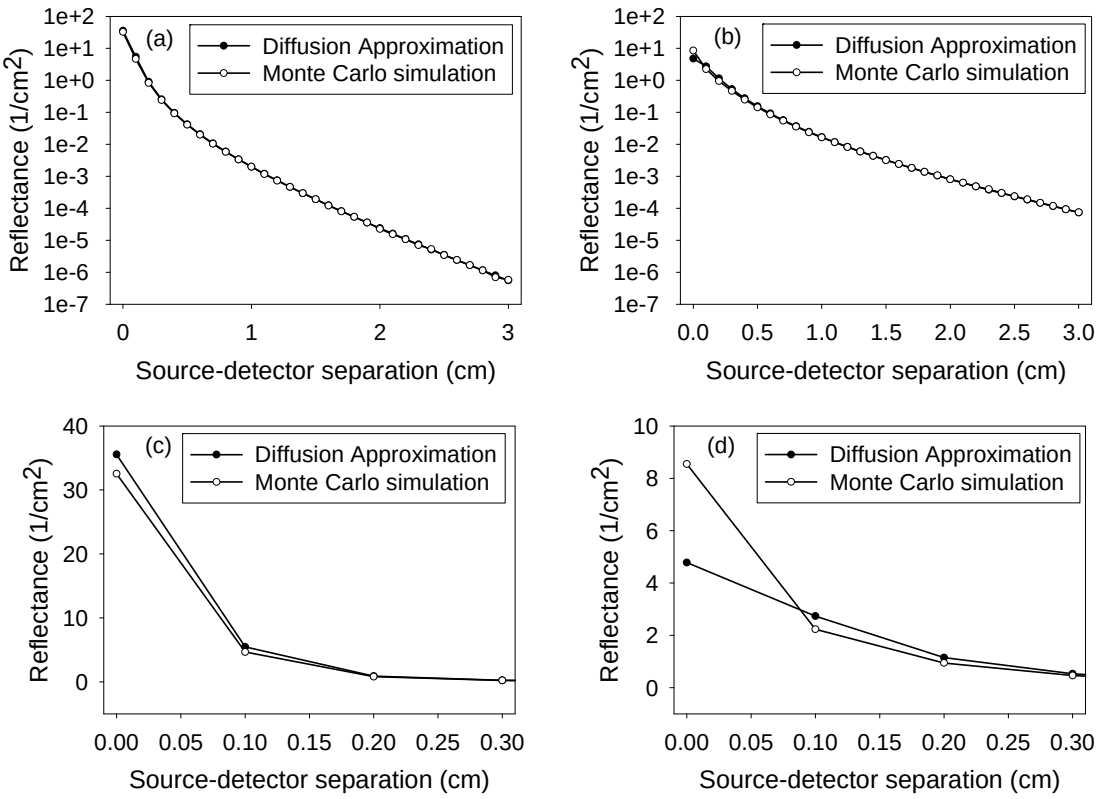

Figure 1.3 Reflectance as a function of probe source-detector separation [3], modeled with the diffusion approximation (black circles) and Monte Carlo simulations (white circles) for tissues with scattering coefficients of (a,c) μ_s = 280 cm^{-1} and (b,d) μ_s = 75 cm^{-1}. Panels (c) and (d) are magnified versions of (a) and (b) for short source-detector separations. For the tissue scattering coefficient of 75 cm^{-1}, there is notable disagreement between the two models at source-detector separations of less than 3 mm (d).

1.3 Dissertation objectives

Now that the different types of commonly-used mathematical models in biomedical optics have been introduced, the remainder of this dissertation will focus on the development of novel versions of two of these types of models (semi-empirical and Monte Carlo) for specific tissue diagnostic applications in human pancreatic, bone, and breast tissues.

Specific Aim 1: To develop novel, closed-form, semi-empirical models of pancreatic tissue reflectance and fluorescence to quantitatively analyze measured optical data from normal and diseased human pancreatic tissues. The first-ever photon-tissue interaction (PTI) models of reflectance and fluorescence from human pancreatic tissue will be developed and fit to measured reflectance and fluorescence spectra from normal pancreatic tissue, pancreatitis, and adenocarcinoma to extract optical absorption and scattering parameters from the measured data.

Specific Aim 2: To assess the diagnostic significance of parameters extracted from the semi-empirical models of pancreatic tissue reflectance and fluorescence and employ these parameters for tissue classification. The diagnostic utility of the tissue parameters extracted from the PTI model described in Specific Aim 1 will be assessed in two ways: (1) Comparison of the changes in these parameters between the different tissue types with the changes observed in these tissue types via histopathology; (2) Statistical tests to determine the degree of statistical significance of each parameter for distinguishing between the different tissue types. Subsequently, the parameters from the PTI model will be included in a statistically-rigorous tissue classification algorithm that

employs multinomial logistic analysis with Generalized Estimating Equations to account for correlations in the data. From the tissue classification algorithm, the sensitivity, specificity, positive predictive value, and negative predictive value of the optical parameters for distinguishing pancreatic adenocarcinoma will be calculated.

Specific Aim 3: To develop a novel Monte Carlo model of inelastic (Raman) scattering in layered tissues, for application to bone and breast tissue disease diagnostics. A novel Monte Carlo model of Raman scattering in bone tissue will be developed to quantitatively assess the effect of absorption and scattering from overlying tissue layers (skin, muscle, tendon) and fiber-probe properties on the Raman signal from bone that is detected non-invasively by a fiber-optic probe placed on the surface of the skin. A novel Monte Carlo model of Raman scattering in breast tissue will be developed, validated, and employed to predict the effect of tissue and probe properties on the detected Raman signal from a buried tumor layer, for characterization of a spatially-offset Raman spectroscopy method for breast tumor margin assessment during surgery.

Specific Aim 4: To develop a novel, user-friendly, versatile Monte Carlo model of light propagation in complex biological tissues with irregular geometries. A novel MATLAB-based Monte Carlo fluorescence model will be developed with the use of surface meshes to describe photon transport in tissues with a wide range of biologically-relevant geometries. The temporally- and spatially-resolved fluorescence predictions of the code will be verified by comparison with a pre-existing, previously-validated code for bi-layered slab-mesh models.

1.4 Dissertation overview

Chapter 2 describes the development of the first-ever semi-empirical models of reflectance and fluorescence from human pancreatic tissues, and the application of these models to pancreatic cancer diagnostics.

Chapter 3 describes the development of novel Monte Carlo models of Raman scattering in layered biological tissues (bone tissue and breast tissue), and the use of these models for predicting the effect of tissue and probe properties on the detected Raman signal for bone tissue assessment and breast tumor margin detection during surgery.

Chapter 4 describes the development of a novel, user-friendly, mesh-based Monte Carlo model for simulation of light propagation in tissues with complex geometries.

Chapter 5 provides the conclusions of the dissertation, an overview of the key contributions described in the dissertation, and a summary of the next steps associated with the research mentioned in the dissertation.

Chapter 2

Pancreatic disease detection with reflectance and fluorescence

2.1. Development of Photon-Tissue Interaction (PTI) model

Pancreatic cancer has a five-year survival rate of only 6% [95], largely because there is currently no reliable method to diagnose the disease in its early stages. If a cancerous pancreatic tumor is accurately located and resected, and the patient then undergoes adjuvant therapy, the five-year survival rate only increases to about 20% [96]. Endoscopic ultrasound-guided fine-needle aspiration (EUS-FNA) is currently considered the diagnostic standard for pancreatic cancer diagnosis, but it has a sensitivity of only 54% when the patient also has chronic pancreatitis (pancreatic inflammation), which is frequently the case [97]. For diagnosing cancer in solid lesions of the pancreas, the negative predictive value (true negatives/all negatives) of EUS-FNA has a mean value of 72% and ranges from 16% to 92%, according to a recent meta-analysis of 28 clinical studies [96]. In [96], the authors reported that one of the most common "diagnostic dilemmas" is that of distinguishing malignant masses from inflammatory ones and concluded that EUS-FNA "preoperative biopsy of potentially resectable pancreatic tumours is not generally advisable, as malignancy cannot be ruled out with adequate reliability." Patients who are diagnosed with pancreatic cancer may undergo an arduous surgical procedure known as a Whipple resection; one study found that fully 9% of

Whipple patients were classified as "false positives" – that cancer was not present after the resected tissue was examined [98]. As a result, there is an unmet clinical need for a method that can accurately and reliably detect pancreatic cancer at early stages of development and distinguish it from chronic pancreatitis.

Reflectance and fluorescence spectroscopies have shown potential for clinical cancer detection in tissues including the breast [9], colon [5], cervix [7], and esophagus [6]. However, few studies have used optical methods to detect disease in the human pancreas. Optical interrogation of human pancreatic tissue has been demonstrated with optical coherence tomography [99, 100] and near infrared spectroscopy [101]. Partial-wave microscopic spectroscopy has shown promise for detecting cancer-related changes in the nanoarchitecture of human pancreatic cells obtained from archival cytology specimens [102]. Recently, an optical study of murine tumors consisting of human pancreatic cancer cells was conducted to quantitatively distinguish different tumor regions [103]. However, to our knowledge, there has been no comparable work involving mathematical models of experimentally obtained reflectance and fluorescence data from normal and diseased human pancreatic tissues. Toward this end, prototype instrumentation [28, 104] was developed at the University of Michigan to obtain reflectance and fluorescence spectra [28, 104, 105] from freshly excised human pancreatic tissues. In the study reported here [32], mathematical modeling of experimentally measured data was used to quantitatively describe differences in the reflectance and fluorescence spectra of normal pancreatic tissue, pancreatic adenocarcinoma, and pancreatitis. In particular, we sought to correlate the results of bimodal tissue optical spectroscopy with those of microscopic histological

examination of tissue (Figure 2.1), which is the current "gold standard" for cancer diagnostics.

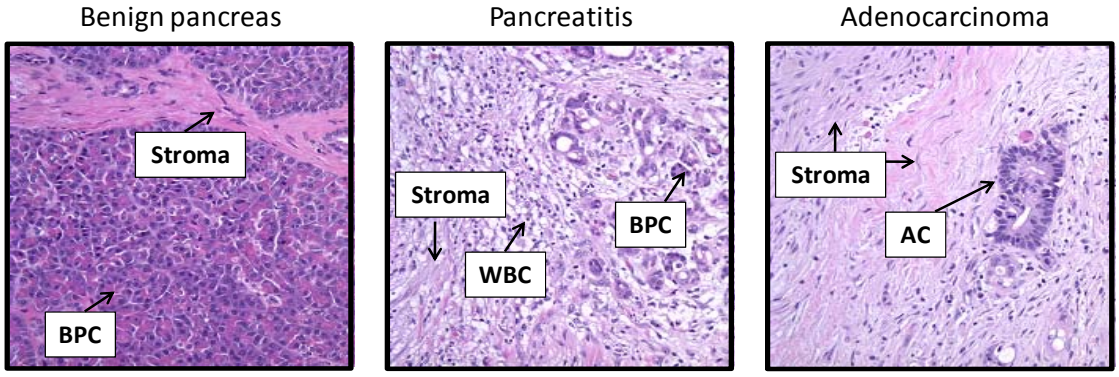

Figure 2.1 Representative histology images [32, 104] (used with permission) of normal pancreatic tissue (BPC = benign pancreatic cells), pancreatitis (WBC = white blood cells), and pancreatic adenocarcinoma (AC = adenocarcinoma cells with enlarged nuclei). The nuclei and stroma have been stained purple (hematoxylin stain) and pink (eosin stain), respectively.

As shown in Figure 2.1, pancreatic adenocarcinoma has larger nuclei than benign pancreatic tissue, and both adenocarcinoma and chronic pancreatitis have more collagenous stroma than normal pancreatic tissue. The mathematical model of reflectance quantitatively linked increased nuclear size in adenocarcinoma to changes in the measured reflectance spectra from 455-525 nm. The fluorescence model quantitatively linked increased collagen content in pancreatitis and adenocarcinoma to changes in the composition of the measured fluorescence spectra. Fitting the reflectance model to the experimental data also enabled what is, to the best of our knowledge, the first-ever extraction of values for the optical absorption and reduced scattering coefficients of human pancreatic tissues.

The mathematical model provided a quantitative link between optical spectroscopy and tissue histology (Table 2.1), suggesting a potential clinical application of optical spectroscopy and modeling to minimally invasive early cancer diagnostics in the pancreas. Although this paper focuses exclusively on pancreatic tissues, the methods described are potentially useful for optical diagnostic applications in other biological tissues.

Table 2.1 Key histological features of pancreatic tissues detected by optical spectroscopy [32].

Pancreatic tissue	Key histological features (relative to normal pancreatic tissue)	Optical signature found in
Adenocarcinoma	Increased nuclear size Greater stromal collagen content	Reflectance spectra Fluorescence spectra
Pancreatitis	Greater stromal collagen content	Fluorescence spectra

A prototype clinically-compatible Reflectance and Fluorescence Lifetime Spectrometer (RFLS; Figure 2.2), developed at the University of Michigan and described previously in the literature [28, 104, 106], was employed to obtain reflectance and fluorescence measurements of human pancreatic tissue within 15 minutes of removal via Whipple resection at the University of Michigan Medical Center. Briefly, the RFLS consisted of two light sources: a tungsten halogen lamp (HL 2000FHSA, Ocean Optics, Dunedin, FL) for CW reflectance, and a 355 nm pulsed laser with a 1 KHz repetition rate and a 500 ps pulse width (PNV001525-140, JDS Uniphase, San Jose, CA) for fluorescence excitation. Light from these two sources was directed onto the tissue via two separate optical fibers with core diameter of 600 μm. A third identical fiber was used to detect both the

reflectance and fluorescence photons that returned to the surface. These three fibers were incorporated into a custom-made fiber optic probe (Ocean Optics), in which they were arranged in a triangular geometry at the probe's distal end [27].

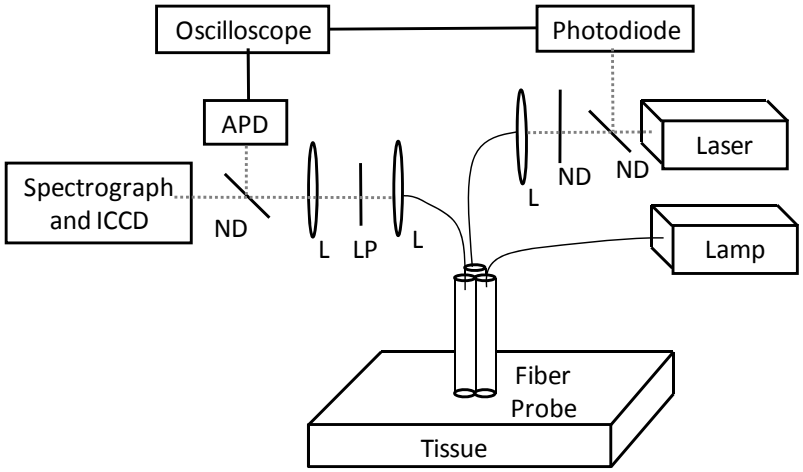

Figure 2.2 Schematic of prototype clinically-compatible Reflectance and Fluorescence Lifetime Spectrometer (RFLS) [10]. ND = neutral density filter, L = lens, LP = long pass filter, APD = avalanche photodiode, ICCD = intensified charge coupled device.

A portion of the collected signal was directed to time resolved fluorescence measurements (not described here). For wavelength resolved measurements of reflectance and fluorescence, the rest of the detected photons were sent to a spectrograph (MS 125, Oriel Instruments, Stratford, CT) coupled intensified charge coupled device (ICCD) camera (ICCD 2063, Andor Technology, Belfast, Northern Ireland). At each tissue site, fluorescence and reflectance measurements were made in sequence by using shutters to block the other light source. Each fluorescence (reflectance) measurement had an associated acquisition time of 2 seconds (2.5 seconds).

All measured reflectance and fluorescence spectra were background-corrected [125]. Corrected reflectance spectra R/R_o were obtained by background subtraction and then dividing by the reflectance spectrum R_o of the lamp [105]. The lamp spectrum R_o was measured by placing a reflectance standard (SRS-50-010, Labsphere, North Sutton, NH) or a neutral density filter (optical density 0.05) at the distal end of the probe and collecting the lamp light that was reflected from the surface of the reflectance standard. Each wavelength-resolved spectrum was normalized to peak intensity.

Measurements were taken at five sites on each tissue specimen. One pancreatectomy specimen was evaluated from each of two different patients. Each measured site was biopsied under the supervision of a clinical pathologist, and the biopsied samples were evaluated histologically. For the first patient, two of the sites were histologically normal and three were pancreatitis, while for the second patient, all five sites sampled were adenocarcinoma [28, 104, 105]. There were noticeable differences in both the reflectance and fluorescence spectra of the three tissue types, most notably around 500 nm for the reflectance spectra and near 400 nm for the fluorescence spectra [28, 104, 105]. The study was approved by the Institutional Review Board of the University of Michigan Medical Center and written consent was obtained from the patients.

The lineshapes of reflectance spectra from biological tissues are known to be primarily dependent on the absorption and scattering coefficients of the media. Absorbers such as blood will attenuate the light, while scatterers such as cell nuclei and collagen fibers will change the paths of the photons, eventually leading some of them back to the tissue

surface. Mie theory [33, 49, 51, 107] was used to describe the scattering coefficient μ_s, as a function of wavelength, in terms of the size and density of the scatterers in the tissue. Two Mie theory terms were used: one for spherical scatterers (cell nuclei) [49, 51, 107] and another for cylindrical scatterers (collagen fibers) [33, 49]. For the spherical Mie scattering term, the Van de Hulst approximation was used [51, 107]:

$$\mu_s(\lambda) = \frac{1}{2}\pi N_s L_o^2 \left[1 - \frac{\sin\left(2\delta/\lambda\right)}{\left(\delta/\lambda\right)} + \left(\frac{\sin\left(\delta/\lambda\right)}{\left(\delta/\lambda\right)} \right)^2 \right]; \delta = \pi L_o (n_s - n_m). \quad (3)$$

In Eq. (3), L_o is the scatterer diameter, N_s is the number of scatterers per unit volume, and n_s (n_m) is the index of refraction of the scatterer (surrounding medium). The wavelength λ is defined as λ_{vac}/n_m, where λ_{vac} is the wavelength of the incident light in vacuum. For all pancreatic tissue types in this study, n_m was assumed to be 1.33 (for water), while n_s was set as a free parameter and varied over a range previously measured for cell nuclei in freshly excised colon tissues [108]. For normal pancreatic tissue, the values of L_o and N_s were estimated from histology to be 9 μm and 7×10^7 cm^{-3}, respectively. The parameter N_s was kept constant for all tissue types. For both pancreatitis and adenocarcinoma, a enlargement factor L_d/L_o was applied to the nuclear diameter. It was expected that L_d/L_o would be equal to 1.0 for pancreatitis but greater than 1.0 for adenocarcinoma because cancer cells are known to exhibit enlarged nuclei [109-111].

The cylindrical scattering term was modeled by a combination of Bessel functions, in which the diameter, refractive index, and anisotropy of the collagen fibers were set to 3 μm, 1.35, and 0.975, respectively [33]. Both pancreatitis and adenocarcinoma were

modeled to have three times the concentration of collagen fibers as normal pancreatic tissue, as previously determined quantitatively for human pancreatic tissues using the Blumenkrantz and Asboe-Hansen method to assess hydroxyproline content [112]. Since the spherical and cylindrical Mie scattering terms are explicit functions of scatterer size and concentration, they were chosen over the commonly used approximation $\mu_s' = A\lambda^{-b}$ [9] (where μ_s' is the reduced scattering coefficient, equal to $\mu_s(1-g)$ in a tissue with anisotropy g).

The absorption coefficient μ_a was modeled as a linear combination of the extinction coefficients of oxy- and deoxy-hemoglobin [113], weighted according to their concentrations in the tissue [5]:

$$\mu_a(\lambda) = [Hb]\varepsilon_{Hb} + [HbO_2]\varepsilon_{HbO_2}. \quad (4)$$

Using Eq. (4), μ_a was represented as a function of the total tissue hemoglobin concentration $[Hb]_{tot} = [Hb] + [HbO_2]$ and the blood oxygen saturation $SO_2 = [HbO_2]/[Hb]_{tot}$.

The key diagnostic feature of the measured reflectance was increased amplitude between 455 nm and 525 nm in the adenocarcinoma spectra, relative to normal pancreatic tissue spectra. An empirical model (Eq. (2), re-written here as Eq. (5) for clarity), previously shown to be accurate in the case of small source-detector separations [52, 93], was used to model this feature by describing the reflectance spectra $R^{EMP}{}_i(\lambda)$ as functions of tissue absorption and scattering:

$$R_i^{EMP}(\lambda) = a\mu_s^{'}(\lambda)\exp\left(-\frac{C_{corr}(\lambda)\mu_a(\lambda)b}{\left[C_{corr}(\lambda)\mu_a(\lambda)\mu_s^{'}(\lambda)\right]^c}\right). \quad (5)$$

Since Eq. (3) gives the scattering coefficient $\mu_s(\lambda)$ and Eq. (5) is a function of the reduced scattering coefficient $\mu_s'(\lambda)$, it was necessary to estimate a value for the tissue anisotropy, so g was set to 0.9 at all λ for each tissue type [93]. The factor $C_{corr}(\lambda)$ describes the confinement of oxy- and deoxy-hemoglobin to cylindrical blood vessels [114]. The value of C_{corr} was modeled to be dependent on the mean radius of the blood vessels (set to 7 μm for all tissue types [115]) and the absorption coefficient of blood (given by Eq. (4) for each tissue type) [114].

The parameters a, b, and c are related to probe design; their respective values were estimated [52, 93] to be 0.11, 0.22, and 0.2. These values do not vary significantly when the tissue-probe refractive index mismatch is changed [93]. The value of b is somewhat dependent on probe source-detector separation [93], but changing b by as much as 50% was found to have very little effect on modeled pancreatic tissue spectra. Therefore, it was considered reasonable to approximate a, b, and c as noted. For the remainder of the text, the subscript i in Eq. (5) will be denoted as N for normal pancreatic tissue, P for pancreatitis, or A for pancreatic adenocarcinoma.

To model the reflectance spectra of diseased pancreatic tissue, Eq. (5) was used to generate a wavelength-resolved scaling factor to transform the experimentally measured reflectance spectrum $R^{MEAS}_N(\lambda)$ of normal pancreatic tissue into an accurate model for the

adenocarcinoma reflectance spectrum $R^{MODEL}{}_{A}(\lambda)$ and the pancreatitis reflectance spectrum $R^{MODEL}{}_{P}(\lambda)$, according to the equations:

$$R_A^{MODEL}(\lambda) = R_N^{MEAS}(\lambda)\left(R_A^{EMP}(\lambda)/R_N^{EMP}(\lambda)\right); \tag{6}$$

$$R_P^{MODEL}(\lambda) = R_N^{MEAS}(\lambda)\left(R_P^{EMP}(\lambda)/R_N^{EMP}(\lambda)\right). \tag{7}$$

Optimal fits of Eqs. (6) and (7) to the respective measured adenocarcinoma and pancreatitis reflectance spectra were determined via minimization of a cost function C_R, which was equal to the average magnitude of the difference between the reflectance model and measured reflectance spectrum over the 400-700 nm wavelength range. For each tissue type, every individual measured spectrum was first normalized to peak intensity, then these spectra were averaged and the result was normalized to peak intensity again. All of the modeled reflectance spectra were also normalized to peak intensity.

In the fitting procedure described above, the nuclear enlargement factor L_d/L_o for diseased pancreatic tissue (adenocarcinoma and pancreatitis) was varied from 1.0 to 1.9 in steps of 0.1, and the nuclear refractive index n_{sd} of diseased pancreatic tissue was varied from 1.370 to 1.400, in steps of 0.005. The total hemoglobin concentration $[Hb]_{tot}$ was varied from 15 μM to 25 μM for normal pancreatic tissue and 2.5 μM to 25 μM for diseased tissue (in steps of 2.5 μM for all tissue types). The blood oxygen saturation SO_2 was varied from 0.1 to 0.9 (in steps of 0.2) for all tissue types.

The fitting procedure described above was performed for each of three different values of the nuclear refractive index n_{sn} of normal pancreatic tissue: 1.370, 1.375, and 1.380. This range and these values were identified in part because of the results of studies conducted on freshly excised diseased and normal human tissues [108], and in part because we observed that the algorithm extracted physically reasonable values of both L_d/L_o and n_{sd} that did not vary much as n_{sn} was changed. The set of free parameter values that minimized C_R was extracted from each fit, as reported below. The fitting method described here was compared with a nonlinear least-squares method, and t-tests demonstrated that there were no statistically significant differences ($p > 0.25$) between the tissue parameters extracted from the two fitting methods.

Optimal fits of the mathematical model to experimentally measured reflectance data for adenocarcinoma and pancreatitis are shown in Figure 2.3. The error bars on the modeled reflectance spectra represent the standard deviation associated with varying n_{sn} over the range described previously. In the diagnostically important wavelength range between 455 and 525 nm, where the adenocarcinoma reflectance spectra differed significantly from both the normal and pancreatitis spectra, the mean error in fit of the adenocarcinoma model to the average measured spectrum was less than 6%.

The optimal fits between the predicted and measured adenocarcinoma reflectance spectra extracted a (mean ± standard deviation) value of $L_d/L_o = 1.33 \pm 0.06$ for the nuclear enlargement factor and a value of $n_{sd} = 1.375$ for the nuclear refractive index. The optimal fits between the predicted and measured pancreatitis reflectance spectra extracted

a (mean ± standard deviation) value of L_d/L_o = 1.03 ± 0.06 for the nuclear enlargement factor and n_{sd} = 1.372 ± 0.003 for the nuclear refractive index. The model revealed that differences in the reflectance spectra of normal pancreatic tissue, pancreatitis, and adenocarcinoma could be quantitatively linked to an increase in nuclear size for adenocarcinoma relative to pancreatitis and normal tissue, a result that is supported by histology [109-111].

The reflectance fits extracted (mean ± standard deviation) $[Hb]_{tot}$ values of 18.8 ± 4.1 μM for normal pancreatic tissue, 7.5 ± 2.5 μM for pancreatitis, and 20.0 ± 5.0 μM for adenocarcinoma. The fits extracted (mean ± standard deviation) SO_2 values of 0.13 ± 0.08 for normal pancreatic tissue, 0.57 ± 0.23 for pancreatitis, and 0.9 for adenocarcinoma. T-tests demonstrated that there were no statistically significant differences ($p > 0.25$) between either the $[Hb]_{tot}$ or SO_2 values of normal pancreatic tissue that were extracted from the fits to the measured adenocarcinoma spectra and those extracted from the pancreatitis spectra.

Since spectra were obtained *ex vivo*, it is possible that these values reflect the amount of blood that drained from the tissue and the time the tissue was exposed to air prior to measurements. However, these results signify a promising step toward the eventual extraction of hemoglobin concentration and blood oxygen saturation values from *in vivo* measurements of the human pancreas.

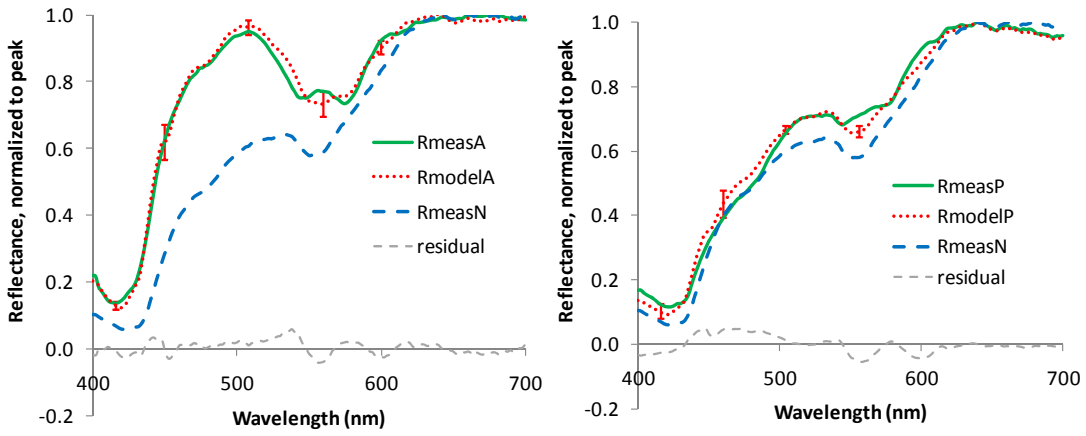

Figure 2.3 Optimal fit of mathematical model (dotted red lines) versus average measured result for reflectance spectra (solid green lines) of pancreatic adenocarcinoma (left) and pancreatitis (right), with residuals (gray) [32]. The experimentally obtained reflectance spectrum for normal pancreatic tissue (dashed blue lines) is shown on both plots for comparison. Relative to normal pancreatic tissue, adenocarcinoma was modeled to exhibit a 1.33x increase in the diameter of cell nuclei, and a 3x increase in collagen concentration; the pancreatitis was modeled to also have a 3x increase in collagen concentration, but no significant change in the size of cell nuclei.

The spectra from Figure 2.3 were also compared with a previously published reflectance spectrum taken *in vivo* from a pancreatic adenocarcinoma xenograft created by injecting human pancreatic cancer cells into the pancreas of a Non-Obese Diabetic/Severe Combined Immunodeficiency (NOD/SCID) mouse [28]. Due to the suppressed immune response in SCID mice, the xenograft had a very low amount of collagen relative to cells. In spite of this difference, the reflectance spectrum of the xenograft was similar to that of freshly excised human adenocarcinoma from 400-525 nm, a result attributed to the increased size of the cell nuclei in both the xenograft and the *ex vivo* human adenocarcinoma tissue samples.

Model fits to experimental data were employed to estimate wavelength-resolved absorption and reduced scattering coefficients for each tissue type via Eqs. (3) and (4) and the formula for Mie scattering from cylinders [49]. The results shown in Figure 2.4 represent the first extraction (to our knowledge) of absorption and reduced scattering coefficients of human pancreatic tissues. The error bars represent the standard error over a set of fits for different values of the nuclear refractive index n_{sn} of normal pancreatic tissue. The values of the coefficients in Figure 2.4 are in the range expected for gastrointestinal tissue [37]. However, it is important to note that these values are specific to the pancreatic tissue samples measured in this particular study.

This study was primarily concerned with the lineshapes of the absorption and reduced scattering spectra, because differences in these lineshapes were indicative of differences in the measured reflectance spectra. For instance, the reduced scattering coefficient of adenocarcinoma was highest from 400-525 nm, whereas the reduced scattering coefficients of normal pancreatic tissue and pancreatitis were lowest. In this range there is also a prominent increase in the amplitude of the adenocarcinoma reflectance spectrum relative to that of normal pancreatic tissue and pancreatitis.

The differences in the mean extracted absorption coefficients for normal pancreatic tissue, pancreatitis, and adenocarcinoma could be attributed to the *ex vivo* nature of the measurements, in which tissue hemoglobin concentration and blood oxygen saturation were likely affected by the amount of blood that drained from the tissue and the time the tissue was exposed to air prior to measurements.

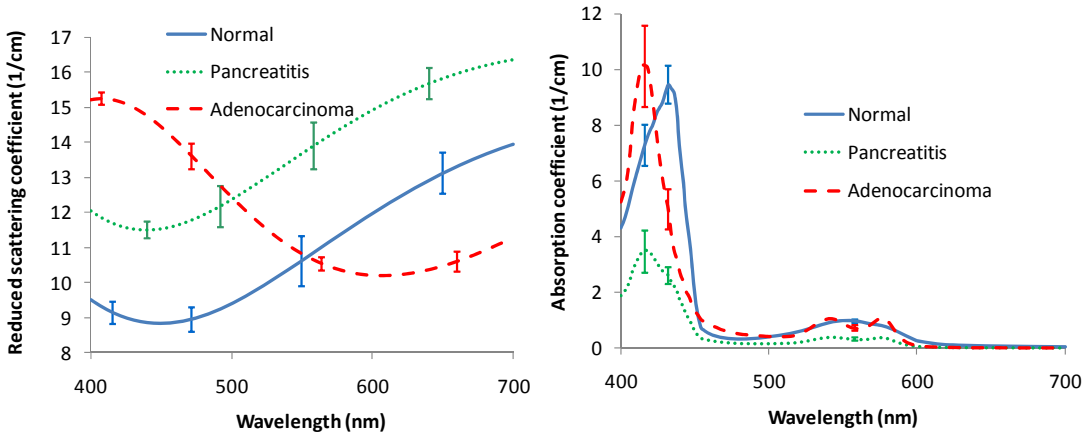

Figure 2.4 Wavelength-resolved reduced scattering (left) and absorption (right) coefficients [32] of normal pancreatic tissue (solid blue lines), pancreatitis (dotted green lines), and pancreatic adenocarcinoma (dashed red lines), extracted from the reflectance model employed in this study. The error bars represent standard error.

Once the fits of the reflectance model to the adenocarcinoma and pancreatitis data were obtained, the extracted scattering parameters were used in an algorithm to remove artifacts of scattering and absorption from the measured fluorescence spectra of normal pancreatic tissue, pancreatitis and adenocarcinoma. To perform this task, a separate Beer-Lambert attenuation factor was constructed for each tissue type by using $\mu_a(\lambda)$ and $\mu_s'(\lambda)$ values specific to that tissue type. The intrinsic fluorescence spectrum $F_{INTRINSIC}(\lambda)$ was then extracted according to the equation:

$$F_{INTRINSIC}(\lambda) = F_{MEAS}(\lambda)\exp\left(\left[\mu_a(\lambda) + \mu_s'(\lambda)\right]z\right). \quad (8)$$

The variable z represented the length of the average path of travel to the surface for photons that had been absorbed and re-emitted by a fluorophore within the tissue. The average value of z over the wavelength range of 400-638 nm was estimated to be 0.064 cm for all tissue types. This value was calculated from time-resolved Monte Carlo

simulations of photon propagation in pancreatic tissue models [77]. Separate simulations were run for normal pancreatic tissue, pancreatitis, and adenocarcinoma. For each of these simulations, the absorption and reduced scattering coefficients were obtained by averaging the absorption and reduced scattering spectra (Figure 2.4) of the tissue type being modeled. The anisotropy g was approximated to be 0.9 for all tissue types. The average path length of emission photon travel was determined by finding the time at which the greatest number of simulated photons exited the tissue, multiplying that by the speed of light in the medium, and dividing by two to account for only the fluorescence photons' travel back to the surface (under the approximation that on average, a photon would be absorbed by a fluorophore at its point of greatest depth in the tissue). Calculation of the same z value for all tissue types likely resulted from the coarseness of the time resolution (1 ps) used in the simulations, as well as the use of average absorption and reduced scattering coefficients as inputs.

We note that Eq. (8) does not include the absorption coefficient at the excitation wavelength. This omission affects only the amplitudes and not the lineshapes of the intrinsic fluorescence spectra; thus it will not cause errors in the relative contributions of fluorophores extracted from these spectra.

Once the intrinsic fluorescence spectra were obtained for each tissue type (solid green lines in Figure 2.5), their lineshapes could be decomposed into the component spectra of collagen, NADH, and FAD, three principal contributors to tissue autofluorescence in the 400-700 nm wavelength range. For each tissue type, the intrinsic fluorescence spectrum

was fit to a linear combination (*BasisFit(λ)*) of experimentally measured basis spectra of collagen, NADH, and FAD:

$$BasisFit(\lambda) = C_{COLLAGEN} F_{COLLAGEN}(\lambda) + C_{NADH} F_{NADH}(\lambda) + C_{FAD} F_{FAD}(\lambda). \quad (9)$$

The basis spectra $F_{COLLAGEN}(\lambda)$ and $F_{FAD}(\lambda)$ were measured at 355 nm excitation on a spectrofluorometer (SPEX® FL3-22 Fluorolog-3, Jobin-Yvon Horiba, Japan) while the $F_{NADH}(\lambda)$ was measured on the RFLS. Solutions of 0.005 mg/ml of NADH (N-8129, Sigma Aldrich, St. Louis, Missouri) in water, 0.7 mg/ml of FAD (F6625, Sigma Aldrich) in water, and 1 mg/ml of collagen (C5483, Sigma Aldrich) in acetic acid were used for the measurements.

To fit the intrinsic fluorescence spectra to Eq. (9), the values of $C_{COLLAGEN}$, C_{NADH}, and C_{FAD} were treated as free parameters whose values were varied between 0 and 0.9 (in steps of 0.1) until a minimal value of a cost function C_F was obtained. The cost function C_F was defined to be the average magnitude of the difference between $BasisFit(\lambda)$ and $F_{INTRINSIC}(\lambda)$ over the wavelength range of 400 nm to 638 nm. For each tissue type, every individual fluorescence spectrum was normalized to the area under the curve from 400-638 nm; these spectra were then averaged and this average spectrum was corrected for attenuation to produce $F_{INTRINSIC}(\lambda)$. For all tissue types, $BasisFit(\lambda)$ and $F_{INTRINSIC}(\lambda)$ were both normalized to the peak intensity. Each of the basis spectra ($F_{COLLAGEN}(\lambda)$, $F_{NADH}(\lambda)$, and $F_{FAD}(\lambda)$) was blue shifted by about 12 nm, which accounted for the fact that the component spectra were measured in various chemical solvents and not within a biological tissue environment [9].

In the algorithm to minimize C_F, the values of L_d/L_o and n_{sd} were taken to be those extracted from the reflectance fits and the value of n_{sn} was fixed at 1.375 (the midpoint of the range over which this parameter was varied in the reflectance fits). To minimize the presence of artifacts from under-correction or over-correction of the measured fluorescence spectra, the values of $[Hb]_{tot}$ and SO_2 were once again treated as free parameters. This procedure was considered reasonable because L_d/L_o and n_s were not expected to change much from site to site over the time period that *ex vivo* measurements were taken, but $[Hb]_{tot}$ and SO_2 were expected to be much more variable. For all tissue types, $[Hb]_{tot}$ was varied from 15 to 25 μM (in steps of 2.5 μM) and SO_2 was varied from 0.1 to 0.9 (in steps of 0.2). These ranges were considered reasonable given the means and standard deviations of the $[Hb]_{tot}$ and SO_2 values reported previously, in addition to the fact that measurements were performed *ex vivo*.

Optimal fits of $BasisFit(\lambda)$ to $F_{INTRINSIC}(\lambda)$ for normal pancreatic tissue, pancreatitis, and pancreatic adenocarcinoma are shown in Figure 2.5. The values of C_{COLL}, C_{NADH}, and C_{FAD} extracted from these fits are displayed in Table 2.2. The deviation of the basis fits to the intrinsic fluorescence spectra of normal pancreatic tissue and pancreatitis around 600 nm may be attributed to the fact that the model does not include porphyrin fluorescence, which is known to peak around 635 nm when excited with 380-440 nm light [116].

The data in Figure 2.5 were also compared to the intrinsic fluorescence extracted from a fluorescence spectrum obtained *in vivo* from a pancreatic adenocarcinoma xenograft in a

NOD/SCID mouse [28]. Mathematical modeling showed that the xenograft fluorescence could be mostly attributed to intracellular components, a conclusion that made sense given that the xenograft tumor was predominantly comprised of cells.

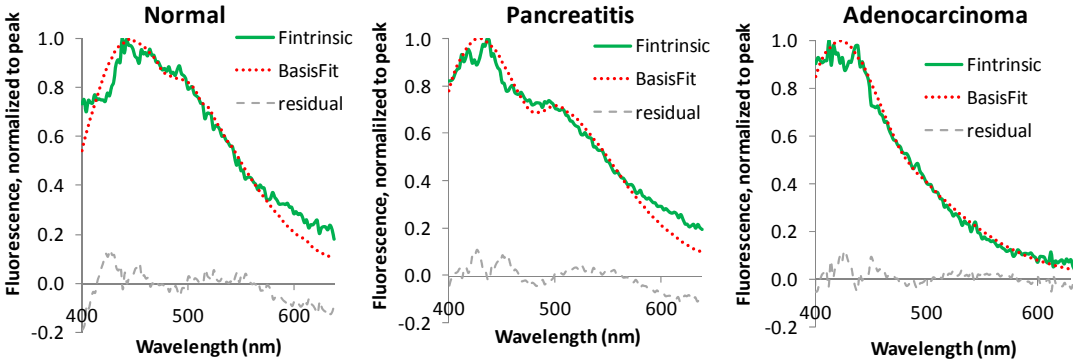

Figure 2.5 Intrinsic fluorescence spectra (solid green lines) of normal pancreatic tissue (left), pancreatitis (middle), and pancreatic adenocarcinoma (right), each shown with an optimal fit to a linear combination (dotted red lines, residuals in gray) of measured and blue-shifted collagen, NADH, and FAD basis spectra [32].

In Figure 2.5, the intrinsic fluorescence between 500 and 600 nm (where intracellular NADH and FAD emit prominently) was observed to decrease in pancreatitis and adenocarcinoma, relative to normal pancreatic tissue. Since the spectra in Figure 2.5 were normalized to their peak values, these differences are consistent with the known higher concentrations of collagen in both pancreatitis and adenocarcinoma, relative to normal pancreatic tissue [112]. This trend was also revealed by the increase in the percentage contribution of collagen (determined via the collagen fit coefficient C_{COLL}) to the intrinsic fluorescence of pancreatitis and adenocarcinoma, relative to normal pancreatic tissue, as illustrated in Table 2.2.

Table 2.2 Fit coefficients C_i (percentage contributions) for collagen, NADH, and FAD basis spectra to intrinsic fluorescence spectra of normal pancreatic tissue, pancreatitis, and pancreatic adenocarcinoma [32].

	Normal	Pancreatitis	Adenocarcinoma
$C_{COLLAGEN}$	0.6 (35%)	0.9 (56%)	0.9 (82%)
C_{NADH}	0.8 (47%)	0.3 (19%)	0.1 (9%)
C_{FAD}	0.3 (18%)	0.4 (25%)	0.1 (9%)

The trend shown in Table 2.2 was further confirmed by qualitative examination of Figure 2.1, which shows representative histology slides of tissue samples from the patients involved in the study. In these slides, the amount of collagen incursion observed amidst the cells in the tissue samples clearly increases in pancreatitis and adenocarcinoma, relative to normal pancreatic tissue. In the diagnostically relevant region between 500 and 550 nm, the mean error in fit between Eq. (9) and the intrinsic fluorescence was less than 4% for normal pancreatic tissue and pancreatitis, and less than 8% for adenocarcinoma.

In this study, mathematical models of reflectance and intrinsic fluorescence were developed and employed to quantitatively describe the effects of key histologically observed tissue parameters on the measured optical spectra of pancreatitis and pancreatic adenocarcinoma (relative to normal pancreatic tissue). An empirical mathematical model of reflectance was able to fit the prominent feature in the average adenocarcinoma spectrum (increased amplitude from 455-525 nm, relative to normal pancreatic tissue) with less than 6% error. Fitting the reflectance model to the measured optical spectra enabled the first-ever (to our knowledge) extraction of wavelength-resolved absorption

and reduced scattering coefficients of human pancreatic tissues. Obtaining values for the optical coefficients is an important result, because knowledge of these coefficients is essential for accurate computational studies of photon migration in pancreatic tissue models. One such computational method is Monte Carlo simulation [75, 77], which is accurate throughout optical parameter space for modeling photon transport in biological tissue.

We note that in this study, Eq. (5) is not employed to model the reflectance spectrum of normal pancreatic tissue. The "normal" data shown in Figure 2.3 is averaged, experimentally measured data from normal pancreatic tissue. This "canonical normal" data is $R^{MEAS}{}_{N}(\lambda)$ in Eqs. (6) and (7). In principle, it could be useful to employ a normal spectrum from each individual patient, but this scenario would not always be possible in a clinical diagnostic application, so here we employ a "canonical normal" spectrum as our general approach.

In theory, it is also possible to obtain the absorption and scattering parameters by fitting the measured reflectance spectra directly with Eq. (5), but we did not use this approach here. Our approach focuses on modeling key differences between the reflectance spectra of normal and diseased pancreatic tissues. One potential advantage of this approach is that many of the characteristics of pancreatic tissue (such as size distributions for scatterers, fluctuations in refractive index, and packaging of hemoglobin into red blood cells [117]) are implicitly contained (at least approximately) in the measured "canonical normal" reflectance spectrum.

The scattering parameters extracted from the reflectance fits were used in an algorithm that corrected the measured fluorescence spectra for attenuation artifacts and fit the resulting "intrinsic" endogenous fluorescence spectra to a linear combination of basis spectra from native tissue fluorophores (collagen, NADH, FAD). This procedure determined the relative contributions from both extracellular (collagen, 400-450 nm emission peak) and intracellular (NADH and FAD, 500-600 nm emission peak) autofluorescence for each tissue type. The relative contribution of collagen was found to be greater in the intrinsic fluorescence spectra of pancreatitis and adenocarcinoma. Since the spectra were normalized to the peak, the intrinsic fluorescence of pancreatitis and adenocarcinoma spectra exhibited a decrease in amplitude in the 500-600 nm range, where NADH and FAD emission are prominent. These results were consistent with the increased collagen fibrosis [112, 118] seen in histology of pancreatitis and adenocarcinoma.

As seen in Figure 2.3, Figure 2.5, and Table 2.3, empirical models of reflectance and intrinsic fluorescence were able to quantitatively describe the major differences between normal pancreatic tissue, adenocarcinoma, and pancreatitis in terms of histologically observed changes in biologically meaningful parameters.

The reflectance spectra of cancerous tissue differed most noticeably from normal pancreatic tissue at around 500 nm (Figure 2.3), a change that could be quantitatively linked, via spherical Mie scattering, to larger cell nuclei in pancreatic adenocarcinoma.

Subtle differences throughout the reflectance spectra of both pancreatitis and adenocarcinoma were found, via modeling of cylindrical Mie scattering, to correlate with the increased number of collagen fibers in both pancreatitis and cancer. These results agree with histology in that both pancreatitis and pancreatic adenocarcinoma are marked by greater collagen content than normal pancreatic tissue, but only adenocarcinoma is characterized by larger cell nuclei [112, 118-120].

Table 2.3 Prominent disease-related changes in histology features and measured optical spectra of pancreatic tissues, along with corresponding changes made to mathematical models of reflectance and fluorescence [32].

Pancreatic tissue	Adenocarcinoma	Pancreatitis
Key histological features (relative to normal pancreatic tissue)	Increased nuclear size Greater stromal collagen content	Greater stromal collagen content
Optical signature (relative to normal pancreatic tissue)	Increased amplitude of reflectance spectrum from 455-525 nm Spectral lineshape change in intrinsic fluorescence spectrum from 500-550 nm	Spectral lineshape change in intrinsic fluorescence spectrum from 500-550 nm
Mathematically modeled by	Multiplying spherical scatterer diameter L_o by 1.33 for reflectance model Increasing percentage contribution of collagen basis spectrum from 35% to 82% in fit to intrinsic fluorescence	Increasing percentage contribution of collagen basis spectrum from 35% to 56% in fit to intrinsic fluorescence
Mean error in fit of model to experimentally measured data in diagnostically relevant region	Less than 6% from 455-525 nm for adenocarcinoma reflectance model Less than 8% from 500-550 nm for all intrinsic fluorescence models	Less than 4% from 500-550 nm for all intrinsic fluorescence models

The intrinsic fluorescence model (Figure 2.5, Table 2.2) showed that for both pancreatitis and adenocarcinoma, there was an increased contribution from the collagen in the stroma, relative to normal pancreatic tissues. This result is consistent with the histological observation that the change from normal pancreatic tissue to both pancreatitis and adenocarcinoma is characterized by increased collagen amidst the cells [112, 118]. However, the intrinsic fluorescence spectra of pancreatitis and cancer were also shown to be different from each other. Whereas the reflectance model was most useful for discriminating pancreatic adenocarcinoma from pancreatitis, the intrinsic fluorescence model was more effective at distinguishing between all three tissue types. The results of this study lend credence to the idea that combining reflectance and fluorescence spectroscopies has a diagnostic advantage over using just one of these modalities to detect pancreatic cancer.

The empirical reflectance model was compared with the diffusion approximation, which is often employed to extract tissue absorption and scattering properties from experimentally measured tissue reflectance spectra [5, 9, 68]. When the reflectance fitting procedure was employed with a subset of the $[Hb]_{tot}$ and SO_2 ranges described previously, the diffusion approximation model was noticeably less effective than the empirical model for fitting the adenocarcinoma reflectance spectrum. In the diagnostically-relevant wavelength range of 455-525 nm, the error in fit to the measured adenocarcinoma spectrum was less than 6% for the empirical model, but it rose to as high as 13% with the diffusion approximation model. These results were not surprising because the fiber-optic probe in this study had a source-detector separation of only about

660 μm. Using the reduced scattering coefficients μ_s' from Figure 2.4, it can be shown that the source-detector separation of the probe was often smaller than $1/\mu_s'$. This condition causes the diffusion approximation to break down [68], but the empirical model is accurate in this regime [93].

Although the reflectance and fluorescence models employed in this paper are useful for extracting physical information from experimental measurements of pancreatic tissue, the models do have several key limitations. The empirical reflectance model approximated tissue scattering as originating from only two sources: sub-cellular nuclei and extracellular collagen fibers. As a first approximation, this model is reasonable, because cell nuclei are known to be important contributors to forward scattering [121, 122] and collagen fibers have been shown to be a significant source of extracellular scattering [33]. In addition, the experimentally measured "canonical normal" tissue spectrum used in the reflectance model contains some level of information about the optical scattering and absorption from other intracellular and extracellular sources. Cell components such as mitochondria, cytoplasm, and plasma membrane also contribute to tissue scattering [121, 122] and are reflected here in the "canonical normal" tissue spectrum for normal, but not diseased, pancreatic tissues.

The model fixed the diameter and concentration of normal cell nuclei in pancreatic tissue at constant values even though there was uncertainty in the estimation of these parameters. The model also approximated the anisotropy to be constant for all tissue types, when that parameter would likely be different for normal pancreatic tissue,

pancreatitis, and adenocarcinoma because each of these tissue types is associated with a different distribution of scatterer sizes and shapes. Furthermore, the fluorescence model approximated the average emission photon path to have the same length for normal pancreatic tissue, pancreatitis, and adenocarcinoma. Future work to improve the model will include an investigation into the effect of including additional scattering terms for other cellular and extracellular components, as well as variations between the anisotropy values for the different tissue types. An expanded study will include an investigation into the effect of incorporating a term into the reflectance model to explicitly correct for the packaging of hemoglobin into erythrocytes [117], as well as further consideration of changes in the distribution of blood vessel sizes for the different tissue types. Preliminary studies showed that when the mean blood vessel radius for adenocarcinoma was doubled (to 14 μm) or halved (to 3.5 μm), relative to that of normal tissue (7 μm), there was no change in the tissue parameters extracted from the reflectance model. However, more sophisticated models of pancreatic tissue vasculature could be incorporated in the future. In addition, a more rigorous calculation of the average emission photon path length as a function of wavelength for each different tissue type will be explored.

Current methods to detect pancreatic adenocarcinoma are highly invasive and fail to find the disease early or to distinguish it from inflammation (pancreatitis). Hence, there is great biomedical need for an endoscopic screening procedure for early detection of pancreatic adenocarcinoma. Bimodal reflectance and fluorescence spectroscopy is a potential inroad into addressing this unmet clinical need. In this study, mathematical models of measured reflectance and fluorescence spectra were employed to quantitatively

describe differences between normal pancreatic tissue, pancreatic adenocarcinoma, and pancreatitis. By using biomedically relevant parameters, the model provided a link between the results of optical spectroscopy and histology. Features in the reflectance spectra were quantitatively linked to larger cell nuclei in cancer and increased collagen content in both cancer and pancreatitis. The intrinsic fluorescence spectra were fit to a linear combination of collagen, NADH, and FAD basis spectra to show quantitative differences in the contribution of collagen to the measured fluorescence from normal pancreatic tissue, pancreatic adenocarcinoma, and pancreatitis.

Translation to an *in vivo* setting is feasible because the model can extract the optical absorption coefficient from increased blood content in the tissues. We believe that the reflectance model should be effective even if the blood content is higher, especially because we were able to model the reflectance obtained *in vivo* from a xenograft in a mouse with an average error in fit of less than 12% in the diagnostically relevant wavelength range of 455 nm to 525 nm. Challenges associated with obtaining an accurate reflectance fit near 425 and 550 nm (where hemoglobin absorption is noticeable) can potentially be resolved by fitting each individual reflectance spectrum to an empirical equation [52, 93], a photon migration model [123, 124], or the P_3 approximation [125]. Another test of the model could involve comparing the intrinsic fluorescence extracted via a Beer-Lambert factor (Eq. (8)) with that obtained with a more detailed photon migration model [123, 124]. An *in vivo* human study has been approved and *in vivo* data collection has begun.

Overall, the mathematical models of reflectance and fluorescence developed in this paper are potentially useful tools for pancreatic cancer diagnostics because of their ability to quantitatively link the experimental results of optical spectroscopy with those of histopathology. Figures 2.1 and 2.3 show that the mathematical model of reflectance presented in this paper was able to quantitatively describe the reflectance spectra of normal pancreatic tissue, pancreatitis, and pancreatic adenocarcinoma in terms of biomedically relevant parameters. The algorithm to model the reflectance was rapid, taking less than 7 minutes to execute on a desktop computer. Furthermore, the concept of scaling an average measured normal pancreatic tissue reflectance spectrum to obtain the pancreatitis and adenocarcinoma spectra was found to be helpful with data interpretation due to its intuitive nature. Figure 2.4 shows the capability of the reflectance model to extract, for the first time (to our knowledge), absorption and reduced scattering coefficients of the aforementioned human pancreatic tissue types. When the measured fluorescence spectra were corrected for attenuation artifacts (Figure 2.5), the resulting intrinsic fluorescence spectra revealed differences in collagen content that correlated with histology (Table 2.2). The, rapid, intuitive, and biomedically relevant nature of these methods suggests that the approach outlined in this work may be of potential use not only for pancreatic cancer detection, but also for other optical diagnostic applications involving a wider range of biological tissues.

2.2. PTI model extracts statistically-significant tissue parameters

Here [10], the PTI model was employed to analyze 96 pairs of reflectance and fluorescence spectra from freshly excised human pancreatic tissues. For each pair of spectra, the PTI model extracted a cellular nuclear size parameter from the measured reflectance, and the relative contributions of extracellular and intracellular fluorophores to the intrinsic fluorescence. The results indicated a statistically significant increase in the nuclear size of adenocarcinoma (relative to both normal pancreatic tissue and chronic pancreatitis) and a statistically significant increase in the extracellular collagen contribution to fluorescence in both adenocarcinoma and chronic pancreatitis (relative to normal pancreatic tissue). This suggests that reflectance and fluorescence spectroscopies have the potential to quantitatively distinguish among pancreatic tissue types, including normal pancreatic tissue, chronic pancreatitis, and pancreatic adenocarcinoma, via biophysical tissue properties extracted from the spectra.

At the University of Michigan (U of M), a prototype clinically-compatible Reflectance and Fluorescence Lifetime Spectrometer (RFLS; Figure 2.2), described previously [28, 106], was developed and employed to measure reflectance and fluorescence from human pancreatic tissue samples. Reflectance and fluorescence spectra were measured from human pancreatic tissue samples obtained at the U of M Medical Center within 30 minutes of excision, during operative procedures (Whipple procedure or distal pancreatectomy) performed on 9 patients (average age 62 ± 11 years; 7 female, 2 male). The study received approval from the Institutional Review Board of the U of M Medical School. Prior to data acquisition, written consent was obtained from each patient.

Spectra were measured from 50 pancreatic tissue sites. Immediately following optical measurement, a tissue biopsy was taken from each of these sites and used for histopathologic analysis. Of the 50 sites, 11 were diagnosed by pathology as histologically normal, 22 were diagnosed as chronic pancreatitis (inflammation), and 17 were diagnosed as adenocarcinoma. All pancreatic adenocarcinoma spectra in this study were from patients who had concurrent histologic evidence of chronic pancreatitis in addition to pancreatic adenocarcinoma. Two wavelength-resolved reflectance spectra and two wavelength-resolved fluorescence spectra were taken from each tissue site, except for one adenocarcinoma site, from which only one set of these three measurements was taken.

Two pairs of chronic pancreatitis spectra were excluded because the fluorescence spectra had a signal-to-noise ratio (SNR) of less than 25, where SNR was defined to be the mean signal at peak fluorescence divided by the standard deviation of the noise in the measured spectrum. Another pair of chronic pancreatitis spectra was excluded because the intensity of the reflectance signal at 550 nm was less than 1/10 of that at 650 nm. The remaining 96 pairs of reflectance and fluorescence spectra (22 pairs of normal spectra, 41 pairs of chronic pancreatitis spectra, 33 pairs of adenocarcinoma spectra) were individually fit using the PTI model.

The PTI model was described in detail previously [32]. Briefly, an empirical model [52] of reflectance $R^{EMP}(\mu_s, \mu_a; \lambda)$ as a function of the tissue scattering coefficient μ_s (related

to the nuclear diameter L and nuclear refractive index n_s) and absorption coefficient μ_a (related to the total hemoglobin concentration $[Hb]_{tot}$ and blood oxygen saturation SO_2) was employed to construct a wavelength-resolved scaling factor to transform an average measured "canonical normal" pancreatic tissue reflectance spectrum $R^{MEASURED}{}_{NORMAL}(\mu_a, \mu_s; \lambda)$ into the PTI model spectrum $R^{PTI}{}_{UNKNOWN}(\mu_a, \mu_s; \lambda)$ for each of the 96 individual measured reflectance spectra:

$$R^{PTI}_{UNKNOWN}(\mu_a, \mu_s; \lambda) = \left(R^{MEASURED}_{NORMAL}(\mu_a, \mu_s; \lambda)\right)\left(\frac{R^{EMP}_{UNKNOWN}(\mu_a, \mu_s; \lambda)}{R^{EMP}_{NORMAL}(\mu_a, \mu_s; \lambda)}\right). \quad (10)$$

The PTI-modeled spectra are denoted "unknown" because the model was blinded to pancreatic tissue type. Each model spectrum $R^{PTI}{}_{UNKNOWN}(\mu_a, \mu_s; \lambda)$ resulting from Eq. (10) was individually fit to the corresponding measured reflectance spectrum $R^{MEASURED}(\mu_a, \mu_s; \lambda)$ by varying the nuclear diameter L, total hemoglobin concentration $[Hb]_{tot}$, and blood-oxygen saturation SO_2 over biologically reasonable ranges (Table 2.4) and minimizing the cost function $|R^{PTI}{}_{UNKNOWN} - R^{MEASURED}|$ over the wavelength range of 400 nm to 700 nm [32].

The fitting procedure in this study was identical to that developed in [32], except for four changes: (1) The measured "canonical normal" spectrum was taken to be an average of all 22 measured normal spectra. (Each normal reflectance spectrum was first normalized to its peak value in the 400-700 nm wavelength range, then all 22 of these spectra were averaged, and, finally, the resulting spectrum was normalized to the peak again to create the "canonical normal" spectrum.). (2) The concentration of collagen fibers (cylindrical scatterers) for all unknown reflectance spectra was set to three times that of the canonical

normal (motivated by previous work demonstrating that the mean collagen content of both pancreatic cancer and tumor-associated chronic pancreatitis was roughly three times as high as that of normal pancreatic tissue [112]). This approximation was not expected to have a significant effect on the fitting procedure, because the key disease-related changes in the reflectance spectra were expected to be captured by changes in the variable L [32]. (3) The refractive index of cell nuclei for all tissue types was set to a constant value of 1.375, which was in good agreement with the previous results [32]. (4) The nuclear diameter L was varied from 9 μm to 13.5 μm, which contains the anticipated range for the pancreatic tissue types examined in this study [126, 127].

Table 2.4 Ranges and step sizes for tissue parameters in the PTI model [10].

Tissue parameter	Minimum value	Maximum value	Step size
L	9 μm	13.5 μm	0.9 μm
$[Hb]_{tot}$	2.5 μM	25 μM	2.5 μM
SO_2	0.1	0.9	0.2

In this way, the parameters extracted from the best fit of each "unknown" reflectance spectrum to the PTI model were the mean diameter L of the cell nuclei, as well as the total hemoglobin concentration and blood-oxygen saturation. The value of L from each "unknown" reflectance spectrum was compared to the value L_o (set to 9 μm) that had been input into the PTI model for the mean cellular nuclear diameter of the "canonical normal" tissue [32]. The ratio of L/L_o, termed the *nuclear enlargement factor*, was calculated for each "unknown" reflectance spectrum. The tissue scattering properties

extracted from the PTI model were then employed to correct the corresponding fluorescence spectra for attenuation artifacts.

Once the model described above was fit to an individual measured reflectance spectrum, the corresponding measured fluorescence spectrum $F_{MEASURED}(\lambda)$ was corrected for scattering and absorption attenuation artifacts with a Beer-Lambert factor [32], where the scattering coefficient was obtained from fitting the reflectance spectrum. The resulting "intrinsic" fluorescence spectrum $F_{INTRINSIC}(\lambda)$ was fit to a linear combination of the basis spectra from three endogenous tissue fluorophores: extracellular collagen, intracellular NADH, and intracellular FAD, as described previously [32]. The extracted fit coefficients C_{COLL}, C_{NADH}, and C_{FAD} were then normalized via division by their sum, in order to obtain the percentage contributions *%COLL*, *%NADH*, and *%FAD* from the constituent endogenous tissue fluorophores [32]. These percentages summed to 100% for each measured fluorescence spectrum.

Figure 2.6 shows representative reflectance and fluorescence spectra measured from normal pancreatic tissue, chronic pancreatitis, and pancreatic adenocarcinoma. As reported previously [28, 32, 128], there are noticeable differences between the spectra of the different tissue types. From 450 nm to 530 nm, there is a significant increase in the amplitude of the adenocarcinoma reflectance spectrum (relative to normal and chronic pancreatitis), attributed to the increased size of cell nuclei in adenocarcinoma [126, 127]. Near 400 nm, there are notable increases in the amplitude of the adenocarcinoma and

chronic pancreatitis fluorescence spectra (relative to normal), attributed to the increased extracellular collagen content in adenocarcinoma and chronic pancreatitis [112].

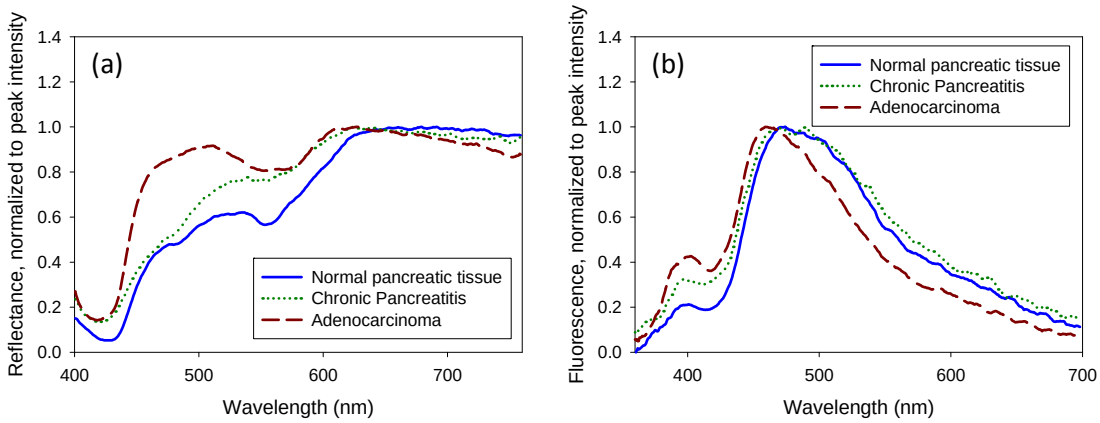

Figure 2.6 Representative (a) reflectance and (b) fluorescence spectra of normal pancreatic tissue, chronic pancreatitis, and pancreatic adenocarcinoma [10].

Figure 2.7 shows best fits of the PTI model to reflectance and fluorescence spectra from chronic pancreatitis and pancreatic adenocarcinoma. The average error in fit of the PTI reflectance model to the 96 measured spectra was less than 15% in the wavelength range 450-530 nm. This spectral range is where significant differences in spectral amplitude were reported for adenocarcinoma, relative to normal pancreatic tissue and pancreatitis [28, 32, 128], as can be seen in Figure 2.6(a). The average error in fit of the PTI fluorescence model to the 96 "intrinsic" fluorescence spectra was less than 6% in the wavelength range of 500-550 nm, in which key differences in spectral amplitude were reported [28, 32, 128] for the different pancreatic tissue types (see Figure 2.6(b)). When the 11 (out of 96) reflectance spectra with the highest cost functions were discarded, the average error in fit of the PTI reflectance model to the remaining 85 reflectance spectra fell below 10% in the 450-530 nm wavelength range, the average error in fit of the PTI fluorescence model to the 85 corresponding fluorescence spectra in the 500-550 nm

wavelength range was nearly unchanged (remaining at less than 6%), and there was no significant change to the mean or standard error for the extracted parameters.

Figure 2.8 shows the cellular nuclear enlargement factor L/L_o extracted from the PTI model for each pancreatic tissue type. The mean ± standard error values of L/L_o extracted for normal pancreatic tissue, chronic pancreatitis, and pancreatic adenocarcinoma were 1.03 ± 0.01, 1.05 ± 0.02, and 1.26 ± 0.02, respectively. The extracted parameter L/L_o can distinguish between adenocarcinoma and normal pancreatic tissue, as well as between adenocarcinoma and chronic pancreatitis ($p < 0.001$ from Wilcoxon rank-sum tests). This result is consistent with the larger average cellular nuclear diameters found in histopathological analysis of pancreatic adenocarcinoma relative to normal pancreatic tissue and chronic pancreatitis [111, 126, 127].

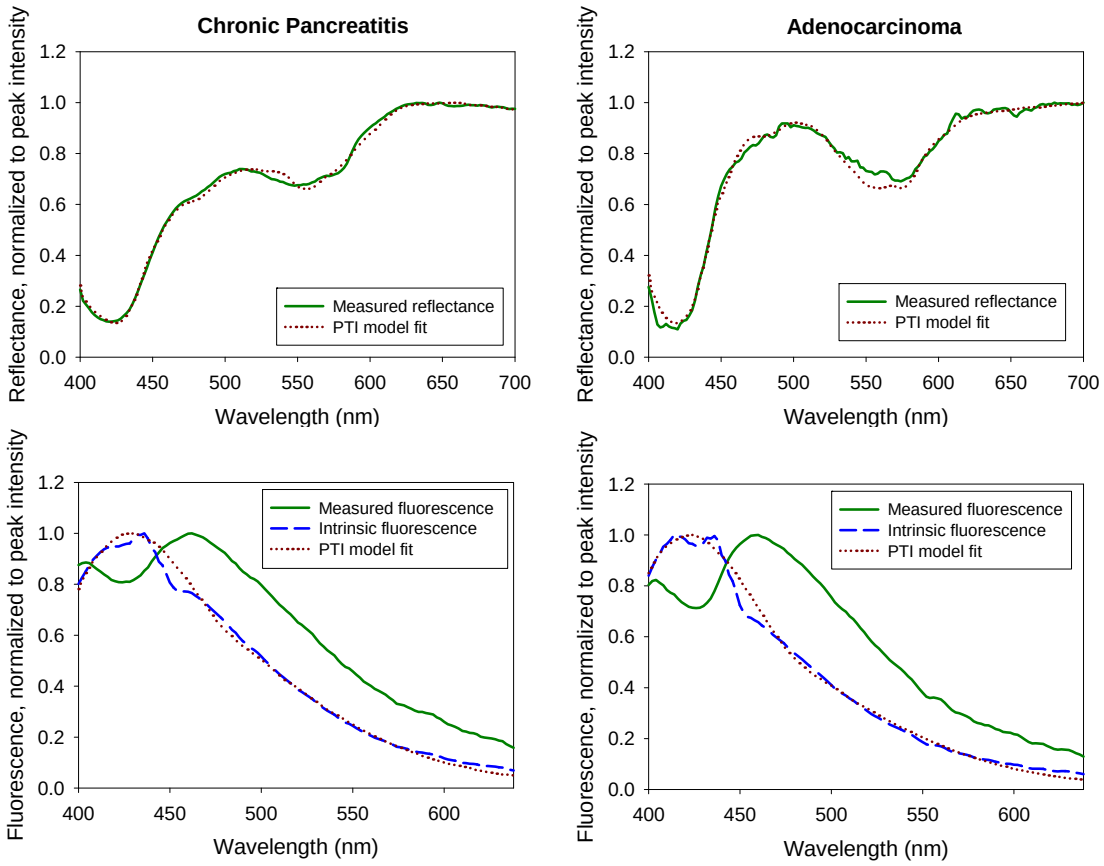

Figure 2.7 Best fits of the PTI model to measured reflectance spectra (top row) and intrinsic fluorescence spectra (bottom row) for chronic pancreatitis (left column) and adenocarcinoma spectra (right column) [10]. Over all measured spectra, the average error in fit of the PTI reflectance model was less than 15% in the wavelength range 450-530 nm, and the average error in fit of the PTI fluorescence model was less than 6% in the wavelength range of 500-550 nm.

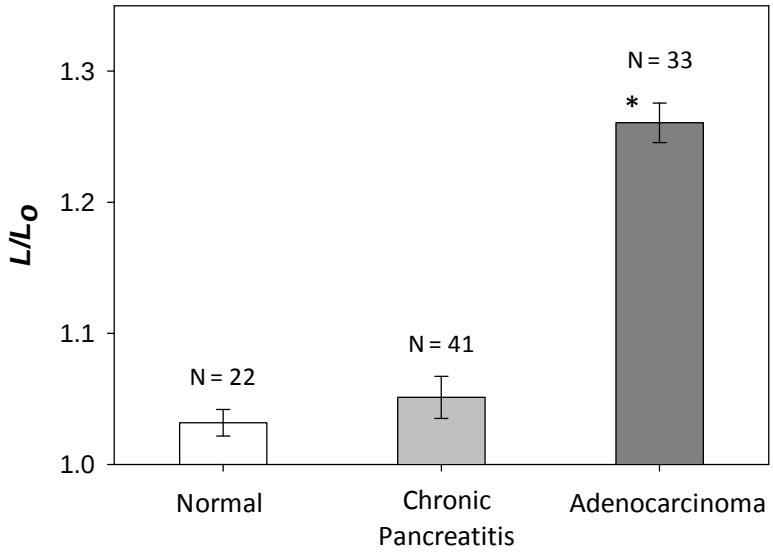

Figure 2.8 Extracted nuclear enlargement factor L/L_o for normal pancreatic tissue (N = 22 spectra), chronic pancreatitis (N = 41 spectra), and pancreatic adenocarcinoma (N = 33 spectra) [10]. Differences were statistically significant (*, $p < 0.001$ from Wilcoxon rank-sum tests) for distinguishing adenocarcinoma from normal pancreatic tissue as well as distinguishing adenocarcinoma from chronic pancreatitis.

Figure 2.9 shows the percentage contribution of extracellular collagen to the intrinsic fluorescence of normal pancreatic tissue, chronic pancreatitis, and pancreatic adenocarcinoma. The mean ± standard error values of the percent contributions of extracellular collagen fluorescence to the spectra of normal pancreatic tissue, pancreatitis, and adenocarcinoma were 15.5 ± 3.5, 28.7 ± 3.8, and 60.9 ± 4.8, respectively. The results shown in Figure 2.9 suggest that the percentage contribution of extracellular collagen to the intrinsic fluorescence is potentially useful (*, $p < 0.001$ from Wilcoxon rank-sum tests) for distinguishing adenocarcinoma from normal pancreatic tissue, as well as distinguishing adenocarcinoma from chronic pancreatitis. Figure 2.9 also shows that the percentage contribution of extracellular collagen to the intrinsic fluorescence is

potentially useful (**, $p < 0.05$ from Wilcoxon rank-sum test) for distinguishing chronic pancreatitis from normal pancreatic tissue. These results agree with qualitative histopathological observation [32, 129] and hydroxyproline content analysis [112], both of which have revealed increases in the amount of collagen found in chronic pancreatitis and pancreatic adenocarcinoma, relative to normal pancreatic tissue.

The results shown in Figures 2.8 and 2.9 suggest that reflectance and fluorescence spectroscopies have the potential to distinguish among pancreatic tissue types, including normal pancreatic tissues, chronic pancreatitis, and pancreatic adenocarcinoma, using biophysical tissue parameters extracted from the data via the PTI model of light propagation. The relevant biophysical parameters for distinguishing the different pancreatic tissue types were the nuclear enlargement factor L/L_o and the percentage contribution of extracellular collagen to the intrinsic fluorescence.

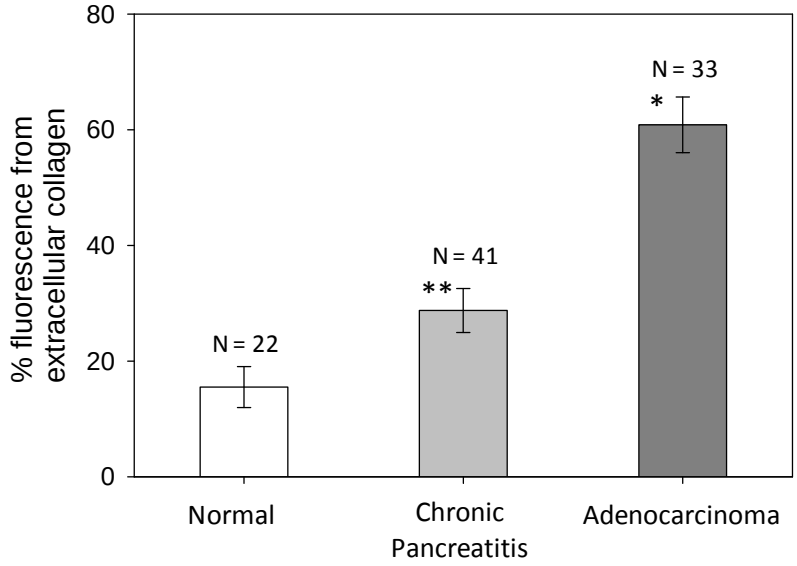

Figure 2.9 Extracted percentage contributions of extracellular collagen to intrinsic fluorescence spectra of normal pancreatic tissue (N = 22 spectra), chronic pancreatitis (N = 41 spectra), and pancreatic adenocarcinoma (N = 33 spectra) [10]. Differences were statistically significant for distinguishing adenocarcinoma from normal pancreatic tissue as well as distinguishing adenocarcinoma from chronic pancreatitis (*, $p < 0.001$ from Wilcoxon rank-sum tests). Differences were also statistically significant for distinguishing chronic pancreatitis from normal pancreatic tissue (**, $p < 0.05$ from Wilcoxon rank-sum test).

The observed increase in the nuclear enlargement factor L/L_o for adenocarcinoma, relative to normal pancreatic tissue and chronic pancreatitis, is in agreement with the findings of histopathology that the mean cellular nuclear diameter is larger in pancreatic adenocarcinoma than in normal pancreatic tissue [126] and chronic pancreatitis [127]. The increased percentage contributions of extracellular collagen to the intrinsic fluorescence for adenocarcinoma and chronic pancreatitis (relative to normal pancreatic tissue) are in agreement with studies demonstrating that there is increased collagen content in both pancreatic adenocarcinoma and tumor-associated chronic pancreatitis, relative to normal pancreatic tissue [112].

We note that since different source fibers were used for reflectance and fluorescence measurements, the light paths of the detected reflectance and fluorescence photons likely interrogated slightly different regions of each tissue site. However, since the reflectance and fluorescence photons were both collected by the same detector fiber, and all three fibers were positioned adjacent to each other in a triangular geometry, we used Monte Carlo simulations [37, 76, 77] to estimate that the majority of reflectance and fluorescence photons collected at a given tissue site visited roughly the same (~1 mm^3) region of tissue.

The PTI model reported here does not make use of the hemoglobin concentration and blood-oxygen saturation parameters extracted from the reflectance fits. Since the measurements used for training the PTI model in this study were all obtained *ex vivo*, much of the hemoglobin absorption information obtained from these measurements is likely most directly related to the amount of blood that drained from each tissue sample and the time that each sample was exposed to air prior to measurement. We note that the blood absorption features present in the measured reflectance spectra were likely similar for measurements made on patients who underwent either type of pancreatic surgery (Whipple procedure or distal pancreatectomy). This is a reasonable assumption because in the distal pancreatectomy procedure, the splenic artery was divided early, producing a level of ischemia that was likely similar to that associated with the Whipple surgery.

In an *in vivo* setting, we expect to see changes in the measured reflectance spectra that can be linked to differences in the vasculature and blood oxygenation (and hence, the hemoglobin absorption) of pancreatic adenocarcinoma, chronic pancreatitis, and normal pancreatic tissue [130, 131]. We also expect the PTI model to be capable of describing these changes in terms of the total hemoglobin concentration, blood-oxygen saturation, and mean blood vessel radius, as well as the possible addition of a variable to represent the packaging of hemoglobin into erythrocytes [117]. In preparation for future *in vivo* studies, we are working to further refine the PTI model and examine in greater detail the effect of the hemoglobin absorption parameters on the modeled reflectance. We do not anticipate that the accuracy of the PTI model will be significantly affected by the transition to an *in vivo* setting, since the model can account for increased levels of absorption due to blood. Thus, the results reported in this study illustrate the potential of the PTI model to address the clinical need for accurate detection of pancreatic adenocarcinoma in the setting of chronic pancreatitis. An optical sensing technique involving the PTI model could potentially be employed in a clinical setting to guide EUS-FNA biopsy.

In this study, we demonstrate the first-ever use of a photon-tissue interaction (PTI) model to fit individual reflectance and fluorescence spectra from human pancreatic tissues. The best fits of the PTI model to the optical spectra extracted diagnostically-relevant biophysical parameters. The nuclear enlargement factor was extracted from the PTI reflectance model, and the percent contribution of extracellular collagen to the intrinsic fluorescence was extracted from the PTI fluorescence model. Both of these parameters

were statistically significant for distinguishing pancreatic adenocarcinoma from normal pancreatic tissue, as well as for distinguishing adenocarcinoma from chronic pancreatitis. Furthermore, the percent contribution of extracellular collagen to the intrinsic fluorescence was also statistically significant for distinguishing chronic pancreatitis from normal pancreatic tissue. These results indicate that optical spectroscopy involving a photon-tissue interaction model has the potential to quantitatively distinguish between different pancreatic tissue types and to provide an inroad toward addressing the clinical need for accurate detection of early-stage pancreatic cancer.

2.3. Systematic verification of PTI model

As described previously in this dissertation, optical spectroscopic methods have the potential to provide quantitative, minimally invasive tissue assessment for applications such as cancer detection [3-6, 9, 10, 35, 128]. Reflectance spectroscopy can provide quantitative information about tissue scatterers (including size and concentration) and absorbers (including hemoglobin concentration and blood-oxygen saturation) [5, 9]. These parameters can be extracted by photon-tissue interaction (PTI) models based on diffusion theory [5, 9], Monte Carlo simulations [43], or semi-empirical equations [10, 32, 52]. Previously, we showed that a PTI model of reflectance has the potential to extract diagnostically-relevant parameters related to tissue morphology and biochemistry in the human pancreas [10, 32].

Figure 2.10 is a conceptual illustration (to scale) of the distribution of photons of 400 nm and 700 nm wavelength that have been launched from a fiber-optic probe into a pancreatic adenocarcinoma tissue site. The tissue model has been generated from a histology image of an adenocarcinoma site [32], where the cell nuclei have been stained purple and the extracellular collagen has been stained pink. Figure 2.10 shows the structural characteristics of the tissue (such as cell nuclei and extracellular collagen fibers) that are responsible for wavelength-dependent scattering of the incident light. Since these morphological features are expected to remain constant over the time period in which the measurements are taken, it is anticipated that optical spectroscopy can provide the ability to extract consistent values of tissue scattering properties even when the tissue absorption is changing due to variations in blood content.

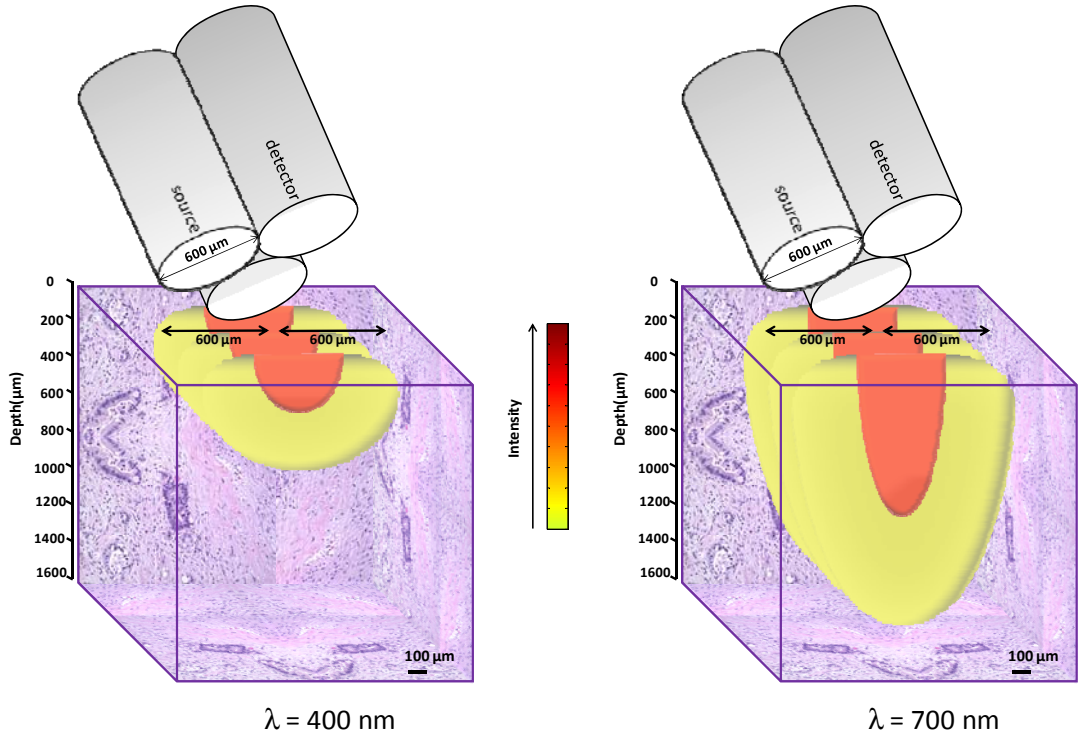

Figure 2.10 Conceptual illustration (to scale) of the distribution of 400 nm photons (left) and 700 nm photons (right) launched into a pancreatic adenocarcinoma tissue site with the fiber-optic probe configuration used in clinical studies. The distribution of photons within the tissue (orange and yellow glowball) is related to scattering from morphological tissue features (shown here as purple-stained cell nuclei and pink-stained extracellular collagen fibers). The probe appears tilted in this image so that the reader can see the bottom face of the fibers, but the probe was placed perpendicular to the tissue surface for all measurements reported in this study. The histology images are from [104] (used with permission).

Assessing optical spectroscopic methods for tissue diagnostics typically involves analyzing extracted tissue parameters to calculate their predictive accuracy for diagnostic classification [5, 6, 9, 10, 35, 43, 128]. Reported studies have analyzed a single measurement for each tissue site [5, 35], averaged repeated measurements [132], or considered multiple measurements acquired from the same site to be independent [9, 128]. We anticipate that the tissue scattering properties will remain the same between

repeated measurements, because the scattering properties are related to morphological quantities (such as the mean cellular nuclear diameter and the concentrations of cell nuclei and collagen fibers) that are not expected to vary significantly over a short time period. Quantifying the precision of optical spectroscopy in this manner is important for *in vivo* studies of any human tissue (where blood is dynamically flowing through the tissue, and measurements may be impacted by fiber-probe pressure or the puncture of a needle-based probe), as well as for *ex vivo* studies (where blood is draining from the tissue and becoming more oxygenated over time). Variations in blood content that occur *in vivo* can be linked to hypoxia and tissue vasculature [130, 131], so precisely assessing the effect of these variations is important for *in vivo* clinical studies.

Here we report the results of a more in-depth analysis of the PTI model. We begin with a systematic study of how individual absorption and scattering parameters affect the semi-empirical reflectance equations used in the PTI model. Then, we analyze how the PTI model is employed to mathematically transform an average measured "canonical normal" pancreatic tissue reflectance spectrum into an accurate model for pancreatitis (by increasing the collagen concentration) and adenocarcinoma (by increasing the collagen concentration and the mean size of the cell nuclei). The PTI model predictions are compared with average measured data from pancreatitis and adenocarcinoma to illustrate the effectiveness of the PTI model at linking changes in specific biophysically-relevant tissue parameters to specific changes in distinct regions of the reflectance spectrum. These systematic tests of the PTI model serve to separate the effects of the individual absorption and scattering parameters on the modeled reflectance. Once the effects of the

individual parameters have been characterized in this way, the effect of changing blood content on the extracted tissue parameters is investigated. We show that since the absorption and scattering parameters in the PTI model affect distinct regions of the modeled reflectance spectrum, the extracted scattering parameters remain consistent even for tissue sites at which the two measured spectra appear very different due to blood draining from the tissue over the course of measurement.

Prototype clinically-compatible instrumentation [28, 106] was developed, as described previously [28, 128], to acquire reflectance spectra from human pancreatic tissues within 30 minutes of resection during pancreatic surgery at the University of Michigan (U-M) Medical Center. The study received approval from the Institutional Review Board of the U-M Medical School, and written consent was obtained from all patients before measurement. Briefly, a tungsten-halogen lamp (Ocean Optics) was employed as the reflectance source and light from the lamp was directed onto the tissue surface with an optical fiber of 600 μm core diameter. Reflectance photons were colletced by a separate 600 μm diameter detector fiber placed adjacent to the source fiber. Light from the detector fiber was directed toward a spectrograph-coupled ICCD camera for spectral detection.

Optical data was acquired from nine patients within 30 minutes of excision of the pancreatic tissue. Prior to measurement, excess blood was wiped off of the tissue with gauze. The on-site pathologist then identified sites of interest on the excised tissue and the optical probe was placed on those tissue sites for data acquisition. Some of these sites

were beneath the surface of the tissue; in these cases the tissue was cut in order to provide access to the fiber-probe. At each site, the probe was held in position by hand and its position was monitored by the pathologist and the person taking the measurement. Two sets of measurements of steady-state reflectance, steady-state fluorescence, and time-resolved fluorescence decay were made at each site without removing the probe. Each set of measurements took approximately 40 seconds to obtain. After completion of the measurements at a given site, the probe was removed and the pathologist immediately excised a portion of the tissue from that site for histopathologic analysis, which was considered the "gold-standard" for this study. In this manner, optical measurements were obtained at 5 to 10 sites from each patient, depending on the size of the resected tissue sample. Non-usable measurements (for which the fluorescence signal-to-noise ratio was less than 25, or for which the reflectance intensity at 550 nm was below 10% of the intensity at 650 nm due to hemoglobin absorption dominating the detected signal) were discarded. The analysis presented in this paper was performed on the subset of the data for which two usable measurements were taken from each site. This subset contained 47 sites (11 normal, 20 chronic pancreatitis, 16 adenocarcinoma), and since two reflectance measurements were taken at each site, there were a total of 94 measured reflectance spectra.

It is important to note that in this study, the variations in tissue blood content were not experimentally-controlled. Absorption-related variations were observed in the two reflectance spectra acquired at each site, and it was presumed that this variability was caused by changes in the concentration and oxygenation of blood in the freshly-excised

tissues. This hypothesis makes sense because variations in tissue blood content are known to occur post-resection and these variations have been shown to impact the measured optical spectra [28, 133].

A PTI model using semi-empirical reflectance equations [52, 93] (as described previously [10, 32]) was employed to extract absorption- and scattering-related tissue parameters (Table 2.5) from the measured reflectance spectra.

Table 2.5 Tissue parameters that can be extracted by PTI reflectance model.

Scattering	Absorption
Mean diameter of cell nuclei, $<L>$	Total hemoglobin concentration, $[Hb]_{tot}$
Refractive index of cell nuclei, n_s	Blood-oxygen saturation, SO_2
Concentration of collagen fibers, ρ_c	Mean blood vessel radius, r_{bl}

Figure 2.11 illustrates the components of the PTI model. The starting point of the PTI model is an average measured "canonical normal" reflectance spectrum, $N_{measured}(\lambda)$, obtained by averaging all reflectance measurements from normal tissue sites in the data set. This "canonical normal" spectrum is then mathematically transformed to produce a PTI model spectrum $R_{PTI}(\lambda)$ that is fit to an individual reflectance measurement of "unknown" tissue type. This mathematical transformation takes the form:

$$R_{PTI}(\lambda) = N_{measured}(\lambda)\frac{R_{empirical}(\lambda)}{N_{empirical}(\lambda)}. \quad (11)$$

In Eq. (11), $R_{empirical}(\lambda)$ and $N_{empirical}(\lambda)$ are semi-empirical equations describing the "unknown" reflectance measurement and the "canonical normal" reflectance, respectively. Both of these semi-empirical equations take the following general form $R(\lambda)$ [52, 93]:

$$R(\lambda) = \mu_s'(\lambda) \exp\left(-\frac{C_{corr}\mu_a(\lambda)b}{\left[C_{corr}(\lambda)\mu_a(\lambda)\mu_s'(\lambda)\right]^c} \right). \quad (12)$$

In Eq. (12), $\mu_a(\lambda)$ is the tissue absorption coefficient and $\mu_s'(\lambda)$ is the reduced scattering coefficient, defined as $\mu_s'(\lambda) = \mu_s(\lambda)(1-g)$, where g is the anisotropy (set equal to 0.9 here) [32]. The variables b and c are related to tissue and fiber-probe properties [93]. Tissue scattering was attributed to cell nuclei (modeled as spheres [5, 107] with mean diameter $<L>$ and refractive index n_s) and collagen fibers (modeled as cylinders [33] with concentration ρ_c). Tissue absorption was attributed to oxy- and deoxy-hemoglobin [5, 52, 125], with a correction factor $C_{corr}(\lambda)$ that accounted for the confinement of blood to cylindrical blood vessels [114] with mean radius r_{bl}. From each reflectance measurement, a cellular nuclear enlargement factor L/L_o and the total hemoglobin concentration $[Hb]_{tot}$ were extracted [10, 32]. The nuclear enlargement factor was a ratio between the mean (ensemble average) diameter $<L>$ of cell nuclei at a given site and the mean size L_o of normal pancreatic cell nuclei [32]. The value of L/L_o was previously shown to be larger for adenocarcinoma than for normal pancreatic tissue or pancreatitis, a result that agreed with histopathological observation [10, 32].

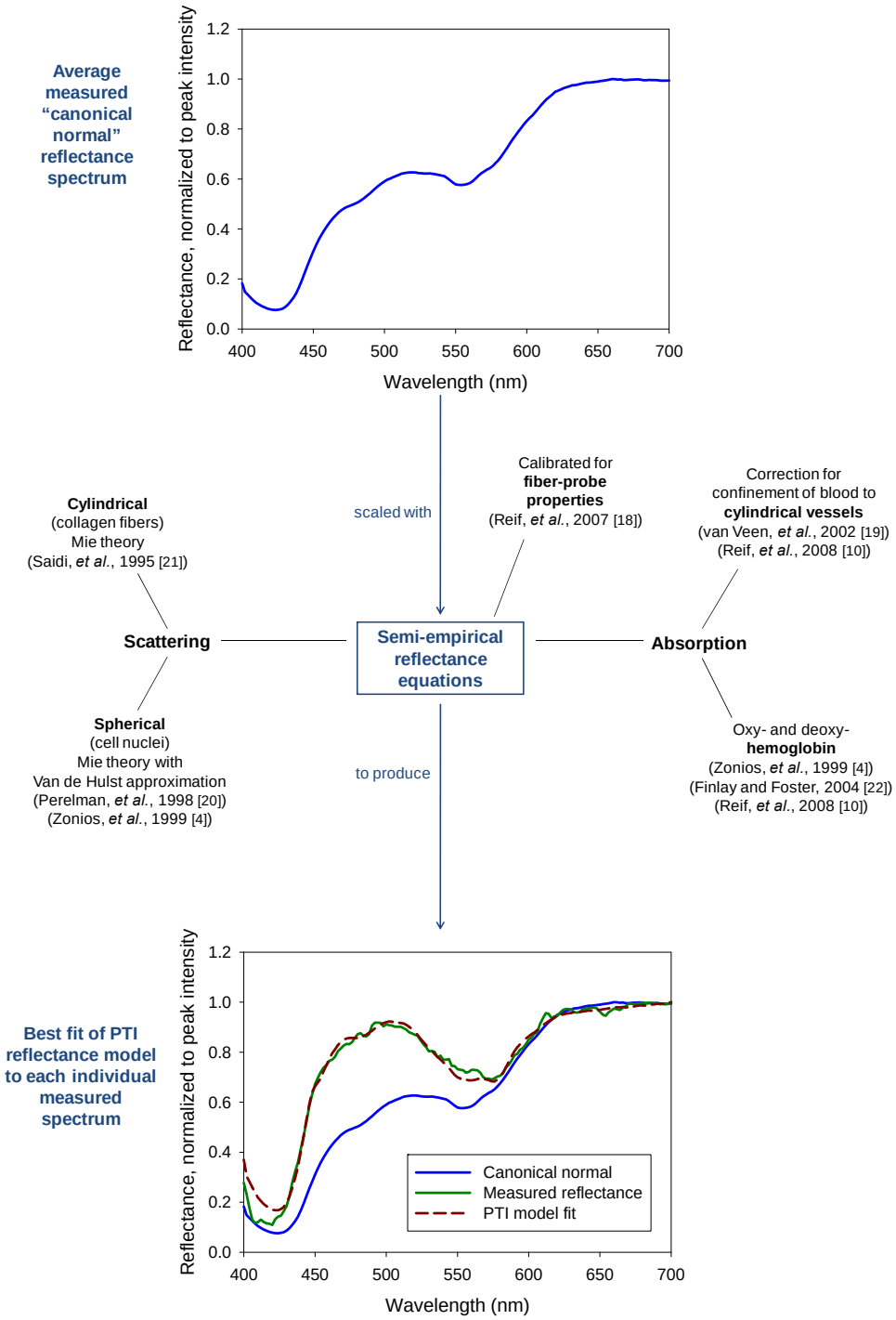

Figure 2.11 Conceptual illustration of photon-tissue interaction (PTI) model employed to extract pancreatic tissue properties from measured reflectance spectra. The best fit PTI model is from [10] and the canonical normal is from [128] (used with permission).

To systematically examine the effect of the different tissue properties on the semi-empirical reflectance equation $R_{empirical}(\lambda)$, the total hemoglobin concentration, blood-oxygen saturation, mean nuclear diameter, and nuclear refractive index were varied individually while all of the remaining parameters were kept constant. Figure 2.12 shows the effect of each of these variations.

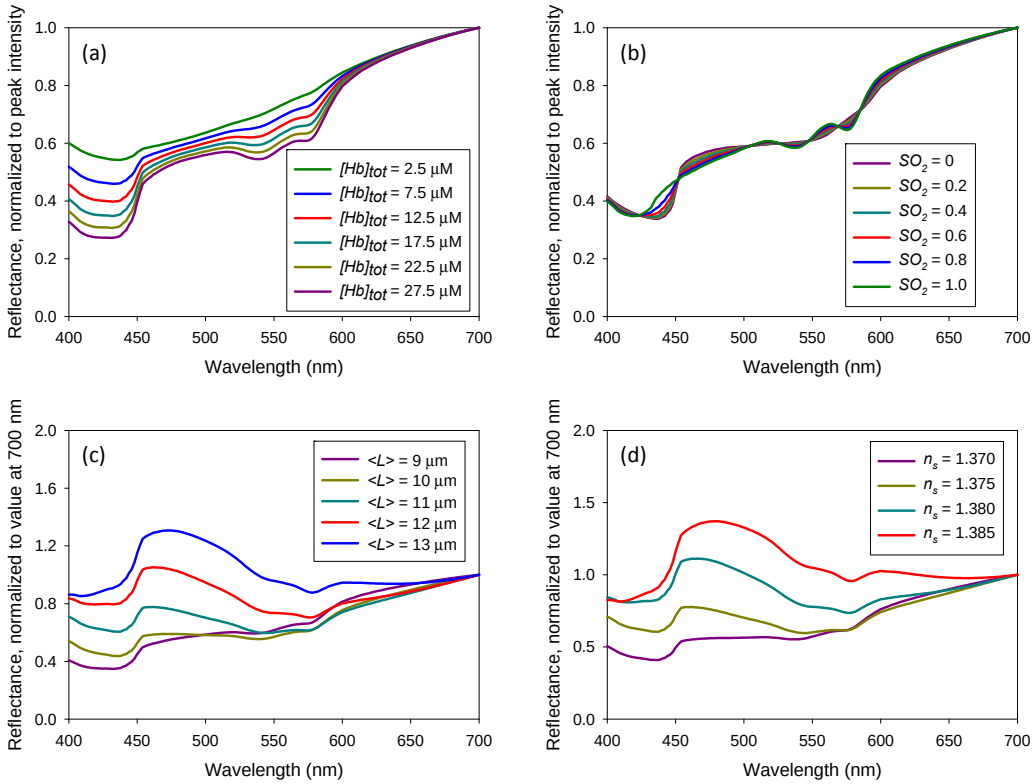

Figure 2.12 Systematic examination of changes in the semi-empirical reflectance $R_{empirical}(\lambda)$ when four different tissue parameters are individually varied: (a) Varying only the total hemoglobin concentration $[Hb]_{tot}$; (b) Varying only the blood-oxygen saturation SO_2; (c) Varying only the mean nuclear diameter $\langle L \rangle$; (d) Varying only the nuclear refractive index n_s. It can be seen from (a) and (b) that changes in the absorption parameters primarily affect the spectra from 400-450 nm and 525-600 nm while (c) and (d) show that changing the scattering parameters also has a significant effect on the spectra from 450-525 nm.

From Figures 2.12(a) and 2.12(b), it can be seen that changing the hemoglobin concentration and blood oxygenation primarily affects the amplitude of the reflectance from 400-450 nm and from 525-600 nm. Figure 2.12(c) shows that changing the mean nuclear diameter has a significant effect on the amplitude of the modeled reflectance in the 450-525 nm range. This result is consistent with the experimentally-observed trend that reflectance spectra from pancreatic adenocarcinoma (which is expected to exhibit enlarged cell nuclei) typically have higher amplitude in the 450-525 nm range than the spectra of normal pancreas or pancreatitis [10, 128]. Figures 2.12(c) and 2.12(d) both illustrate that changing the tissue scattering properties can affect the slope of the reflectance spectrum between 600 nm and 700 nm.

The results in Figure 2.12 are consistent with the experimentally-observed trends that reflectance spectra of adenocarcinoma, pancreatitis, and normal pancreatic tissue have different amplitudes in the 450-525 nm wavelength range and different slopes in the 600-700 nm wavelength range [10, 128]. These findings suggest that the semi-empirical reflectance equation (Eq. (12)) is sensible to incorporate into the PTI model because it has the potential to link specific biophysically-relevant tissue parameters to specific trends in the measured reflectance spectra that are related to the progression of pancreatic disease.

Figure 2.13 illustrates how Eqs. (11) and (12) can be employed to mathematically transform an average measured "canonical normal" spectrum (obtained here by averaging 22 reflectance measurements from normal pancreatic tissues [128]) into a PTI reflectance

model $R_{PTI}(\lambda)$ for pancreatic tissues with different scattering properties. In Figure 2.13(a), the concentration ρ_c of the collagen fibers is varied, and in Figure 2.13(b), the mean size $<L>$ of the cell nuclei is varied. In both cases, the region of the spectrum from 450-525 nm is most prominently affected.

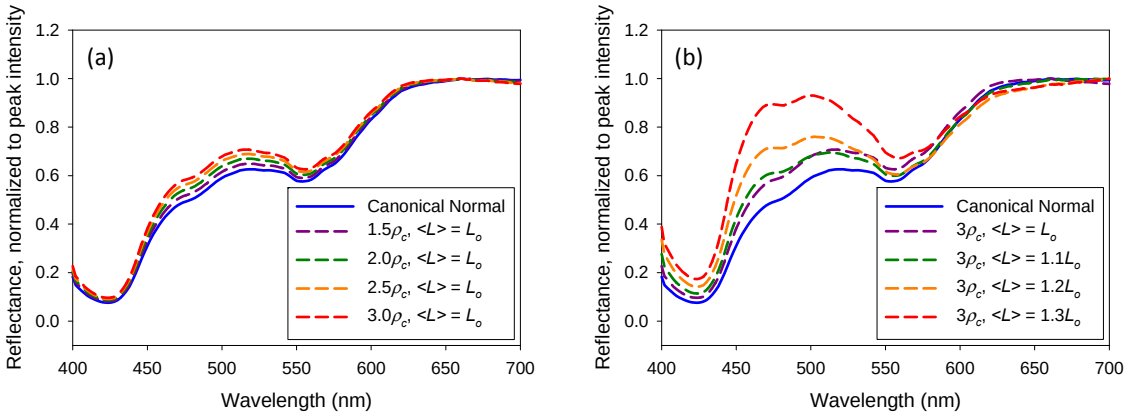

Figure 2.13 Effect of changes in two different scattering parameters on PTI reflectance model $R_{PTI}(\lambda)$: (a) varying values of the collagen concentration ρ_c and (b) varying values of the mean nuclear size $<L>$. Changing the collagen concentration has a subtle effect on the reflectance lineshape from 450-525 nm, while changing the mean nuclear size has a much more notable effect on the reflectance in this region. The canonical normal spectrum is from [128] (used with permission).

Using Figure 2.13 as a guideline, Figure 2.14 shows how some key features of the reflectance spectra from the PTI model (Figure 2.14(a)) match up with those of average measured reflectance data from pancreatitis and adenocarcinoma (Figure 2.14(b), [128]). First, the mean nuclear size is kept constant but the collagen concentration is multiplied by a factor of three, which has been shown in the medical literature to be indicative of both pancreatitis and adenocarcinoma [112]. In this case, the PTI reflectance model (dot-dashed green line in Figure 2.14(a)) looks similar to the average measured reflectance from pancreatitis (dot-dashed green line in Figure 2.14(b)). This result is consistent with

the observation at histopathology that pancreatitis is characterized by increased extracellular collagen but no significant increase in the mean size of cell nuclei (relative to normal tissue) [32]. Next, the concentration of collagen is kept at three times that of normal tissue, but the mean nuclear size $<L>$ is increased from its initial value of L_o to a value of $1.25L_o$. For this larger value of $<L>$, one can see the similarity between the PTI reflectance model (dashed red line in Figure 2.14(a)) and the average measured reflectance from adenocarcinoma (dashed red line in Figure 2.14(b)). This result agrees with the observation at histopathology that adenocarcinoma is characterized by increased extracellular collagen and enlarged cell nuclei [32].

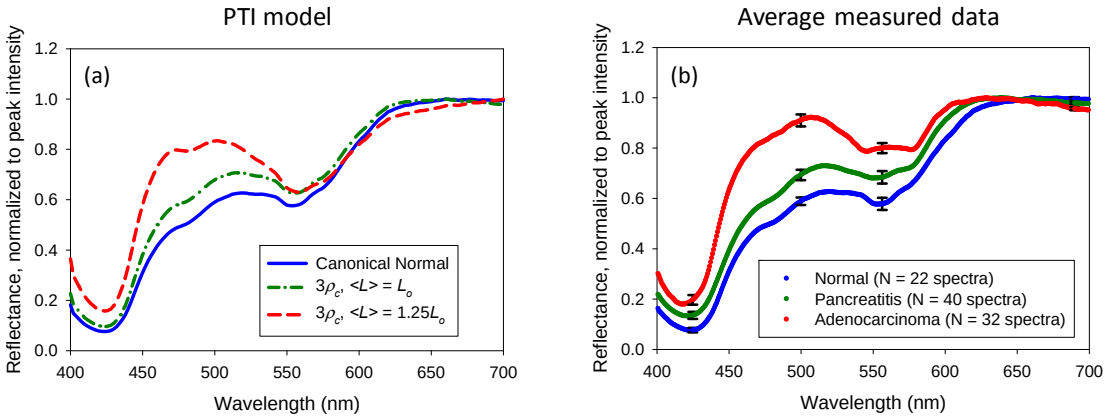

Figure 2.14 Demonstration of PTI reflectance models $R_{PTI}(\lambda)$ for various combinations of tissue scattering parameters (a), shown alongside average measured data from human pancreatic tissues (b) [128] (used with permission). When the concentration of collagen is increased to three times that of normal pancreatic tissue but the mean size of the cell nuclei is left unchanged (dot-dashed green line in (a)), there is a clear similarity between the PTI model and the measured data from pancreatitis (dot-dashed green line in (b)), relative to normal (blue lines in (a) and (b)). As the mean diameter of the cell nuclei is increased and the concentration of collagen is kept at three times that of normal tissue, the PTI model (dashed red line in (a)) looks similar to the average measured reflectance from adenocarcinoma (dashed red line in (b)), relative to normal. In particular, the increase in collagen concentration provides a subtle change in the reflectance from 450-525 nm (as shown in Figure 2.13(a)), while the increase in nuclear size is responsible for the more pronounced change in the reflectance in this region (as shown in Figure 2.13(b)). The error bars in (b) represent the standard error. The canonical normal spectrum is from [128] (used with permission).

The PTI model was fit to each of the two reflectance spectra acquired from all 47 sites. In the fitting procedure [10], the value of the nuclear enlargement factor L/L_o was varied from 1.0 to 1.5 (in steps of 0.1), and the value of the total hemoglobin concentration $[Hb]_{tot}$ was varied from 1.1 μM to 11 μM (in steps of 1.1 μM). For each measurement, the best fit of the PTI model to the data was defined to be the fit that minimized the cost function $C_R = \Sigma|R_{measured}(\lambda) - R_{PTI}(\lambda)|$, where $R_{measured}(\lambda)$ was the measured reflectance spectrum, $R_{PTI}(\lambda)$ was the PTI reflectance model, and Σ represented a sum over all wavelengths from 400-700 nm. For each site, the values of L/L_o and $[Hb]_{tot}$ extracted from the best fits were compared for the two measurements. The PTI model fits were examined in the 430-500 nm range (where changes in scattering have been shown to distinguish the adenocarcinoma spectra from the normal and pancreatitis spectra [32]).

Sites at which there was a significant degree of difference between the two reflectance measurements $R_1(\lambda)$ and $R_2(\lambda)$ were identified by using the manually-selected criterion $\Sigma(R_2(\lambda)-R_1(\lambda))^2 > 1.8$. Here, Σ denotes a sum over all wavelengths between 400 nm and 700 nm (the same range over which the PTI model was fit to each reflectance spectrum). Using this criterion, it was found that 18 of the 47 sites exhibited significant variation between the two measured reflectance spectra. For the remaining 29 sites, the two reflectance measurements were very similar, thereby illustrating the capability of the instrumentation and experimental protocol to provide consistent measurements.

Figure 2.15(a) shows two measured reflectance spectra (solid lines) from a single adenocarcinoma site, along with the corresponding fits of the PTI model (dashed lines) to

each spectrum. According to the criterion described previously, the two measurements shown in Figure 2.15(a) were not considered to be significantly different. As expected, the extracted values of the nuclear enlargement factor L/L_o and the mean reduced scattering coefficient $<\mu_s'>$ were identical for the two measurements.

Figure 2.15(b) shows two measured reflectance spectra (solid lines) from a second adenocarcinoma site, along with the corresponding fits of the PTI model (dashed lines) to each spectrum. Here, according to the criterion described previously, the two measurements were considered to be significantly different. However, the extracted values of the nuclear enlargement factor L/L_o and the mean reduced scattering coefficient $<\mu_s'>$ were still identical for the two measurements. These results demonstrate the ability of the PTI model to extract consistent values of the tissue scattering properties even when there are noticeable variations in the amount of blood at a given site.

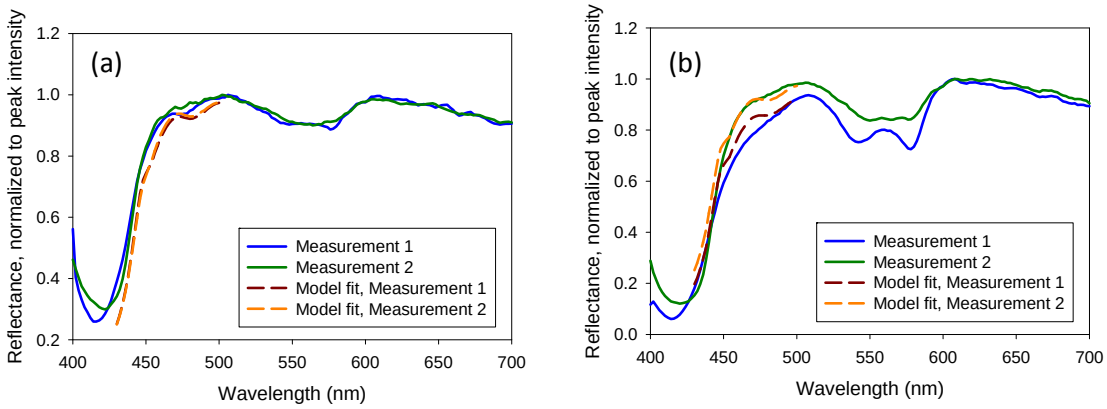

Figure 2.15 Pairs of reflectance measurements (solid blue curves, solid green curves) acquired from two different adenocarcinoma sites, shown with the corresponding fits of the PTI model (red dashed curves, orange dashed curves) to the measured spectra from 430-500 nm. For the site shown in (a), the two measured spectra were very similar, and the values of the nuclear enlargement factor L/L_o and mean reduced scattering coefficient $<\mu_s'>$ extracted from the two spectra were identical. For the site shown in (b), the two measured spectra looked significantly different (likely due to changes in the absorption caused by the draining of blood from the freshly excised tissue), and the $[Hb]_{tot}$ values extracted from the two spectra differed by 22.5 μM, but the values of the nuclear enlargement factor L/L_o and mean reduced scattering coefficient $<\mu_s'>$ extracted from the two spectra were still identical. This result illustrates the ability of the PTI model to extract consistent values of tissue scattering parameters even when the blood content of the tissue was changing over time.

Figure 2.16(a) shows a histogram of the differences between the total hemoglobin concentration values $[Hb]_{tot}$ acquired at the sites (N = 29) for which there was no significant difference between the two measured spectra (including the site shown in Figure 2.15(a)) according to the criterion described previously. Figure 2.16(b) shows the corresponding histogram of the differences between the L/L_o values extracted from the two reflectance spectra from each of these sites. The differences $\Delta[Hb]_{tot}$ and $\Delta L/L_o$ were defined as $[Hb]_{tot2}$-$[Hb]_{tot1}$ and $(L/L_o)_2$-$(L/L_o)_1$, respectively, where the subscripts 1 and 2 denoted the first and second measurements taken from a given site. For 23 of these 29 sites (79%), the $[Hb]_{tot}$ values extracted from the two measurements differed by less than

10 μM. Furthermore, for this set of 29 sites, the average difference between the L/L_o values extracted from the two measurements was less than 2% and the average difference between the $<\mu_s'>$ values extracted from the two measurements was less than 1%. These results demonstrate the robustness of the data collection method and the stability of the PTI model.

Figure 2.16(c) shows a histogram of the differences between the $[Hb]_{tot}$ values extracted from the two reflectance spectra acquired at the sites (N = 18) for which there were significant differences between the two measured spectra (including the site shown in Figure 2.15(b)) according to the criterion described previously. Figure 2.16(d) shows the corresponding histogram of the differences between the L/L_o values extracted from each of these sites. For 8 of the 18 sites (44%), the $[Hb]_{tot}$ values from the two measurements differed by at least 10 μM. However, the average difference between the L/L_o values extracted from the two measurements was less than 6%. Figure 2.16(d) shows that for 16 of the 18 sites (89%), the magnitude of $\Delta L/L_o$ was no greater than 0.1 (the step size for L/L_o in the PTI fitting procedure described previously). In addition, the average difference between the $<\mu_s'>$ values extracted from the two measurements was less than 2%. Overall, larger variations in hemoglobin concentration did not have a notable effect on the precision with which the PTI model extracted the nuclear enlargement factor and mean reduced scattering coefficient. These results indicate that the PTI model extracted consistent values of the tissue scattering properties even when the tissue blood content was varying.

For each tissue type, the five sites for which the two reflectance measurements were the most different from each other were determined by maximizing the function $Diff(R_1(\lambda),R_2(\lambda)) = \Sigma(R_2(\lambda)-R_1(\lambda))^2$, where $R_1(\lambda)$ and $R_2(\lambda)$ were the two reflectance spectra measured from each site and Σ represented a sum over the wavelengths from 400-700 nm. For this reduced data set, the mean L/L_o value for adenocarcinoma was still 20% larger than that of normal pancreatic tissue and 15% larger than that of pancreatitis. Using Wilcoxon rank-sum tests, the *p*-value for using L/L_o to distinguish adenocarcinoma from non-malignant tissue (normal and pancreatitis) was still statistically significant ($p < 0.001$) for this reduced data set. These results suggest that the PTI algorithm has the potential to distinguish between different pancreatic tissue types even when the measured spectra from a single site were significantly different.

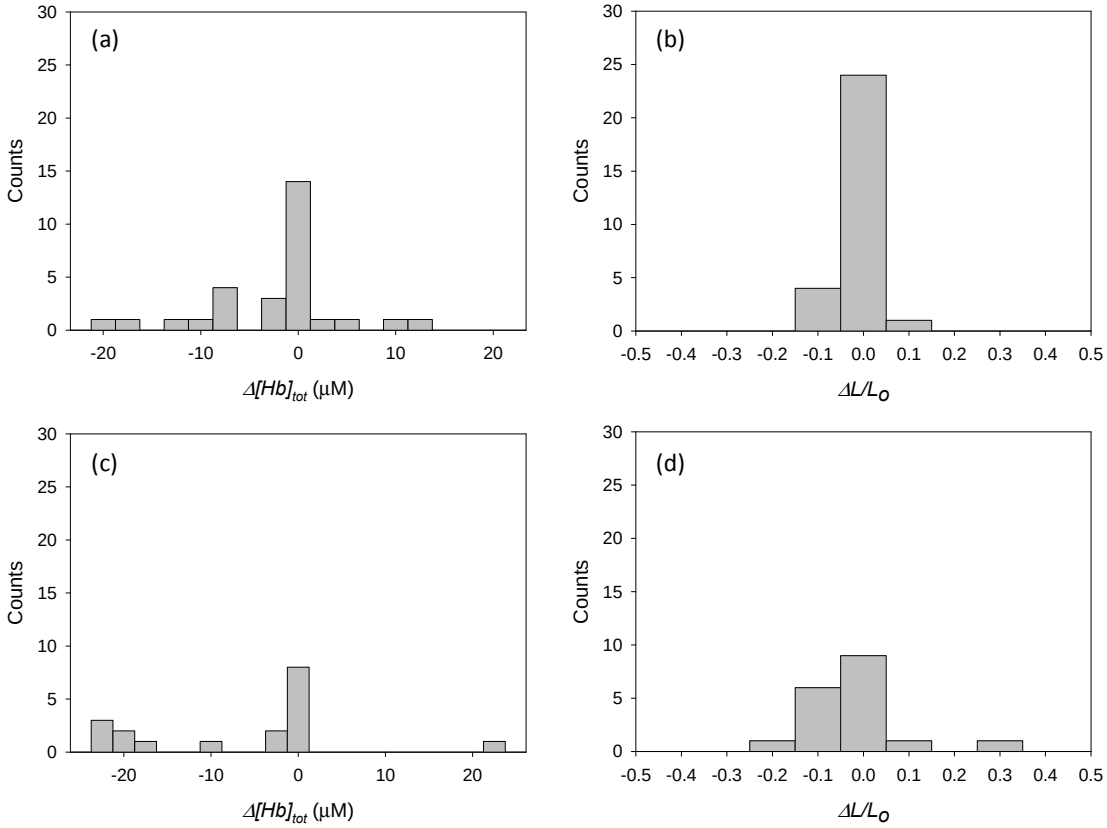

Figure 2.16 Histograms of differences in extracted values of the total hemoglobin concentration ($\Delta[Hb]_{tot}$) and nuclear enlargement parameter ($\Delta L/L_o$) for (a, b) the 29 pancreatic tissue sites at which the two measured reflectance spectra were not significantly different from each other, and (c, d) the 18 pancreatic tissue sites at which the two measured reflectance spectra were significantly different from each other. When the two reflectance measurements were not significantly different, the magnitude of $\Delta[Hb]_{tot}$ (a) was less than 10 μM for 23 of 29 sites (79%), and the average difference between the two extracted L/L_o values (b) was less than 2%. When the two reflectance measurements were significantly different, the magnitude of $\Delta[Hb]_{tot}$ (c) was less than 10 μM for only 10 of the 18 sites (56%), but the average difference between the two extracted L/L_o values (d) was still less than 6%.

Here we have reported the development of a photon-tissue interaction (PTI) model for extracting biophysically-relevant tissue absorption and scattering parameters from measured reflectance spectra. The model uses semi-empirical equations to scale an average measured "canonical normal" reflectance spectrum such that disease-related changes in the reflectance spectra are quantitatively linked to parameters related to tissue

structure (such as mean size of cell nuclei and concentration of collagen fibers). The effect of the different tissue properties on the semi-empirical reflectance equations was systematically examined. In addition, we have demonstrated the potential of optical spectroscopy to provide consistent values of tissue scattering parameters at a given tissue site, even when the measured spectra at that site are varying noticeably in time due to changes in absorption from blood. Future work will investigate the extension of this study to tissue fluorescence, as well as to tissue optical spectra acquired *in vivo*. These results illustrate the feasibility of employing optical spectroscopy for consistent characterization of disease-related changes in human pancreatic tissues, and these findings should also be applicable to a wide range of other tissue types.

2.4. Tissue classification

As mentioned previously, pancreatic cancer is the fourth-leading cause of cancer death in the United States, with a five-year survival rate of only 6% [95]. This statistic is largely due to the fact that currently-used diagnostic methods cannot reliably detect the disease in its early stages [96]. Therefore, it is necessary to find a more accurate method for pancreatic cancer diagnostics. Here, we develop and employ clinically-compatible optical spectroscopy technology for accurate classification of pancreatic cancer, reliably distinguishing the disease from non-cancerous pancreatic tissues (normal and pancreatitis). The tissue optical data were analyzed with mathematical models and a statistically rigorous tissue classification algorithm, and the results were compared with those of biopsy and histopathology, which is the diagnostic gold standard. The optical method accurately classified pancreatic cancer sites, with a sensitivity, specificity, positive predictive value, and negative predictive value of 87.5%, 89.0%, 77.8%, and 94.2%, respectively. These results suggest that optical spectroscopy has the potential to distinguish pancreatic cancer from non-malignant pancreatic tissues.

Clinically-compatible instrumentation [28, 106, 128] was employed to acquire reflectance and fluorescence spectra from freshly-excised human pancreatic tissues from an expanded data set of 18 patients. Measurements were taken at multiple sites from each patient; 39 normal sites, 34 pancreatitis sites, and 32 adenocarcinoma sites were used in the analysis. Visually noticeable differences among the tissue types were observed in both the reflectance and the fluorescence spectra. To analyze these differences, two

mathematical models were employed: a Principal Component Analysis (PCA) model [134], and a Photon-Tissue Interaction (PTI) model [10, 32].

Prior to data analysis, outlier spectra were removed from the data set. Reflectance spectra for which the detected signal at 550 nm was less than 1/5 of that at 650 nm were removed because these spectra were dominated by absorption from blood. Fluorescence spectra with a signal-to-noise ratio of less than 30 were also removed, because these spectra were considered too noisy to properly analyze.

In addition, a residual-based method was employed to detect sites where the two measured fluorescence or reflectance spectra were extremely different from each other. This was done through a series of linear mixed models where the spectrum measurements at specific wavelengths were regressed on the tissue diagnosis with a random intercept to account for correlation among sites which originated from the same patient. Ten regressions were performed on the fluorescence spectra at wavelengths of 375.18, 417.19, 423.38, 427.52, 444.04, 452.99, 466.08, 479.16, 502.57, and 511.52 nm, and ten regressions were also performed on the reflectance spectra at wavelengths of 426.827, 440.598, 461.255, 481.913, 490.175, 541.130, 544.573, 612.053, 625.135, and 755.964 nm. Transformations were necessary to ensure that the spectra measurements had a Gaussian shape necessary for the linear regressions. For each of the regressions the difference between the residuals of the two duplicate measurements at each site were calculated and ranked in order of magnitude. The ranks for the ten regressions were then averaged to give an overall fluorescence or reflectance average rank for each site. Sites

whose overall mean rank exceeded the 85th percentile of the total number of sites were flagged as potential outliers. Through this method five sites were identified as having a pair of very different reflectance spectra, and four sites were identified as having a pair of very different fluorescence spectra. Sites with extremely different measurements were removed from the analysis, and for the remaining sites, the two measured spectra were averaged. Of the 117 sites from which measurements were acquired, 12 sites were flagged as outliers and removed from the data set.

The PCA model extracted the principal components from each measured reflectance and fluorescence spectrum (Figure 2.17). The PCA code was written in MATLAB using functions that were built into the MATLAB programming language. The values of the principal components and their statistical significance for distinguishing between the tissue types are displayed in Table 2.6. The first reflectance principal component ($p < 1x10^{-4}$) and the first fluorescence principal component ($p < 1x10^{-4}$) were the most statistically-significant PCA variables for distinguishing adenocarcinoma from normal pancreatic tissue. The first reflectance principal component ($p < 9x10^{-3}$) and the first fluorescence principal component ($p < 3x10^{-3}$) were also the most statistically significant PCA variables for distinguishing adenocarcinoma from pancreatitis.

As described previously, the PTI model algorithm [10, 32] fit mathematical models of reflectance and fluorescence to the measured optical data to extract parameters related to tissue structure and biochemical composition. The PTI model was written in MATLAB employing a combination of previously-used equations [5, 33, 49, 51, 52, 93, 114, 125] to

model the measured reflectance and fluorescence as functions of tissue properties related to absorption, scattering, and concentration of endogenous tissue fluorophores. These parameters included the nuclear enlargement factor L/L_o and the total hemoglobin concentration $[Hb]_{tot}$, from the reflectance and the percentage contributions of extracellular collagen and intracellular NADH and FAD to the fluorescence. The extracted values of the PTI model parameters and their statistical significance for distinguishing between the tissue types are displayed in Table 2.6. The nuclear enlargement factor ($p < 1\text{x}10^{-4}$) and the percentage contribution of collagen ($p < 1\text{x}10^{-4}$) were the most statistically significant PTI variables ($p < 2\text{x}10^{-2}$) for distinguishing adenocarcinoma from normal pancreatic tissue. The nuclear enlargement factor ($p < 2\text{x}10^{-2}$) and the percentage contribution of collagen ($p < 3\text{x}10^{-2}$) were also the most statistically significant PTI variables for distinguishing adenocarcinoma from pancreatitis.

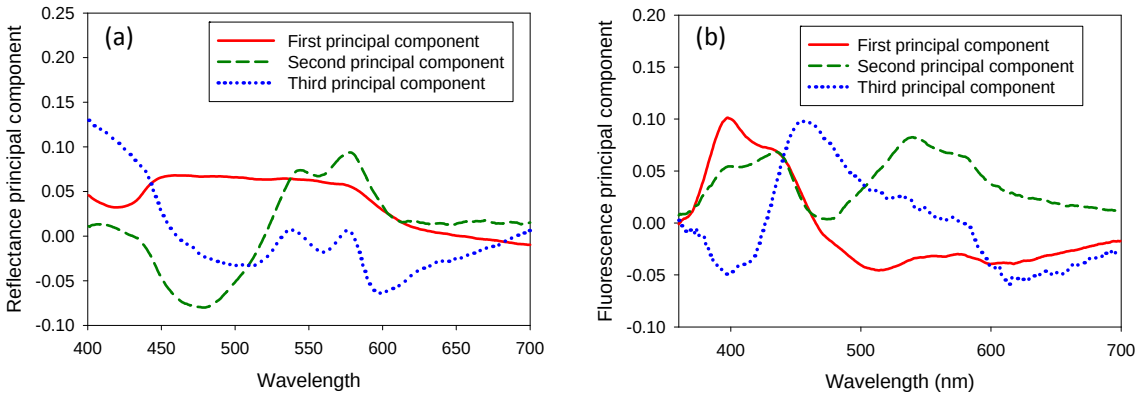

Figure 2.17 (a) First three principal components of the reflectance data set. These three principal components explained 95% of the variation in the measured reflectance spectra. (b) First three principal components of the fluorescence data set. These three components explained 95% of the variation in the measured fluorescence.

Table 2.6 Mean, standard error, and significance of PCA and PTI model parameters.

Variable	Mean ± Standard Error for N	Mean ± Standard Error for P	Mean ± Standard Error for A	*p*-value for A vs. N	*p*-value for A vs. P
RPC1	-2.35 ± 0.25	-0.01 ± 0.30	2.87 ± 0.35	<0.001	0.0089
RPC2	-0.07 ± 0.10	0.37 ± 0.16	-0.30 ± 0.10	0.2905	0.0200
RPC3	0.20 ± 0.05	-0.22 ± 0.07	-0.01 ± 0.13	0.5708	0.2086
FPC1	-1.69 ± 0.19	-0.33 ± 0.27	2.40 ± 0.37	<0.001	0.0026
FPC2	-0.40 ± 0.18	0.56 ± 0.25	-0.11 ± 0.21	0.2066	0.1112
FPC3	-0.09 ± 0.10	0.11 ± 0.08	0.00 ± 0.14	0.8195	0.4014
L/L_o	1.06 ± 0.01	1.12 ± 0.03	1.34 ± 0.03	<0.001	0.0119
$[Hb]_{tot}$	19.6 ± 1.4 µM	13.7 ± 1.9 µM	9.9 ± 1.7 µM	0.0055	0.6606
SO_2	0.53 ± 0.05	0.76 ± 0.05	0.73 ± 0.06	0.0212	0.7555
%Collagen	6.6 ± 1.9	24.4 ± 3.4	47.9 ± 4.6	<0.001	0.0212
%NADH	69.0 ± 2.3	53.2 ± 3.7	44.7 ± 4.3	0.0011	0.2194
%FAD	24.4 ± 1.6	22.5 ± 2.4	7.4 ± 1.6	0.0091	0.0756

Variables from the PCA and PTI models were input into a hybrid tissue classification algorithm (Figures 2.18 and 2.19) to distinguish adenocarcinoma from pancreatitis and normal pancreatic tissue.

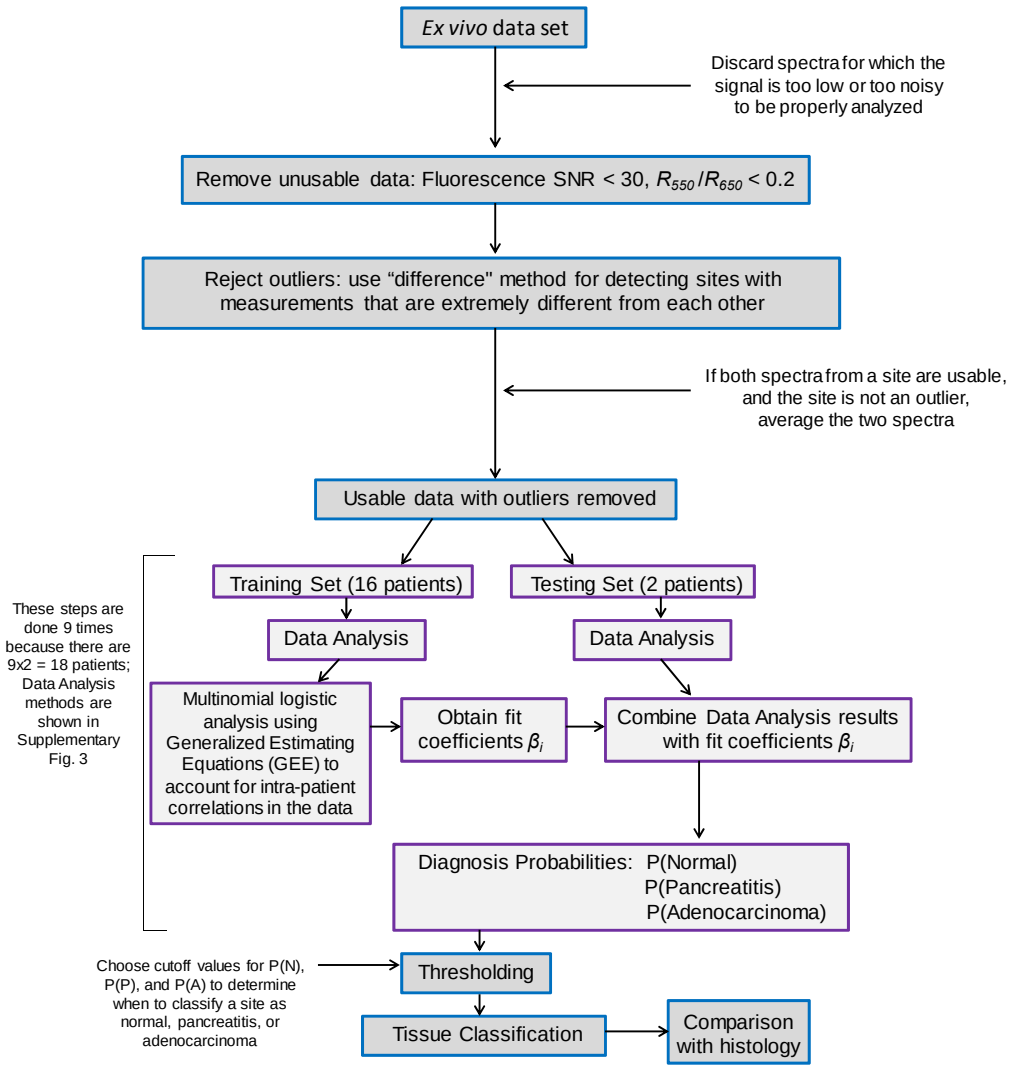

Figure 2.18 Flow chart of tissue classification algorithm. First, optical spectra are removed from the data set if the signal is too low or too noisy for analysis. Next, sites for which the two measured spectra are significantly different from each other are removed. Then, the resulting data set (39 normal sites, 34 pancreatitis sites, 32 adenocarcinoma sites) is split into a training set (16 patients) and a testing set (2 patients). The optical spectra from each training set are modeled with the PCA and PTI models to obtain diagnostically-relevant tissue parameters. These parameters are then input into a multinomial logistic regression that uses Generalized Estimating Equations (GEE) to account for the fact that multiple sites were measured from each patient. The multinomial logistic regression provides fit coefficients that are combined with the tissue parameters extracted from the testing set to obtain the diagnosis probabilities that each tissue site in the testing set is normal, pancreatitis, or adenocarcinoma. Thresholds are applied to these probabilities to determine the diagnosis for each site. These optical diagnostic results are then compared with those of histopathology. The process is repeated nine times, so that each patient is included in exactly one testing set. The boxes outlined in purple correspond to the portion of the algorithm shown in Figure 2.19.

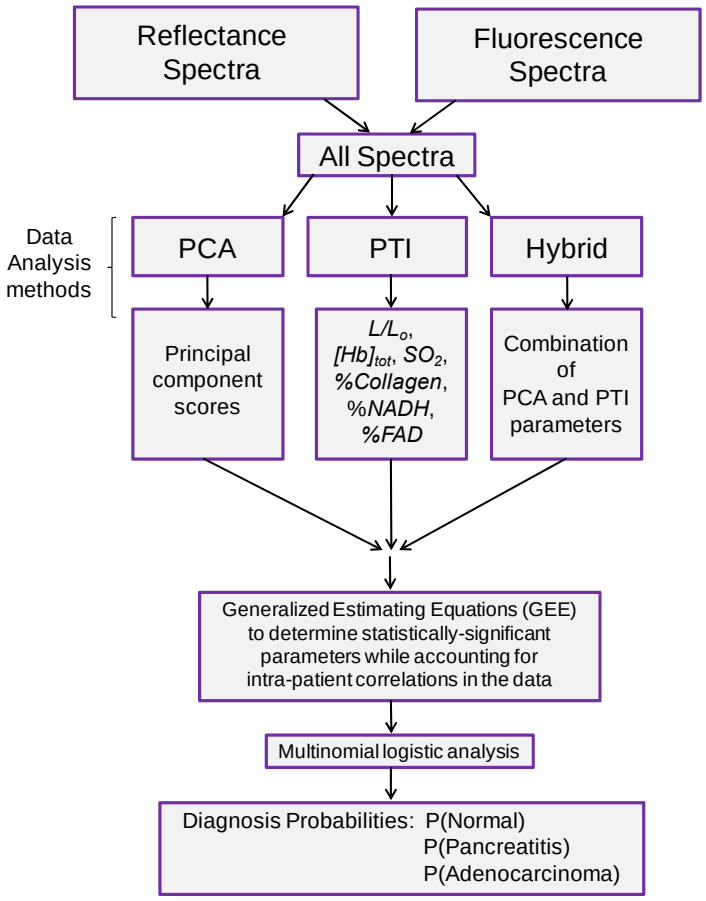

Figure 2.19 Flow chart of data analysis and tissue classification procedures employed to analyze optical spectra from human pancreatic tissues. First, the measured reflectance and fluorescence spectra are analyzed with principal component analysis (PCA) and a photon-tissue interaction (PTI) model to extract tissue parameters that describe disease-related changes in the spectra. Then, Generalized Estimating Equations (GEE), which corrects for intra-patient correlations in the data set, is employed to determine which parameters will be put into the multinomial logistic analysis tissue classification algorithm. The outputs of the multinomial logistic analysis algorithm are the diagnosis probabilities *P(N)*, *P(P)*, and *P(A)* that a given tissue site is normal, pancreatitis, or adenocarcinoma, respectively.

Selection of the variables used in the tissue classification algorithm was determined through multinomial logistic regression using Generalized Estimating Equations (GEE) [135-137] to statistically account for the fact that the data set included multiple sites from each patient and employed the complete data set. GEE has been previously employed in

medical physics studies to correct for intra-patient correlations [138-141]; for instance, in ophthalmology, in which there are correlations between data taken from the two eyes of a single patient [138].

For each variable extracted by the PCA and PTI models, a GEE model with an exchangeable correlation structure was employed to contrast the differences between the mean values of that variable for each pair of tissue types. For each contrast a Wald test statistic using the robust covariance matrix was calculated to account for the repeatedly measured observations from the same patients. Results from this analysis, including the *p*-values mentioned previously, can be found in Table 2.6.

Following the identification of significant predictor variables, correlations between the selected variables were calculated and highly correlated variables were removed to minimize the multicollinearity. The final set of variables that were used included the nuclear enlargement factor, percent collagen contribution, and total hemoglobin concentration from the PTI model algorithm, as well as the first three principal components of the reflectance and the third principal component of the fluorescence. The first two principal components of fluorescence were dropped due to their extreme correlation with other variables. The Pearson correlation between the first principal component of fluorescence and the percent collagen contribution was -0.92, and the Pearson correlation between the second principal component of fluorescence and the second principal component of reflectance was 0.76. The third fluorescence principal component *FPC3* was used in the classification algorithm despite its lack of statistical

significance because the cost associated with the multinomial logistic regression model was minimized when *FPC3* was included.

For tissue classification (Figure 2.18), a "leave-two-patients-out" cross-validation method was employed. The classification algorithm was run nine times, and each time, the data set was split into a training set of 16 patients and a testing set of two patients. The algorithm was executed nine times because there were 18 patients overall and each patient was put in the testing set exactly once. For each pair of training and test data sets a standard multinomial logistic regression was fit to the training dataset and was then employed to generate predicted probabilities of adenocarcinoma, pancreatitis, and normal tissue types for the observations in the test data set

The outputs of the classification algorithm were the diagnosis probabilities *P(N)*, *P(P)*, and *P(A)* of each site being normal, pancreatitis, or adenocarcinoma. Ternary plots of these probabilities for all sites in the data set are shown in Figure 2.20 for the hybrid algorithm (including PCA and PTI variables) and in Figure 2.21 for the algorithm using only PCA variables (Figure 2.21(a)) and the algorithm using only PTI variables (Figure 2.21(b)).

A threshold was then applied to *P(A)* to determine whether each individual site should be classified as "cancer" or "not cancer." The sensitivity and specificity calculated for different thresholds were employed to generate ROC curves (Figure 2.22) for distinguishing adenocarcinoma from non-cancerous tissue. The area under the ROC

curve was 0.906 for the hybrid algorithm, 0.881 for the algorithm using only PCA variables, and 0.847 for the algorithm using only PTI variables (Figure 2.22). In order to determine the sensitivity, specificity, positive predictive value (PPV), and negative predictive value (NPV) of the optical method for detecting pancreatic adenocarcinoma, the threshold for a diagnosis of cancer was set at $P(A) > 0.28$. The resulting sensitivity, specificity, PPV, and NPV were 87.5%, 89.0%, 77.8%, and 94.2% for distinguishing adenocarcinoma from non-cancerous tissue (Figure 2.20).

The aforementioned thresholding method was compared with a cost-function-based technique for calculating the optimal thresholds for determining a diagnosis of normal, pancreatitis, or adenocarcinoma from the predicted probabilities. In this technique, costs were assigned to each of the potential errors that could occur with prediction. Incorrectly predicting a site as either pancreatitis or normal tissue when it was actually adenocarcinoma was considered the worst possible error and assigned a high cost of 12. Predicting cancer for either normal or pancreatitis sites resulted in a cost of 6. Finally, incorrectly predicting pancreatitis as normal or vice versa was assigned a cost of 1. The optimal thresholds were those that minimized the total cost for the given model and were found through a grid search. The cost-based thresholding method distinguished adenocarcinoma from non-cancerous tissue with the same sensitivity, specificity, PPV, and NPV as the thresholding method in which sites with $P(A) > 0.28$ were diagnosed as cancer (87.5%, 89.0%, 77.8%, and 94.2%, respectively).

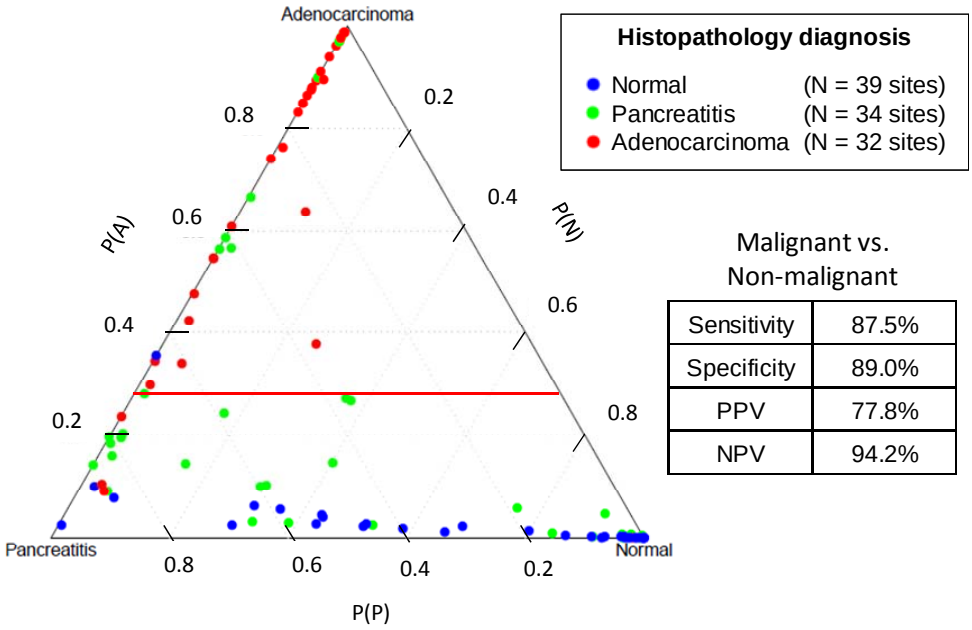

Figure 2.20 Ternary plot of diagnosis probabilities (probability *P(N)* that a tissue site is normal; probability *P(P)* that the site is pancreatitis; probability *P(A)* that the site is adenocarcinoma), as determined by optical spectroscopy with the hybrid data analysis method (which included parameters from both the PCA and the PTI models). Shown alongside the ternary plot are the sensitivity, specificity, positive predictive value (PPV), and negative predictive value (NPV) for distinguishing malignant (adenocarcinoma) tissue sites from non-malignant (normal and pancreatitis) tissue sites. Parameters from reflectance (first three principal component scores, nuclear enlargement factor L/L_o, and total hemoglobin concentration $[Hb]_{tot}$) and fluorescence (third principal component score and percentage contribution of collagen) were used in the hybrid method, and only one threshold ($P(A) > 0.28$; red line) was required to achieve the user-defined optimal classification accuracy.

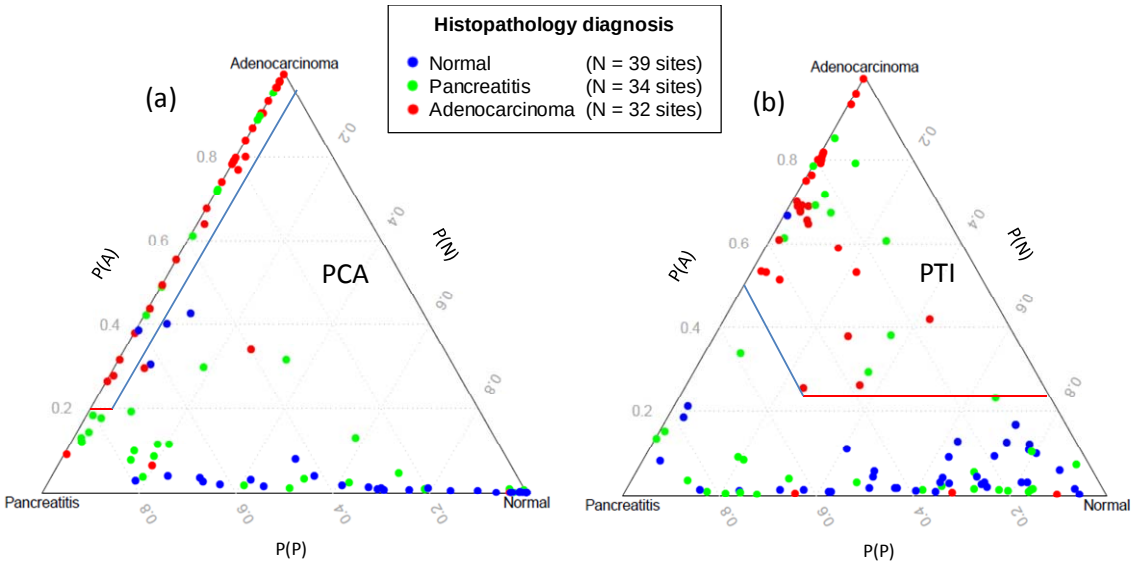

Malignant vs. Non-malignant

Sensitivity	84.4%
Specificity	86.3%
PPV	73.0%
NPV	92.6%

Malignant vs. Non-malignant

Sensitivity	90.6%
Specificity	84.9%
PPV	72.5%
NPV	95.4%

Figure 2.21 Ternary plots of diagnosis probabilities (probability *P(N)* that a site is normal; probability *P(P)* that the site is pancreatitis; probability *P(A)* that the site is adenocarcinoma), as determined by optical spectroscopy with the PCA (a) and PTI (b) models. The tissue sites are color-coded according to histopathological diagnosis. Optimal probability thresholds for distinguishing malignant tissue sites (adenocarcinoma) from non-malignant tissue sites (normal and pancreatitis) are shown in both (a) and (b). Red lines indicate thresholds on *P(A)*, and blue lines denote thresholds on either *P(N)* (a) or *P(P)* (b). The sensitivity, specificity, positive predictive value (PPV), and negative predictive value (NPV) for distinguishing adenocarcinoma are shown beneath the plots. Both models distinguished malignant from non-malignant tissues with a sensitivity and specificity of greater than 84%, and a NPV of over 92%.

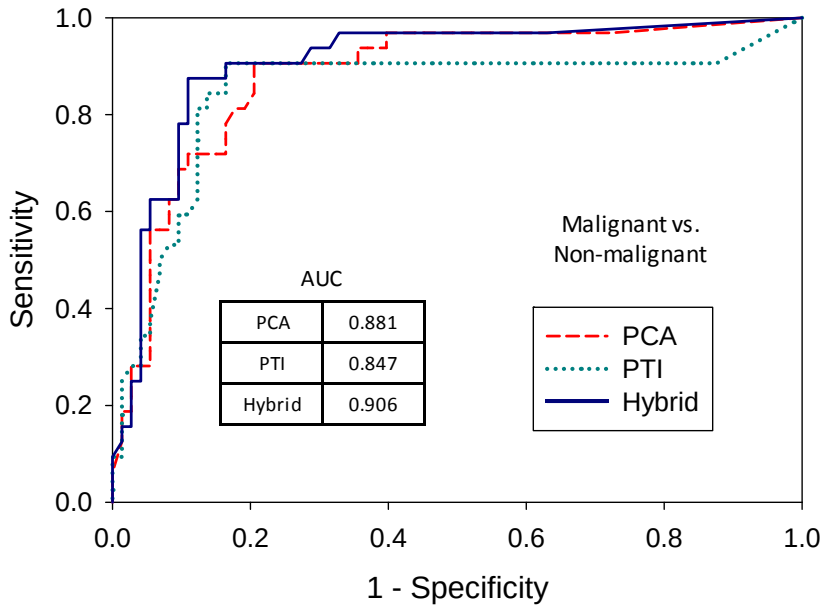

Figure 2.22 Receiver operating characteristic (ROC) curves for distinguishing malignant (adenocarcinoma) tissue sites from non-malignant (normal and pancreatitis) tissue sites using the PCA model, the PTI model, and the hybrid method combining PCA and PTI parameters, with the area under the curve (AUC) for each method displayed as an inset. The ROC curves were generated by applying a set of different thresholds to the predictive probability of adenocarcinoma. Overall, the hybrid method provided the best diagnostic accuracy for detecting adenocarcinoma, as evidenced by the fact that the hybrid had the highest AUC.

The optical spectroscopy-based classification method has several potential advantages over currently employed methods to detect pancreatic cancer. The method is potentially compatible with minimally invasive endoscopic procedures, including endoscopic ultrasound-guided fine-needle aspiration (EUS-FNA), which currently suffers from limited diagnostic accuracy. The method also provides real-time feedback, does not require exogenous contrast, is cost-effective, and can potentially be employed for diagnosis of other tissue types, such as pre-cancers and pancreatitis. These results suggest that the optical spectroscopy method described in this dissertation has the potential to assist with detection of pancreatic cancer in a clinical setting.

Chapter 3

Bone and breast tissue characterization with Raman spectroscopy

3.1. Monte Carlo modeling of Raman scattering in bone tissue

Elastic light-scattering spectroscopy is frequently used in biomedical optics to provide information about the morphological and biochemical composition of tissues [5, 6, 9, 57, 59, 92, 142, 143]. The resulting data has been incorporated into sophisticated tissue diagnostic methods for early disease detection and other types of tissue viability assessment throughout the body: for instance, in the breast [9, 92], colon [5], cervix [59], esophagus [6], and oral mucosa [57, 142, 143]. Recently, there has been interest in developing such an algorithm for early detection of osteoporosis, a condition that causes bone strength to decrease over time and ultimately leads to fracture in about 35% of women over 50 as well as 1 in every 8 men [144]. Osteoporosis is often difficult to diagnose until the first fracture occurs, and current screening methods rely heavily on bone density measurements that fail to provide much information about the bone's molecular composition [145].

Raman spectroscopy can potentially be used to develop a noninvasive screening method that can detect the biochemical changes associated with the progression of osteoporosis and other bone diseases, because it provides biochemical information about bone

composition [146]. For bone tissue, information about both the mineral and matrix components can be obtained. Bone mineral is similar to hydroxyapatite, $Ca_{10}(PO_4)_6(OH)_2$, but with extensive carbonate substitution into the apatitic lattice, as well as substitution of other ions, especially sodium and magnesium [146]. The mineral is embedded within the matrix, which is about 90% type I collagen. Both the phosphate (~960 cm^{-1}) and carbonate (~1070 cm^{-1}) symmetric stretches are prominent mineral bands in bone spectra. The amide III (~1250 cm^{-1}), CH_2 scissoring (~1450 cm^{-1}), and amide I (~1650 cm^{-1}) regions are representative of the collagen matrix [146-148].

One Raman metric that is often used to characterize the quality of bone tissue is the carbonate/phosphate (C/P) ratio, given by the height or area ratio of the carbonate and phosphate symmetric stretching bands [147]. This ratio is a measure of the amount of carbonate substitution in the apatitic lattice and has been shown to correlate with bone stiffness [146]. Raman spectroscopy of tissue is performed with near-infrared lasers, usually with wavelengths of 785 nm or 830 nm. Near-infrared light has a high tissue penetration depth (on the order of centimeters) and is essentially harmless to humans, thereby allowing bone measurements to be made through overlying tissues via a fiber-optic probe placed directly on the skin [39]. Recently, a fiber-optic probe was even used to collect Raman data from a canine tibia, and combined with spatial priors from a CT scan, a tomographic image of a portion of the limb was reconstructed [148]. Therefore, Raman spectroscopy using fiber-optic probes is of great potential use for the noninvasive and information-rich measurements of bone tissue quality.

However, there are also several major challenges associated with using Raman spectroscopy as a tissue diagnostic modality. For one, detected Raman signal is usually several orders of magnitude lower than fluorescence, so it is important to design the fiber-optic probe in a manner that optimizes the collection of Raman signal [149]. Also, if the probe is going to send light into the tissue through the skin, there are multiple layers of tissue between the skin and the bone, and each of these layers has its own set of absorption and elastic scattering properties that can attenuate the detected bone Raman signal [149]. Therefore, it is crucial to develop a mathematical model of Raman scattering that is able to pinpoint the optimal source-detector configuration for maximizing the ratio of bone Raman signal to background, as well as correct the detected Raman signal for artifacts related to tissue absorption and elastic scattering. Monte Carlo simulations are known to be effective at accomplishing both of these objectives for reflectance and fluorescence studies throughout optical parameter space and for a variety of fiber-probe configurations [75-77, 150]. Recently, Monte Carlo and other mathematical models of Raman scattering [151-153] have been applied to several types of turbid media, including biological tissue, but to our knowledge, these codes have not incorporated a multi-layered geometry overlying bone tissue. This study [154] shows preliminary results of a Monte Carlo model of Raman scattering in bone that is buried within a tri-layered soft tissue structure consisting of dermis, subdermis, and muscle. The code is utilized to locate an optimal source-detector separation for maximum detected bone Raman signal, as well as to demonstrate how the carbonate/phosphate ratio can be distorted by elastic scattering effects from the overlying tissue layers.

As mentioned previously, the tissue model used in this study included overlying layers of dermis, subdermis, and muscle, but this preliminary version neglected intermediate layers such as fascia, tendon, and periosteum. In order to determine whether these layers would have a significant effect on the detected Raman signal, an experiment was performed in which a number of these layers were dissected from a rat leg, and their optical properties were measured with an integrating sphere. A digital photograph of some of these tissue layers is shown in Figure 3.1 to demonstrate the amount of variability between the size, geometry, and blood content of the various tissues.

Using a 6" diameter integrating sphere (Labsphere, RT-060-SF) with Spectraflect coating (reflectivity ~ 0.96) on the inside wall, reflectance and transmittance measurements were taken from a variety of tissue types in a dissected rat leg. The measurements used a broadband light source from a lamp that was sent directly into a Kohler illuminator (Labsphere, KI-120) to collimate the light. The light source was powered by an LPS preset power supply (Labsphere, LPS-150-0660). The lamp emitted primarily in the visible range, but it will most likely be replaced with an IR source in future studies so that the interrogated spectral region will match up with that used in the experimental Raman spectral measurements. For reflectance measurements, the light beam was sent through an open port on one side of the sphere, and it propagated through the sphere until it reached the sample port on the other side. Some of the light was then diffusely reflected by the tissue sample and this light re-entered the sphere, where it bounced off of the sphere walls until it was angled in such a way that it reached the detector port and traveled out of the sphere, through a fiber optic cable, and into a spectrometer (HR2000+,

Ocean Optics, 200-1100 nm range) that was linked to a computer via a USB port. The data was then displayed on-screen and saved using the Ocean Optics SpectraSuite software. For transmittance measurements, a similar procedure was used, except that the sample was moved to the side of the sphere nearest the light source, and the port on the opposite side was covered.

When performing integrating sphere measurements of biological tissue, it is important that the measured sample is relatively homogeneous and has a diameter greater than the diameter of the light beam [155]. These two stipulations were often difficult to follow for rat tissues of the types shown in Figure 3.1 because of their small size and tendency to self-adhere in irregular ways (e.g. fascia in Figure 3.1). For several tissue types, such as periosteum, tendon, and bone, the diameter of the sample was essentially equal to the diameter of the incident light beam; future experiments will attempt to address this issue in order to minimize light losses. The sample diameter should also be greater than the sample port diameter, in order to prevent light losses from the uncovered portion of the sample port; this precaution was neglected in the initial experiment, but port reducers (Labsphere, Spectraflect coating, 1.0” to 0.25” and 1.0” to 0.125”) have been purchased and can be employed to make the reflectance and transmittance measurements more accurate.

In order to account for the spectral response of the lamp, the reflectance and transmittance were measured with respect to standards. For reflectance, a Spectralon® reflectance standard (Labsphere, SRS-99-010, 99% reflectance, 1.25” diameter) was

placed in the sample port, and for transmittance, the sample port was left empty. In order to measure the background signal, dark spectra were also taken. The diffuse reflectance and transmittance spectra were then obtained by the formulae $R(\lambda) = r_{std}\ (R_{meas}(\lambda)-R_{dark}(\lambda))/(R_{std}(\lambda)-R_{dark}(\lambda))$ and $T(\lambda) = (T_{meas}(\lambda)-T_{dark}(\lambda))/(T_0(\lambda)-T_{dark}(\lambda))$, where $R_{meas}(\lambda)$ and $T_{meas}(\lambda)$ were the uncorrected reflectance and transmittance of the sample, $R_{std}(\lambda)$ was the measured reflectance spectrum of the Spectralon® standard, r_{std} was the reflectance of the standard (equal to 0.99) and $T_0(\lambda)$ was the measured transmittance spectrum with an empty sample port [156]. If the reduced elastic scattering coefficient is to be separated into the elastic scattering coefficient $\mu_s(\lambda)$ and the anisotropy $g(\lambda)$, a collimated transmittance measurement must also be performed [155, 157].

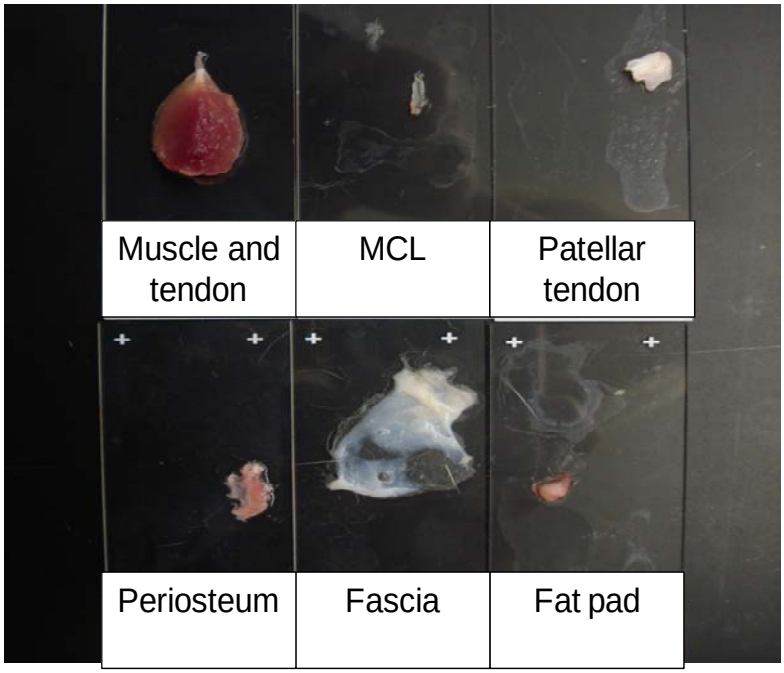

Figure 3.1 Various types of tissue dissected from the leg of a rat [154], demonstrating a high degree of variation in the geometrical and optical properties.

The MC model used in this study has been described previously [76, 77]. Briefly, photons are launched into a layered tissue model approximated by a stack of turbid slabs with various thicknesses, absorption and elastic scattering coefficients, and anisotropies [150]. Each elastic scattering event is modeled by sampling the step size and scattering angle from probability distribution functions [150]. The Henyey-Greenstein function is used to model the distribution of scattering angles in a manner that incorporates the anisotropy of the tissue [150]. Photons are given an initial weight of unity, and this weight is subsequently attenuated according to Beer's Law at each scattering step [76]. If the weight of a photon falls below a pre-defined threshold, the photon is sent to a Russian roulette routine and if it does not survive, it is said to be absorbed by the tissue [76]. The MC code has previously been modified to accommodate absorption and re-emission from multiple fluorophores with distinct quantum yields, mean lifetimes, and locations in any of the tissue layers [77]. Previous studies had validated the code against experimental phantom studies and theoretical photon transport expressions [76, 77].

To model Raman scattering within the framework of the MC code, a Raman event was treated as a fluorescence event with a mean lifetime of zero, which was believed to be a good approximation because Raman scattering takes several orders of magnitude less time than fluorescence. Another approximation in the preliminary version of the code was that Raman scattering was isotropic; it will be necessary to perform subsequent research to determine if this assumption needs to be modified. The bone tissue was modeled as having two Raman scatterers, carbonate and phosphate, and Raman scattering from all other tissue layers was neglected. The relative concentrations and Raman cross

sections of the carbonate and phosphate were modeled with the pre-existing variables for the fluorophore absorption coefficient and fluorescence quantum yield. Since the preliminary study was focused on simulating carbonate/phosphate ratios, it was not necessary to input the correct magnitudes of the concentrations and cross-sections as long as their ratio was consistent with literature [147, 158]. A schematic of the tissue model used for the MC simulations (Figure 3.2) included overlying layers of dermis, subdermis, and muscle atop the bone; values for the absorption coefficients, elastic scattering coefficients, and thicknesses of these layers were estimated from literature [147, 159]. The anisotropy and refractive index for all layers and wavelengths were set to 0.9 and 1.4, respectively [77, 160]. The combined thickness of all tissue layers atop the bone [147] was held constant at 2 mm. Studies to measure the absorption and elastic scattering coefficients of several other intermediate tissue layers (fascia, tendon, and periosteum) and incorporate these layers into the tissue model are currently underway. The fiber-optic probe used in the MC code was similar to the "ring-disk" configuration published in previous literature [147]. All of the fibers were modeled to have diameters of 200 μm and numerical apertures equal to 0.22. Table 3.1 provides the tissue absorption and elastic scattering coefficients [159] used for each layer of the model. The elastic scattering coefficients in each tissue layer at 857 nm were set equal to those at 849 nm in the first set of simulations, and then reduced by 5 cm^{-1} for the next set of simulations.

Table 3.1 Tissue properties used in Raman scattering simulations [154].

Wavelength	**785 nm (excitation)**		**849 nm (Raman scattering from phosphate)**		**857 nm (Raman scattering from carbonate)**	
Optical coefficient	μ_a **(cm^{-1})**	μ_s **(cm^{-1})**	μ_a **(cm^{-1})**	μ_s **(cm^{-1})**	μ_a **(cm^{-1})**	μ_s **(cm^{-1})**
Dermis	0.15	200	0.125	185	0.125	185, 180
Subdermis	0.08	125	0.08	115	0.08	115, 110
Muscle	0.4	70	0.4	65	0.4	65, 60
Bone	0.07	140	0.08	135	0.08	135, 130

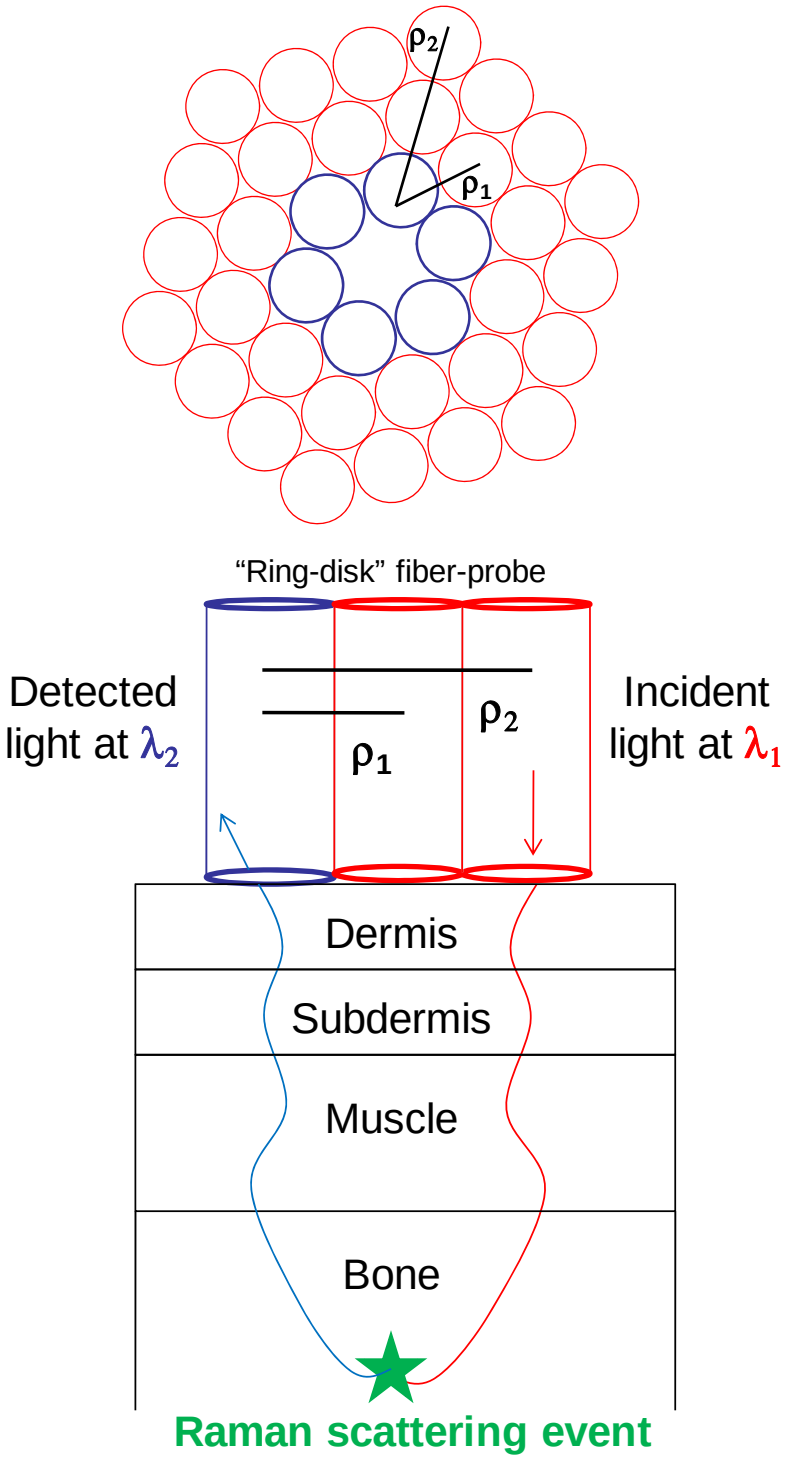

Figure 3.2 Schematic of four-layered tissue model and ring-disk probe configuration used in Raman MC simulations [154].

The MC code was utilized with the tissue model shown in Figure 3.2 in order to predict the source-detector separation that would produce the highest number of detected Raman photons (Figure 3.3). In these simulations, the elastic scattering coefficients in each tissue layer at 857 nm were set equal to those at 849 nm.

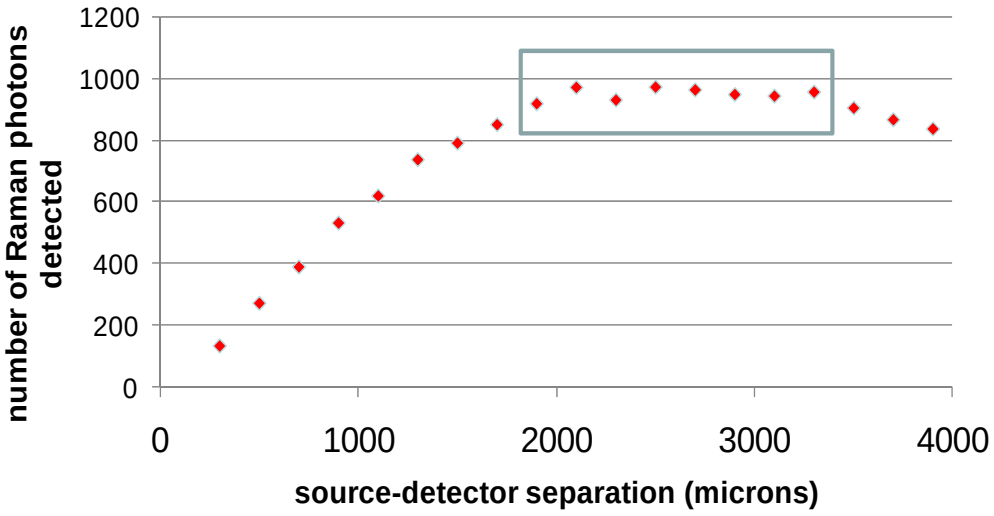

Figure 3.3 Plot of number of detected Raman photons as a function of source-detector separation [154], for the tissue model shown in Figure 3.2. The boxed region (centered at a separation distance of about 2.5 mm) represents the optimal predicted source-detector distance for detecting a maximum number of Raman photons from the tissue model.

Figure 3.3 predicts that a source-detector separation of around 2.5 mm will obtain the highest Raman photon counts. However, the current MC model neglects background from fluorescence, so further studies must be done to determine the optimal source-detector distance for obtaining a high ratio of Raman signal to fluorescence background.

The MC model of Raman scattering from bone was also used to predict how the calculated carbonate/phosphate (C/P) ratio might is affected by the thicknesses of the overlying tissue layers. First, a tissue model of exposed bone was used in a "control" MC simulation. The code was run four times, the results were averaged, and the mean C/P

ratio was determined. Next, the code was re-run for the four-layered tissue model shown in Figure 3.2; however, the absorption and elastic scattering coefficients of each layer were approximated to be the same for the Raman scattering wavelengths of carbonate (857 nm) and phosphate (849 nm). In this case, it was observed that there was more variation in the detected C/P ratios, so the code was run eight times in order to attempt to improve the statistics. The result was a mean C/P ratio that was almost identical to the one simulated with the exposed bone model; however, the standard deviation was larger. This result may be of importance when attempting to mathematically model the experimental results because a greater noise in the system limits the smallest detectable changes in the C/P ratio. It is potentially useful to obtain a quantitative description of how the standard deviation of the C/P ratio varies as a function of various changes to the tissue model.

For the next set of simulations, each layer of the tissue model was changed so that its elastic scattering coefficient at the Raman scattering wavelength of carbonate was 5 cm^{-1} less than that for the Raman scattering wavelength of phosphate (as shown in Table 3.1). It was hypothesized that this discrepancy in the elastic scattering coefficients would affect the mean calculated C/P ratio, because the photons that were Raman-scattered from carbonate would propagate differently than the photons that were Raman-scattered from phosphate. The absorption coefficient was assumed to be negligible in this region of the spectrum. A set of eight identical simulations was run for tissue models of various thicknesses in the different layers, in an attempt to estimate variations that might be found from region to region of the biological tissue being measured. The results of this

study are shown in Figure 3.4, where the thickness of the dermal and subdermal layers were each defined to be half of the total "skin" thickness, and the bone layer was regarded as semi-infinite.

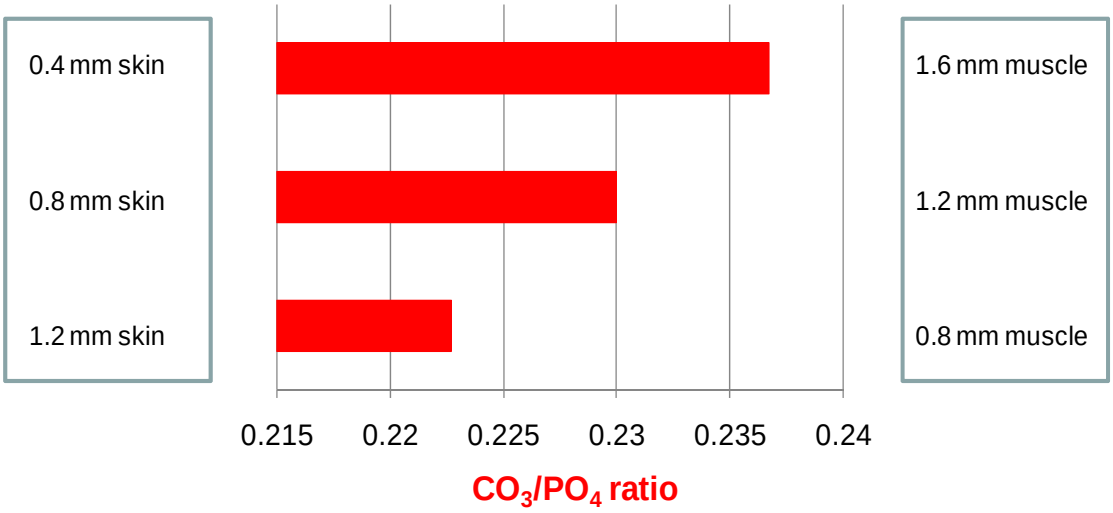

Figure 3.4 Change in carbonate/phosphate ratio for Raman tissue model with various thicknesses of skin and muscle [154], where the elastic scattering coefficients at the Raman scattering wavelengths of carbonate and phosphate were separated by 5 cm^{-1}.

The data shown in Figures 3.3 and 3.4 demonstrates that the MC model of Raman scattering has the potential to provide useful information about optimal source-detector separation for the fiber-optic probe, as well as a quantitative description of the effects of tissue thickness and elastic light scattering properties on the calculated carbonate/phosphate ratio. Work has also been done to generalize the photon detection scheme in the MC model, so that a high-resolution spatial map of photon exit coordinates can be generated from each simulation. This revision will allow for the testing of a wider range of potential probe configurations, and such a procedure is likely to be important for optimizing the detected ratio of bone Raman signal to background fluorescence. Studies

are also underway to characterize the optical properties of all tissue layers (including fascia, tendon, and periosteum) that Raman-scattered photons are likely to enter on their way back to the detector from the bone layer. The optical coefficients extracted from the integrating sphere measurements can be incorporated into a more detailed version of the MC model described here, and systematic studies can be conducted to determine which tissue layers have a significant effect on the detected bone Raman signal and which of these layers can be disregarded. Work is also currently in progress to convert the MC code to MATLAB as part of a revised algorithm that will be able to define tissue interfaces as mesh surfaces via externally-obtained data from modalities such as CT scans. These and other additions to the MC code will likely provide an even more realistic description of how the paths of Raman-scattered photons can be altered by the properties of the bone and the overlying tissue layers.

3.2. Monte Carlo modeling of Raman scattering in breast tissue

Spatially offset Raman spectroscopy (SORS) has been shown to be an effective tool in recovering Raman spectra from up to several millimeters beneath the surface of turbid media [39, 147, 149, 161-168]. The enhanced depth information obtained from SORS, compared to standard Raman techniques, results from photons being multiply scattered and traveling further beneath the surface before exiting the medium at larger source-detector (S-D) offsets. After initial demonstrations on layered chemical samples [162-164], this technique has been applied to several biological systems. The most extensive biomedical work has been the detection of Raman spectra from bone under several millimeters of soft tissue [147, 149, 166-168]. Other work has been aimed at finding calcifications in breast tissues [161, 167].

In both of the above biological applications, the detection target is hard tissue with strong Raman bands not present in soft tissue – e.g. the phosphate stretch at ~960 cm^{-1}. Detecting the presence of one type of soft tissue below a different layer of soft tissue is more challenging because the Raman spectra of the two layers will typically be quite similar and therefore hard to distinguish; discrimination relies on more subtle differences such as peak widths and relative ratios. This situation is demonstrated in Figure 3.5, which shows typical spectra obtained in a previous study at Vanderbilt, in which we demonstrated the ability of SORS to detect breast cancer tissue under up to 2 millimeters of normal breast tissue [165]. Using a classical least squares (CLS) model with the layers' pure component spectra as inputs, spectra were taken at various S-D offsets from a layered tissue construct to determine the relative spectral contributions of the two

layers. While this study effectively showed the feasibility of using SORS on layered soft tissues, it also raised questions about the limits of such an approach, particularly for evaluating margin status following breast conserving surgery (BCS) - the clinical motivation for this work.

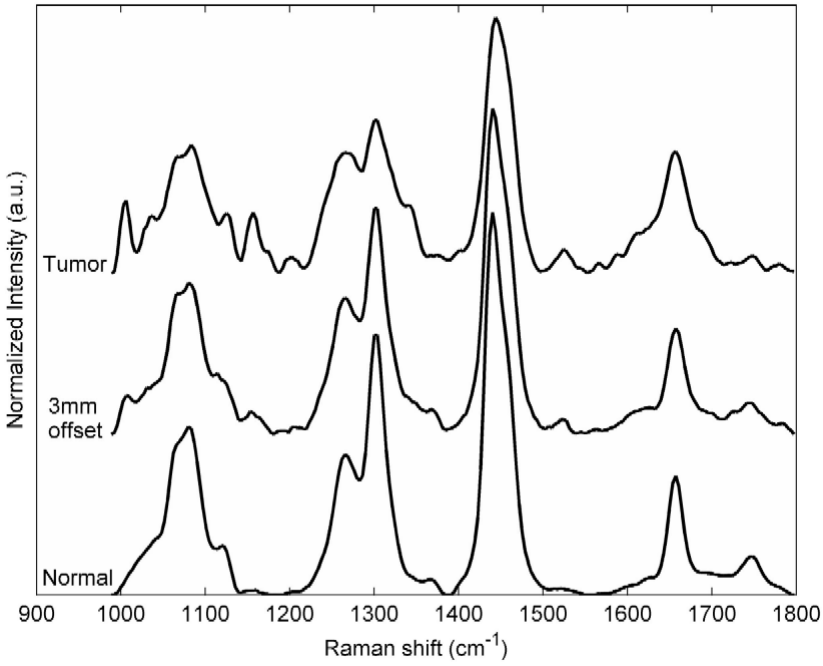

Figure 3.5 Typical Raman spectra from previous SORS study [165, 169] (used with permission), offset for clarity. Normal and tumor spectra are from homogeneous tissue sections, and the "3mm" spectrum is from the setup shown in Figure 3.6 with a S-D separation of 3 mm and a top normal layer of 0.5 mm.

Approximately 180,000 new breast cancer patients each year are eligible for BCS [170], in which the primary tumor is removed along with a surrounding margin of at least 1-2 mm of normal tissue. When the normal tissue margin is of insufficient size (i.e. the margin is "positive"), the patient's risk of recurrence significantly increases, and a second operation becomes necessary [171, 172]. The exact definition of a positive margin varies

by institution [173]; reports show the lowest recurrence rates when a negative margin of 2 mm or more is required, and this value is becoming more widely used [171]. Since current methods of intraoperative margin analysis are limited in terms of accuracy and/or time required [174-177], using SORS for this application could fill a major medical need. From the earlier feasibility study [165], it appears that SORS has the potential to address this need; however, a major issue to be addressed is the detection limit of this technique, in terms of the size of both the overlying normal layer and the tumor.

Since it is very difficult and largely impractical to precisely control tissue thicknesses and geometries in intact specimens, a Monte Carlo (MC) simulation model was sought to investigate the issue of detection limits. Modeling using MC methods has long been considered the gold standard for predicting photon propagation in turbid media. Numerous MC codes have been developed to simulate diffuse reflectance and fluorescence from layered biological tissues [37, 75, 77], but little work has been done in this area with respect to Raman scattering. Matousek *et al.* previously developed a Raman MC model for layered turbid media [152], but their work was largely focused on chemical powders and thus made many simplifying assumptions. Schulmerich *et al.* recently reported on a Raman tomography algorithm for imaging of canine bone tissue using a finite-element reconstruction method [148]. Enejder *et al.* developed a Raman MC model for predicting the effect of system geometry on detected Raman signal from blood [178]. Shih *et al.* used a Raman MC code to validate a photon migration technique for correcting detected Raman spectra for tissue scattering and absorption artifacts [153].

However, none of these previous studies has employed a MC code to model Raman scattering in a layered turbid biological medium using a SORS approach.

The first goal of this study [169] was therefore to adapt the multi-layer fluorescence Monte Carlo code of Vishwanath and Mycek [37, 77] to model Raman scattering in breast tissue, as reported previously for modeling Raman scattering in bone tissues [154]. The model, which recorded the spatial origins of all detected Raman photons in the simulations, was validated by comparing its predicted relative tumor contributions to experimental results [165]. The validated MC model was then used to gain insight on practical considerations, such as detection limits and relevant source-detector separations, for using SORS to evaluate margins in BCS. To do so, models were created to examine relative spectral contributions from each layer in constructs with normal human breast tissue overlaid on breast tumor tissue. A variety of factors were altered in these constructs, including the presence of quartz coverslips present in the tissue constructs used in the original experimental data, thicknesses of both the normal and tumor layers, and the presence of an additional normal layer underneath the tumor.

The Raman Monte Carlo model employed in this report was developed by modifying the previously-existing multi-layer, multi-fluorophore Monte Carlo code of Vishwanath and Mycek [37, 77]. In the fluorescence code, all photons are launched into the medium in accordance with the radius and numerical aperture of the source fiber, with an initial weight equal to 1; a given photon is then scattered through the medium until it exits the tissue or its weight falls below some pre-defined threshold due to absorption. The length

of each scattering step of a photon in layer i of the tissue is determined from sampling a probability distribution dependent on the tissue scattering coefficient μ_{si} in the i^{th} tissue layer. At each step of the photon's path, a new scattering angle is calculated by sampling the Henyey-Greenstein phase function based on the layer's scattering anisotropy g. At any point on its path, a photon can be absorbed by a fluorophore; the probability of this effect is determined by sampling a probability distribution function that is dependent on the fluorophore absorption coefficient μ_{afxi} in the i^{th} tissue layer. Photons that have been absorbed by a fluorophore in layer i of the tissue will then be re-emitted at the emission wavelength, after some time delay τ_i, determined by sampling a probability distribution for the mean time spent by the fluorophore in the excited state. The efficiency of the re-emission of fluorescence photons is determined by the fluorophore quantum yield ϕ_{QYi} in layer i. When a photon exits the tissue, it is "detected" if the radial distance between its entry and exit positions is within one of the pre-defined "detector" bins and its angle of exit is within the acceptance cone defined by the numerical aperture of the detector fibers.

In order to accommodate Raman scattering, the fluorophore absorption coefficient μ_{afxi} and fluorescence quantum yield ϕ_{QYi} in tissue layer i were treated as a single quantity R_{xi} indicative of the Raman cross section (i.e. how likely it is that an excitation photon will undergo Raman scattering) in the i^{th} layer [154]. Once a photon was Raman scattered, any subsequent Raman scattering of that photon was neglected since the probability of Raman scattering is very low compared to elastic scattering or even fluorescence [179]. In addition, the mean time delay τ_i between fluorescence excitation and emission was set

to zero to indicate that Raman scattering could be approximated as instantaneous [179]. Each Raman scattering event was approximated as an isotropic process. While other Raman Monte Carlo reports [152, 153, 178, 180] use this assumption as well, we could not find any experimental validation of this property for biological tissues. To that end, goniometric-like measurements were performed initially on a cylindrical cuvette of cyclohexane in the style of Passos *et al.* [181], and subsequently on a 100 μm thick layer of chicken fat based on Arnfield *et al.* [182]; in both cases, Raman signal was detected rather than elastic scattering as in the references. These experiments (results not shown) provided evidence in support of the assumption that Raman scattering in tissue is an isotropic process.

The wavelength associated with the Raman scattered photons was chosen to be 884 nm. This wavelength falls almost exactly in the middle of the wavelength range corresponding to the relative wavenumber range used experimentally of 990 cm^{-1} (~851 nm) to 1800 cm^{-1} (~914 nm). Optical properties for normal and malignant breast tissues are also available for this wavelength in the literature [183]. It was reasonable to use only a single Raman wavelength because in the near infrared region, absorption in biological tissues is close to zero and tissue scattering is nearly constant [183-185].

The modified Monte Carlo code also included sections that accounted for the presence of clear layers (e.g. glass or quartz coverslips or slides) that had no absorption or scattering but did have a different refractive index than the surrounding tissue layers. This modification was important since the experimental studies [165] included quartz

coverslips between the tissue layers. To simulate the zero-scattering nature of the coverslips, the code was modified to immediately move any photon that had just entered a clear layer to the opposite edge of that layer. Therefore, the next step of any photon that had entered a clear layer would take that photon across the boundary of the clear layer, unless the photon was reflected at the boundary. In that case, the reflected photon would be immediately transported to the opposite edge of the clear layer once again, and the aforementioned process would be repeated. In addition, since the experimental tissue constructs had coverslips on top of the upper tissue layer [165], the code was modified so that all photons began at the bottom edge of this first coverslip, to simulate the effect of the coverslip having no significant scattering properties.

The values used for the relevant optical properties in the MC model are shown in Table 3.2. For the simulations presented in this manuscript, specific values for the reduced scattering coefficient ($\mu_s' = \mu_s[1-g]$) and absorption coefficient for both excitation photons at 785 nm and Raman photons at 884 nm were taken from a study by Grosenick *et al.* [183]. These values were also confirmed experimentally in-house at 785 nm for a small sample set using a double integrating sphere and the inverse adding-doubling method [157]. Anisotropy values for elastic scattering were held constant at both wavelengths and were taken from a report by Ghosh *et al.* [41]. Relative Raman cross sections were estimated by comparing the total area under the curve from non-normalized Raman spectra of optically thick samples of normal breast and breast cancer tissues obtained in identical fashions. The samples were acquired from the Cooperative Human Tissue Network; they were fresh-frozen and were thawed in buffered saline at room

temperature prior to measurement [165]. The values of "4" and "1" for R_{xi} in Table 3.2 indicate that the total signal from normal breast tissues was four times higher than from tumor tissues.

Table 3.2 Summary of optical properties for normal and tumor tissues at excitation (785 nm) and Raman (884 nm) wavelengths [41, 183]. These properties include the absorption coefficient (μ_a), reduced scattering coefficient (μ_s'), anisotropy (g), and relative Raman cross-section (R_x) [169].

Parameter	Normal @785 nm	Tumor @785 nm	Normal @884 nm	Tumor @884 nm
μ_a (cm^{-1})	0.04	0.10	0.06	0.12
μ_s' (cm^{-1})	9.5	11.6	8.0	9.1
g	0.88	0.96	0.88	0.96
R_x	4	1	N/A	N/A

Simulations whose results are shown in Figures 3.7 through 3.10 were run with 10^8 initial photons, and other simulations were run with 5 x 10^7 initial photons. The excitation region and detector bins were set up to match the size (200 μm diameter), placement, and numerical aperture (0.22) of the optical fibers used in the experimental data. Results were quantified by determining the fraction of detected Raman photons in each bin that originated in the tumor layer. This measure was equivalent to the "relative tumor contribution" metric derived from experimental data, which used chemometrics to indicate the % contribution of the pure tumor layer spectrum to a measured spectrum at a given S-D offset [165]. Unless otherwise specified, the thickness of the tumor layer was set to 5 mm to correspond to the approximate thicknesses of the experimental samples.

For simulations with an additional normal layer under the tumor, the thickness of this bottom normal layer was set to 2 cm to act as an optically thick layer.

Figure 3.6 shows the experimental setup used to obtain tissue SORS spectra with examples of paths photons can take from the source fiber to detector fiber at various spatial offsets. A 200 μm source fiber delivered 80 mW of 785 nm light from a diode laser to the sample. This fiber was fixed in position for a given measurement site, and SORS spectra were acquired by translating a 200 μm detector fiber to S-D offsets of 0.75 to 4.75 mm in 0.5 mm increments. Spectra were recorded using an imaging spectrograph and NIR-optimized CCD detector (details described in [165]). The tissue constructs consisted of a bottom layer of ~5 mm thick and 10 by 10 mm wide human breast tumors, with overlying 0.5, 1, and 2 mm thick, and slightly wider normal human breast tissue layers, each encompassed by quartz coverslips and appropriate spacers to accurately control the thickness.

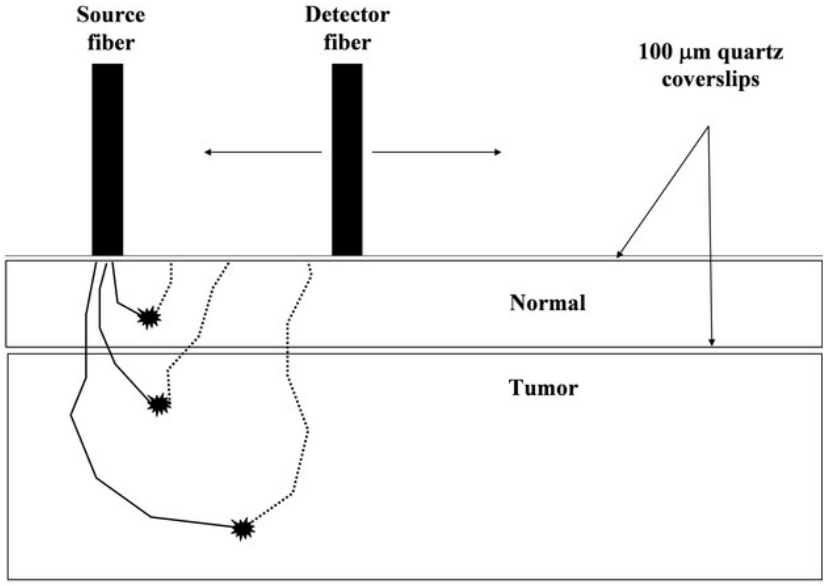

Figure 3.6 Experimental setup from previous report [165, 169] (used with permission) along with sample Monte Carlo photon paths. Solid lines represent excitation photons, dotted lines represent Raman scattered photons. Raman scattering events are represented by symbols at junctions of lines.

Some of the initial Monte Carlo results are shown in Figure 3.7. Each marker in the plot represents the spatial location where a detected Raman photon was generated. One can see that the number of Raman photons generated in the tumor layer (white markers) relative to those generated in the normal layer (black markers) is dramatically larger for the spatially offset detectors compared to the 0 mm offset simulation, especially for the thickest top layer. Figure 3.7 also illustrates the radial dependence of sampling volume on S-D offset, with that volume's width ranging from the excitation point to approximately twice the S-D offset.

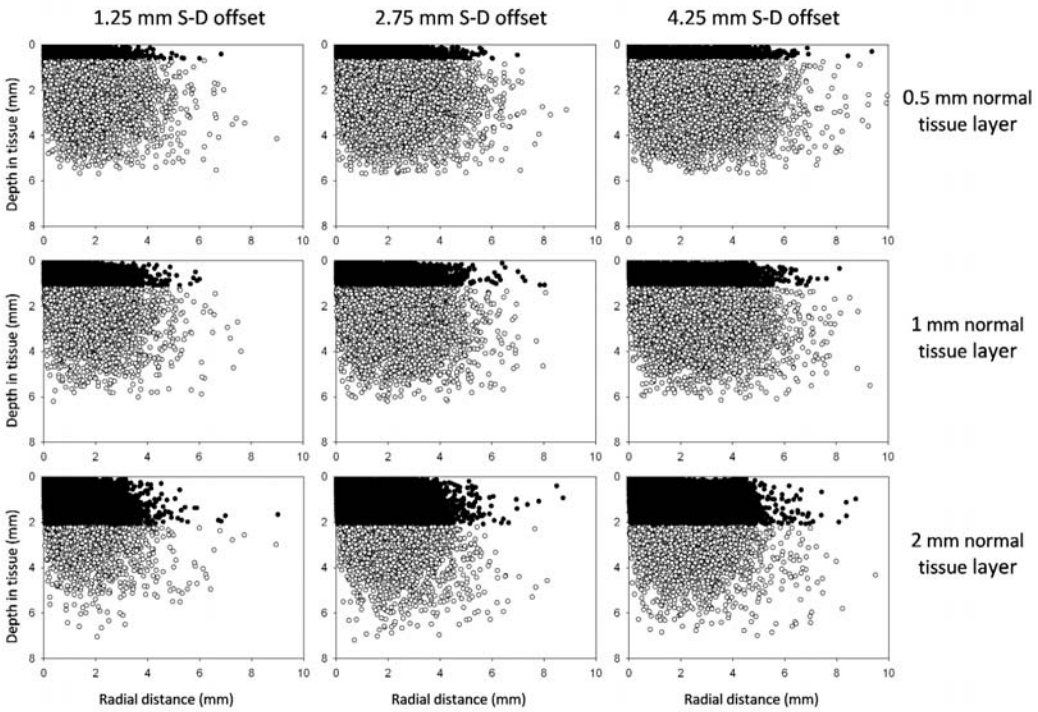

Figure 3.7 Visualizations of spatial origins of Raman photons from SORS simulations [169] using the tissue model shown in Figure 3.6. Tumor thickness is 5 mm in each plot. In each row, the thickness of the top normal layer is constant in all four plots, while the probe S-D separation increases along each row. Closed (black) markers represent Raman photons generated in the top (normal) layer of tissue, and open (white) markers represent Raman photons generated in the bottom tumor layer.

The axial dependence of Raman photon generation is more clearly depicted in Figure 3.8, which plots the depth of Raman events for each panel in Figure 3.7. From this figure, it is clear that the relative production of Raman photons from the tumor layer increases as S-D offset increases and top layer thickness decreases. A number of interesting effects can be seen besides the general drop-off in Raman photon generation with increasing depth. The coverslips, which are seen as blank areas, cause slight increases in Raman photon generation in their immediate vicinity due to index-mismatch reflections. This further

highlights the discontinuity in the plots at the boundary between the two layers that is otherwise caused by the lower Raman cross section of the tumor compared with normal tissue.

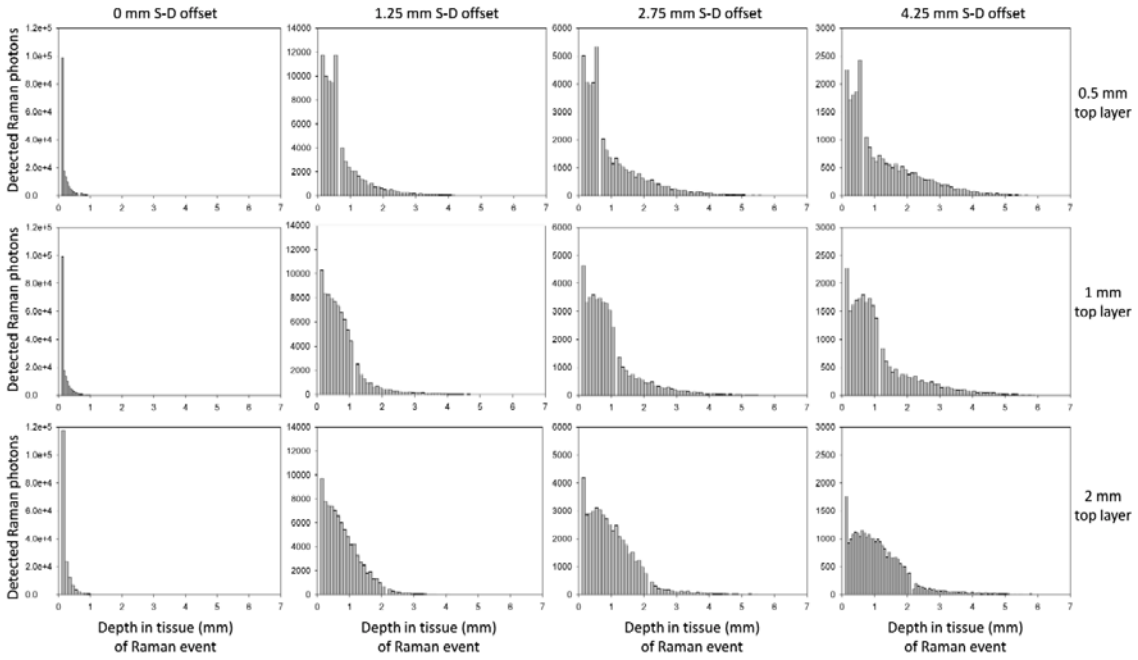

Figure 3.8 Histograms showing depth of Raman photon generation [169] for each panel in Figure 3.7. Coverslip layers are indicated by the zero-valued regions at the surface and between the two tissue layers.

To compare simulations versus experimental results in the remainder of the manuscript, the "relative tumor contribution" metric from our previous report [165] was approximated by dividing the number of detected tumor Raman photons by the total number of detected Raman photons. Figure 3.9 displays both the experimental and simulation results for relative tumor contribution versus source-detector offset for the constructs with normal breast tissue over breast tumors, as shown in Figure 3.6. Normal layers of 0.5, 1, and 2 mm were used as the top layer, while the bottom layer was fixed at

5 mm thick. Simulations used the optical properties from Table 3.2 and included the presence of the 100 μm thick quartz coverslips above and below the normal layer that were used in experimental measurements. Overall, the simulation and experimental data match well, with R^2 values of 0.95, 0.87, and 0.75 for the 0.5, 1, and 2 mm top layers, respectively. For the 2 mm top layer data, the simulation and experiment show better agreement past the 2.25 mm S-D offset point (R^2 of 0.85 for that range only). For smaller S-D offsets with the 2 mm top layer, the simulations indicated that there should be very small tumor spectral contributions to the overall detected Raman signal, but the experiments showed no measurable tumor contribution. Given the overall good fit between experimental measurements and simulations, the Monte Carlo model was then used to investigate the effects of changing various tissue construct parameters.

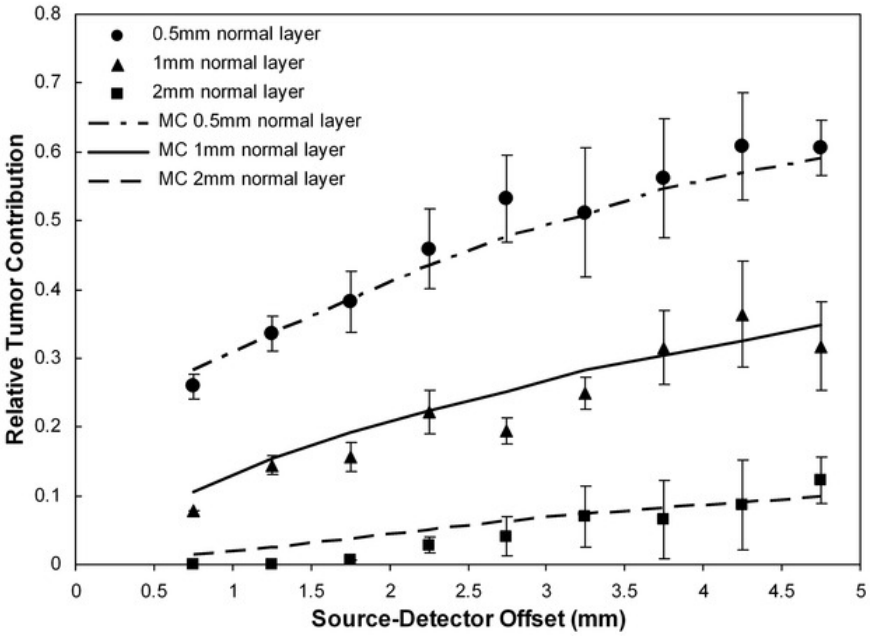

Figure 3.9 Experimental [165] (used with permission) and Monte Carlo results for relative tumor contributions from normal breast tissue layers 0.5, 1, and 2 mm thick, overlying breast tumors [169]. Error bars represent standard error over 3 different samples.

Figure 3.10 displays the relative tumor contributions from simulation results of tissue models with and without quartz coverslips encompassing the normal top layer. The results without coverslips are very similar to the ones with coverslips, but demonstrate slightly stronger relative tumor contributions. These differences range from ~20-25 % at the smallest S-D offsets to ~10% at the largest S-D offsets. From this result, it appears unlikely that the inclusion of quartz coverslips in the original experiment had a significant effect on the trends in relative tumor contributions to the detected SORS signal.

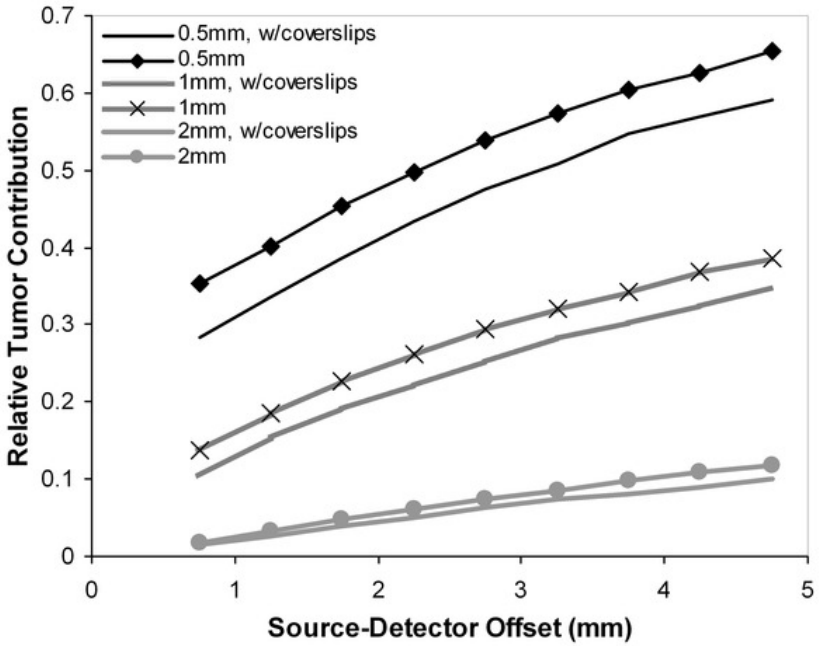

Figure 3.10 Simulated relative tumor contributions from layered tissue constructs, with and without the presence of clear coverslips, for normal breast tissue layers of 0.5, 1, and 2 mm overlying breast tumors [169].

The effect on the simulated SORS signals of changing the tumor thickness is shown in Figures 3.11(a-d) for increasingly thick top normal layers of 0.5 to 2 mm, respectively. The tumor thicknesses ranged from 2 cm (approximately semi-infinite relative to the penetration depth of NIR light) down to 100 μm, which is about the size of a few cells. All panels of Figure 3.11 predict that relative tumor contributions will not substantially decrease compared to that of the semi-infinite layer until the tumor thickness is less than about 3 mm. For tumor layers smaller than 3 mm, there is a relatively larger drop (e.g. from 3 mm to 1 mm compared with 20 mm to 3 mm) in how much tumor spectral signature can be detected at a given S-D offset. For tumor thicknesses less than or equal to 1 mm, Figure 3.11 predicts that the relative tumor contribution will not vary appreciably with S-D offset. For the most clinically relevant top layer of 2 mm, Figure

3.11(d) shows that there are minimal (less than 5%) spectral contributions from sub-millimeter thick tumor layers under a 2 mm normal layer for all S-D offsets. The results from the largest spatial offsets for the 0.1 mm thick tumor in Figure 3.11(a) are somewhat noisy, likely due to the high percentage of excitation photons that were transmitted through the two very thin layers.

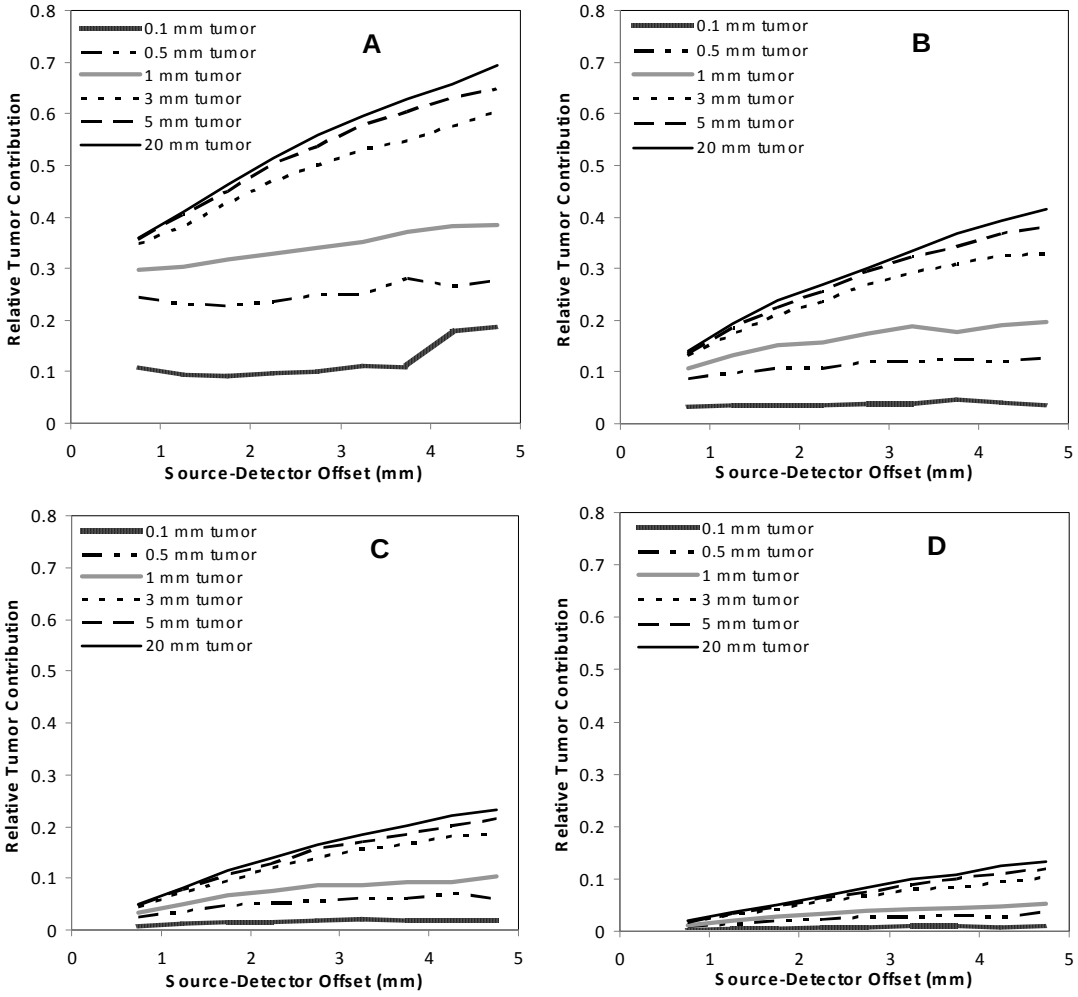

Figure 3.11 Simulated relative tumor contributions for various tumor layer thicknesses under (a) 0.5 mm, (b) 1 mm, (c) 1.5 mm, and (d) 2 mm normal layers [169].

The results shown in Figure 3.12 are from simulations identical to those in Figure 3.11, but for a three-layer tissue model that includes a 2 cm thick normal breast tissue layer

underneath the tumor to simulate conditions more likely to be seen in a clinical sample. For the two thickest tumor layers (20 and 5 mm), little to no difference is seen between all four corresponding panels of Figures 3.11 and 3.12, since not very many photons would enter the lower normal layer through the thick tumors. The same can be said for parts (c) and (d) of Figures 3.11 and 3.12 because of their thicker top normal layers compared with parts (a) and (b) of the two figures. Examination of these similarities between Figures 3.11 and 3.12 suggests that the bi-layered phantoms used for the SORS measurements in [165] were reasonable approximations of the more clinically relevant tri-layered tissue geometry. As the top normal and tumor layer thicknesses decrease, more differences become evident between the two figures. For tumor thicknesses of 1 mm and below, the curves in Figure 3.12(a) show lower relative tumor contributions than the corresponding curves in Figure 3.11(a) as the source-detector separation increases. This effect is likely due to the fact that the tumor volume has remained the same, but for the simulations shown in Figure 3.12, Raman photons can be generated below the tumor as well. In addition, relative tumor contributions from the 1 mm and 0.5 mm tumor layers in Figure 3.12(a) are essentially flat, indicating that photons entering any detector bin have passed through about the same volume of tumor tissue.

The initial goal of this study was to develop and validate a Monte Carlo model to accurately reflect experimental SORS results. As seen in Figure 3.9, the simulations were able to replicate the experimental data very well, with R^2 values of 0.95, 0.87, and 0.75 for the 0.5, 1, and 2 mm top layers, respectively. While the simulation results did not hit every experimental data point, this was expected given the noise in the experimentally

measured data points. The decrease in R^2 values with increasing top layer thickness makes sense because the absolute tumor Raman signal (represented by number of white markers in Figure 3.7 and y values in Figure 3.8 past the second coverslip), and therefore signal to noise ratio for "relative tumor contribution," decreased as the top layer thickness increased.

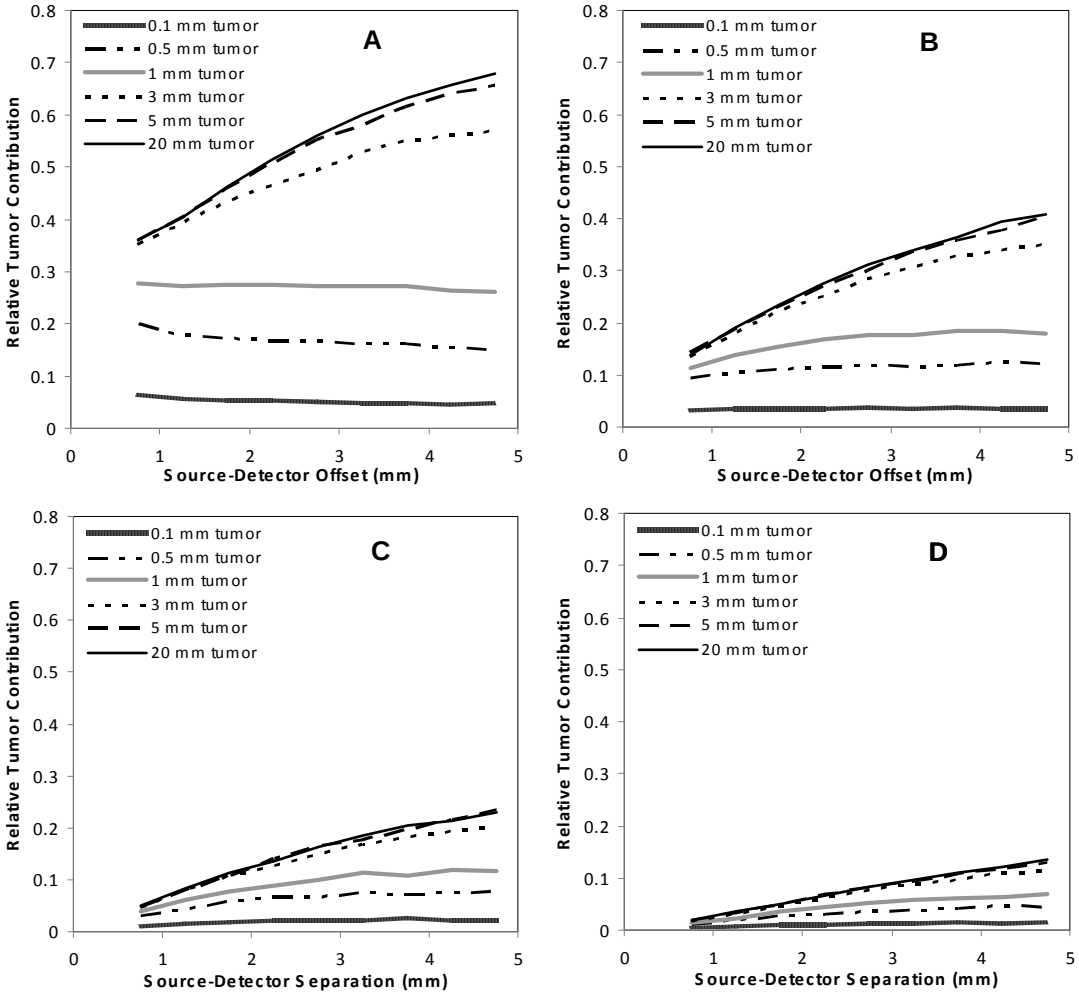

Figure 3.12 Simulated relative tumor contributions for various tumor layer thicknesses under (a) 0.5 mm, (b) 1 mm, (c) 1.5 mm, and (d) 2 mm normal layers, with an additional 20 mm normal layer underneath the tumor [169].

As noted above, there is only one region in Figure 3.9 in which the experiments and simulations differ systematically - the smaller spatial offset measurements with a 2 mm top normal layer. While the model predicted very small tumor contributions to the measured spectra (<= ~5%), no such contributions could be detected in the experimental data. It is likely, then, that a relative tumor contribution of about 5% represents the SORS detection limit of a tumor in practice, as such small spectral contributions would be equivalent in strength to noise levels present in the spectra. Applying this finding to simulations in Figures 3.11 and 3.12, we hypothesize that it would be possible to experimentally detect a very thin (100 μm) layer of tumor cells under 0.5 mm of normal breast tissue, while under 1 mm of normal tissue, the tumor detection limit would increase to a value between 100 and 500 μm thick. For the thickest top normal layer of 2 mm, Figures 3.11(d) and 3.12(d) suggest that it would likely not be possible to detect a tumor smaller than 1 mm thick. It should be noted that these detection limits are likely specific to the experimental setup and conditions of our previous studies [165]; other systems and conditions with different achievable signal to noise ratios could lead to slightly different limits.

The results reported here have a number of implications for using SORS for breast surgical margin analysis. From the detection limits discussion, it is likely possible to experimentally detect a positive margin up to 2 mm below the surface, as needed for the most stringent BCS requirements, but not if the tumor is < 1 mm thick in that region. For thinner normal layers, though, SORS is potentially capable of detecting a tumor layer only a few cells thick. Another conclusion is that it would be very difficult to determine

the exact depth of normal tissue over a tumor in a clinical setting, given how sensitive the 'relative tumor contribution' metric is to a number of factors. For example, from Figure 3.10, the inclusion of 100 μm thick, clear coverslips above and below the normal layer was enough to change the y-axis response by about 10-25% for given S-D offsets. Such a change is expected, though, since these clear layers give the photons more of an opportunity to travel further, both in depth and radially, without being scattered or absorbed in those layers.

The larger confounding factor in experimentally determining exact margin size is evident in Figures 3.11 and 3.12; namely, the effect of tumor layer thickness. For the same normal tissue layer, the observed relative tumor contribution differed by up to a factor of ~7 based on size of the tumor. In some cases, the presence of normal tissue beneath the tumor also changed the trend in relative tumor contribution as a function of S-D offset. While most lines in Figure 3.12 slope upward, the response is nearly flat for thinner tumor layers. This occurs because all of the photons being Raman scattered into any detector pass through the same volume of tumor regardless of how deep their trajectories extend into the lower normal layer. With all of these confounding factors, it therefore seems unfeasible to use SORS to determine an exact negative margin size unless significant *a priori* information is available about the tissue geometry, as in the use of computed tomography (CT) to improve the recovery of Raman tomography signals from bone [186]. Given the intended use of this technique to interrogate freshly excised samples during an operation, such an approach does not seem practical. Although one could also imagine using transmission Raman spectroscopy (TRS) to provide some tumor

geometry information while eliminating the need for a truly multi-modal approach, the spatial resolution of TRS is currently insufficient [187] given the typical size of the specimens removed during BCS (>5 cm cuboids).

Based on the results presented here, a more viable approach for using SORS to evaluate excised breast specimen surgical margins would be simply to look for any evidence of tumor Raman spectral signatures from detector channels that are known to sample to the desired depth. From Figures 3.10-3.12, limiting the spatial offsets to 3.5 mm or less would effectively suppress any spectral contributions from tumors > 2 mm below the surface of normal tissue (to avoid false positives), while still being able to interrogate up to 2 mm beneath the surface. At spatial offsets larger than this, achieving adequate signal-to-noise ratios can be difficult as well.

The SORS Monte Carlo code presented here showed good agreement with experimental results and provided useful predictions about the effects of tissue geometry on SORS measurements. A primary shortcoming of the current code, however, is that tissues had to be represented as stacks of planar, homogeneous slabs. In reality, breast tumors do not have planar boundaries with layers of normal tissue and are not infinitely broad and wide. Modeling a thin layer of tumor between two layers of normal tissue is a reasonable first step in investigating the detection of small tumor "projections," but it remains to be seen what would happen, for example, if such a projection ran in the direction parallel to the fiber optics rather than perpendicular. To this end, work is underway on a mesh-based SORS simulation code capable of creating irregularly shaped layers of finite sizes to

examine their effect on tumor detection limits.

In conclusion, this work is expected to provide major insights into the use of SORS for evaluating margin status after partial mastectomies. In particular, the model has predicted that S-D offsets up to 3.5 mm are needed for clinically relevant depth interrogation during BCS. It has also suggested likely tumor-thickness detection limits for SORS in human breast tissues; for the most clinically useful value of a 2 mm margin, the model predicted that a tumor greater than 1 mm thick can be detected. Future experimental work will be focused on using these results to design and test a multi-separation probe capable of effective sampling from the surface down to the clinically relevant depths in human breast tissue. In addition, the Monte Carlo code developed here could easily be adapted to examine other layered soft tissues, provided information about their optical properties and relative Raman cross sections are known.

3.3. Design and testing of Raman probe for breast tumor margin detection

For many of the approximately 180,000 women diagnosed with early-stage invasive breast cancer or carcinoma *in situ* each year [188], a viable treatment option is breast conserving therapy (BCT). The surgical portion of BCT involves a partial mastectomy, or lumpectomy, to remove only the primary lesion with a small amount of surrounding normal tissue [189]. Depending on the hospital, the depth of normal tissue required from the surgical margin (i.e. the surface of the excised specimen) to the tumor is typically 1-2 millimeters [173]. This situation is illustrated in Figure 3.13; if a sufficient amount of normal tissue exists, as in the right side of Figure 3.13, the margins are said to be negative for tumor. If tumor-positive margins are found, as shown on the left side of Figure 3.13, a second operation is necessary because positive margins are a major predictor of local tumor recurrence [172]. Currently available intraoperative margin evaluation tools, such as simple visual examination, ultrasound, cytological examination ("touch prep"), and frozen section analysis, all have significant drawbacks in terms of accuracy and/or time required [175-177, 190], so there is a need for an automated, real-time method to accurately evaluate surgical margins during BCT.

Spatially offset Raman spectroscopy (SORS) has been shown to be a reliable method for recovering biological Raman spectra from depths greater than those possible with standard techniques [39, 147, 149, 161, 165-168, 191]. It does so because detection elements spaced radially further from source elements are more sensitive to photons traveling deeper beneath the tissue surface and to greater radial distances due to multiple scattering (Figure 3.13). It has been previously demonstrated that SORS can detect

spectral contributions from breast tumors buried under 0.5 to 2 mm of normal breast tissue [165]. A SORS Monte Carlo code (Section 3.2) was developed to quantify signals obtained from layered constructs of normal breast tissue overlying breast tumors [169]. In particular, the code was used to examine the effects of layer thicknesses and overall geometries on relative tumor contributions to detected spectra for a range of source-detector (S-D) offsets [169]. To detect a tumor signature within the first 2 mm from the surface, the resulting spectrum at a given S-D offset must contain at least a 5% contribution from the tumor. To achieve this level of contribution, it was found that the tumor would have to be ~0.1 mm thick under 0.5 mm of normal tissue, or ~1 mm thick under 2 mm of normal tissue [169].

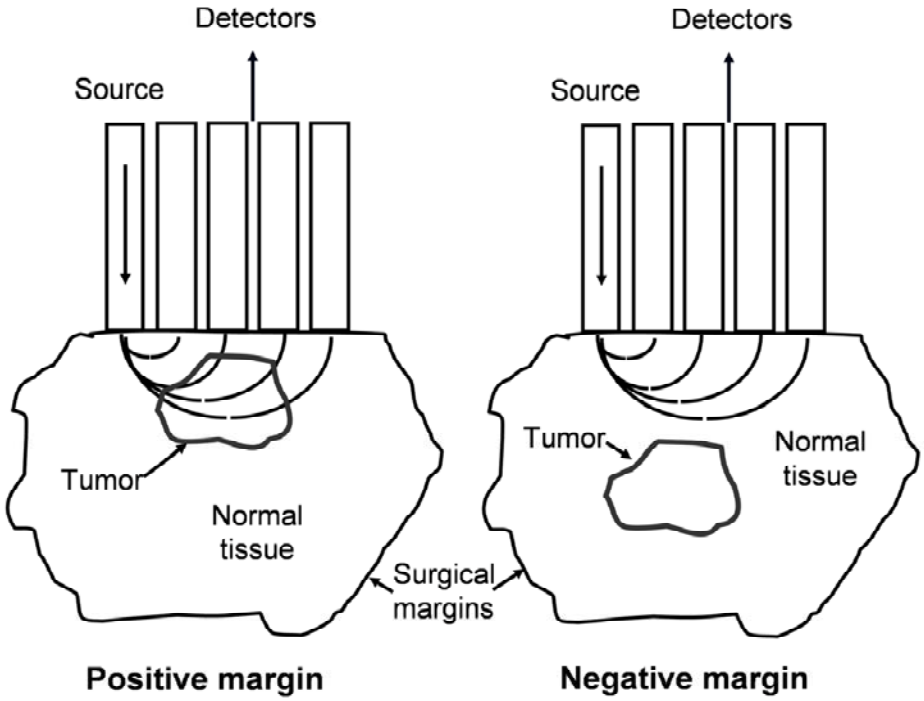

Figure 3.13 Drawing of tumor-positive versus tumor-negative margins, defined by the distance between the surgical margin and the tumor boundary [192]. Overlaid are general photon migration paths demonstrating the advantage of SORS for this application.

Combining the results of experimental [165] and numerically simulated [169] SORS indicated that to be sensitive to breast tumors located up to 2 mm beneath normal breast tissue, as needed for surgical margin evaluation, a maximum S-D offset of ~3.5 mm should be used. With larger offsets, the measurements could possibly detect large tumors from over 2 mm deep and create false positives; also, recording spectra with adequate signal-to-noise ratios (SNRs) at larger offsets is difficult since fewer photons tend to escape the tissue surface as the S-D offset increases. In addition, a shortcoming of the previous experimental work was the need to translate the single detector fiber for each measurement. Thus, the goal of this work was to design, test, and implement a multi-separation SORS probe for breast tumor surgical margin evaluation. In particular, this section describes the use of the previously developed SORS Monte Carlo code to investigate the theoretical drop in SNR as a function of S-D offset, the design of a SORS probe based on the above theoretical and experimental findings, its testing to ensure comparable signal quality in each detector ring, and its use in acquiring spectra from breast cancer samples to assess its ability to accurately evaluate surgical margin status [192].

The primary criterion for designing a SORS probe for breast tumor margin analysis was to ensure proper depth sampling - that is, to develop a probe sensitive to tumor spectral signatures if the tumor is anywhere within the first 2 mm in depth from the excised surface. As noted, the relevant S-D offsets for this purpose were determined to be < 3.5 mm. To investigate the drop in SNR as S-D offset increases, SORS Monte Carlo simulations were run using the same model as for previous results [169]. Simulations

were run for 3-layered samples, consisting of a top layer of 0.5, 1, or 2 mm of normal breast tissue, a 0.1 to 20 mm thick middle layer of breast tumor, and then a 2 cm thick bottom layer of normal breast tissue to mimic the clinical situation of semi-infinite geometry. As a metric for SNR, the total number of simulated Raman photons, originating from any layer, reaching each detector bin was counted and normalized to a maximum of 1, since we are only interested in how SNR falls off with S-D offset. Because the raw signal strength was consistent among the four rings, it was assumed that noise levels were consistent among the four rings as well. Figure 3.14 shows the mean of these SNR curves; since the standard deviation was less than 1% over the range of thicknesses for the top two layers, no error bars are shown.

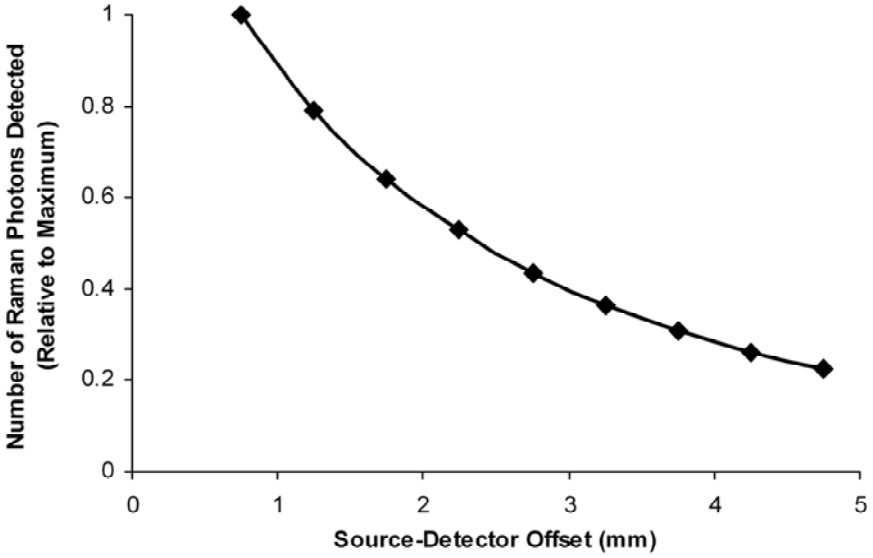

Figure 3.14 Simulation results for total number of Raman photons detected as a function of S-D offset [192], normalized to a maximum of 1. Results were averaged for a variety of thicknesses of the top two tissue layers (0.5 to 2 mm for top normal layer, 0.1 to 20 mm for middle tumor layer). No error bars are shown because the standard deviation was less than 1%.

As predicted, the number of Raman photons detected fell off at what appears to be an exponential decay as a function of S-D offset. Although the trend of SNR as a function of S-D offset was consistent regardless of relative thicknesses of normal and cancerous breast tissues, the trend may not hold for other tissue types, especially those in which optical properties can vary more drastically in inhomogeneous regions.

These results were used to aid the design of a multi-separation SORS probe (assembled by EMVision, Loxahatchee, FL), whose distal tip is shown in Figure 3.15. A single 400 μm diameter source, or excitation fiber is found on one end, and four (partial) rings of 300 μm diameter collection fibers extend radially outward. The excitation fiber includes a bandpass filter at its tip to narrow the laser line, and the collection fibers have longpass filters at their tips to reject elastically scattered light. The center to center distances of the excitation fiber to each detection ring are 0.5, 1.5, 2.5, and 3.5 mm. Based on Figure 3.14, an additional collection fiber was added to each consecutive detector ring to make the SNRs from each ring more comparable to one another. While the curve in Figure 3.14 is not linear, adding a single fiber for each larger-offset ring provided the closest approximation of equivalent SNRs if all of the fibers in each ring were binned. Adding a fiber in each successive detector ring had an added benefit of increasing the lateral sampling volume of the probe as well.

The SORS probe delivered 80 mW of power from a 785 nm diode laser (I0785MB0350M, Innovative Photonics Solutions, Monmouth Junction, NJ). The collection fibers delivered light to a NIR-optimized spectrograph (LS785, Princeton

Instruments, Princeton, NJ), which dispersed the light to be recorded by a deep depletion, thermo-electrically cooled CCD (Pixis 400BR, Princeton Instruments).

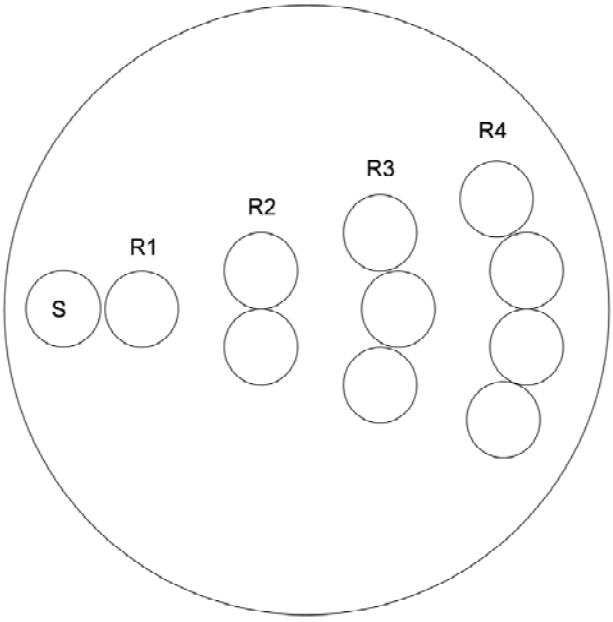

Figure 3.15 Schematic of tip of SORS probe [192]. S – source fiber, all other circles – collection fibers. Each ring of collection fibers is separated by 1 mm (center to center) from the previous ring, with 0.5 mm between the centers of the source fiber and the first detector ring (R1).

Each acquisition with the SORS probe recorded four spectra – one from each detector ring. Each ring was calibrated separately since the inherent curvature in the detection system created slight, but noticeable differences in peak locations on the CCD among different rings. A neon-argon lamp, naphthalene, and acetaminophen standards were used to calibrate the wavenumber axis, and a NIST-calibrated tungsten-halogen lamp was used to correct for the system response [193]. After wavenumber binning (in 3.5 cm^{-1} steps given the system resolution of ~7 cm^{-1}) and noise smoothing, the background fluorescence was subtracted with a modified polynomial fit algorithm [193], and the

spectra were normalized according to their overall mean intensities. To create a composite spectrum with equal weighting from all four rings, which would contain information from the entire 2 mm sampling depth, the binned spectra from each of the four rings were averaged after processing.

To ensure the probe's ability to gather spectra from each ring with comparable SNRs, spectra were acquired for 20 seconds each from 12 different spots on a ~1 cm thick piece of chicken breast (muscle). The spectra were processed as described previously, and the SNR of the binned spectrum from each ring was calculated by dividing the height of the 1445 cm^{-1} peak, which is the strongest peak in all samples measured, by the standard deviation of the flat (i.e. no Raman signal) spectral range between the peaks at 1656 and 1750 cm^{-1}, which represent the noise inherent in the system that could not be removed via pre- or post-processing.

With approval by the Vanderbilt Institutional Review Board (#050551) and the US Army Medical Research and Materiel Command's Human Research Protection Office (USAMRMC HRPO), fresh-frozen human breast tissue samples were acquired from the Cooperative Human Tissue Network. Frozen-thawed tissues are not perfect surrogates for freshly excised tissue, as their optical properties can differ from each other [194]. A recent study by Reble, *et al.* [195] demonstrated that Raman sampling volumes can vary substantially based on a tissue's optical properties, especially the reduced scattering coefficient. Nevertheless, using such tissues is a common first step for breast cancer studies [194, 196], and a recent study showed nearly equivalent performance of an

algorithm for differentiating normal, benign, and malignant breast tissues developed with *in vitro* Raman spectra and applied to *in vivo* measurements [197].

In total, 35 samples were included in the study; 15 samples had either no tumor (n=13) or tumor > 2 mm beneath normal tissue at the point of measurement (n=2) and were thus labeled as "negative margins," while 20 samples had tumor (15 invasive ductal carcinoma [IDC] and five invasive lobular carcinoma [ILC]) regions within the first 2 mm from the measurement surface, and were thus labeled "positive margins." Of the negative samples, seven were predominantly adipose, and eight were varying compositions of adipose and fibroglandular tissue. Of the positive samples, eight had tumors underlying various compositions of normal tissue ranging from 0.1 to 1.5 mm thick, and 12 samples had tumor regions at the surface under at least part of the probe. Wherever possible, measurements from tumor samples were taken such that the SORS probe was placed on a small region of visually normal-appearing tissue on top of the actual tumor to mimic the situation of margin evaluation. Spectra were recorded for 10-30 seconds and processed as above. Measurement sites were inked, fixed in formalin, and serially sectioned to correlate the spectra with histopathology diagnoses of tissue type and the depths from the measurement surface of those tissues. In this manner, the analysis was done to discriminate “negative” margins from “positive” margins.

The composite spectrum from averaging all four detector rings was used for analysis, and if there were histological evidence of tumor cells within 2 mm of the measurement surface, the "margin" was considered positive. All tumor-positive measurements were

lumped into a single category since the surgeon simply needs to know whether any types of malignant cells remain too close to the margin. Discrimination was performed with sparse multinomial logistic regression (SMLR) [198], a Bayesian machine-learning framework that computes the posterior probability of a spectrum belonging to each tissue class based on a labeled training set. In the case of this binary analysis, whichever class had the higher probability of membership was the one to which the spectrum was classified. SMLR also includes inherent dimensionality reduction as it seeks to create sparse basis vectors, which is important for these data sets given their small sizes. Since each *in vitro* sample had only one measurement site (their sizes relative to the probe precluded multiple independent sites), SMLR was run with leave-one-out cross-validation. A range of input parameters to SMLR were tested, and the combination that provided the most accurate classification, while also maximizing sparsity, was using a Laplacian prior, direct kernel, lambda value of 0.01, and not adding a bias term.

Figure 3.16 shows the results of the SNR testing on chicken muscle. Rings 1 and 4 of the SORS probe, with one and four fibers per ring, and with S-D offsets of 0.5 and 3.5 mm, respectively, displayed nearly identical SNRs. Rings 2 and 3 showed smaller SNRs compared with Ring 1, but only by ~30% and 20%, respectively. This trend was expected based on the shape of Figure 3.14, although the signal strengths of rings 2 and 3 were smaller than predicted by the simulations. The likely reason is that when imaging the detection fibers for the two middle rings during alignment and testing, their throughput appeared to be lower compared with the fibers for rings 1 and 4. Even so, the design of the SORS probe effectively accounted for SNR fall-off with increasing S-D offset.

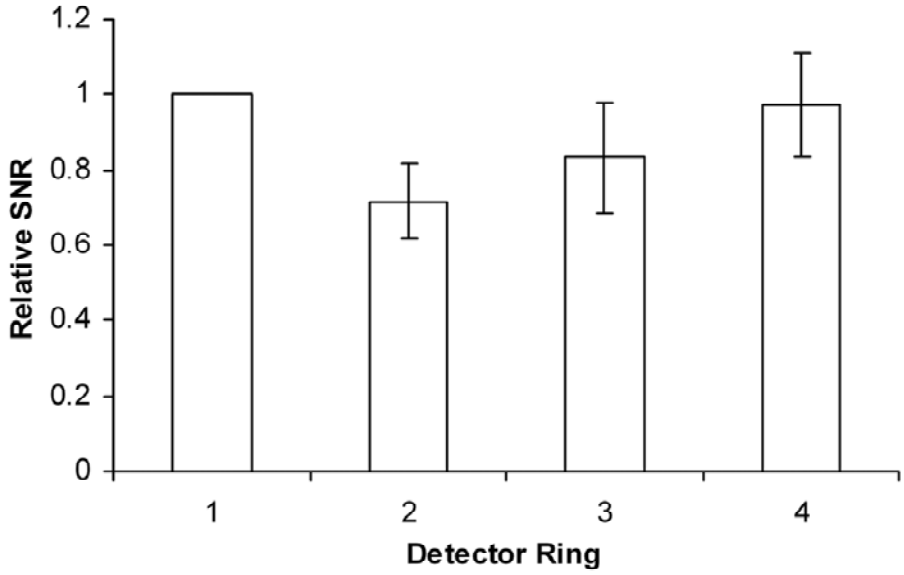

Figure 3.16 Mean (n=12) signal-to-noise ratios (SNR), plus or minus one standard deviation, for spectra of chicken muscle binned within each detector ring and normalized to SNR of first ring [192].

Figure 3.17 shows typical composite spectra recorded from pure normal breast tissue and a pure breast tumor (invasive ductal carcinoma) with the SORS probe. As in the previous study [165], there are numerous spectral regions with major differences between the two tissue types. In particular, tumor tissue contains a strong band at 1006 cm^{-1}, usually attributed to phenylalanine, while normal tissue does not. The ratios of the 1303 cm^{-1} to 1265 cm^{-1} bands, indicative of the ratio of lipid to protein content, are very different between the tissue types, and the amide I band centered around 1656 cm^{-1} is much wider in tumor compared to normal - again indicative of increased relative protein contributions in the cancerous tissues. Also, the 1445 cm^{-1} CH stretch band is relatively more intense in normal tissue, and the normal tissue contains a carbonyl stretch peak around 1750 cm^{-1}, typically due to fat content, while the tumor tissue does not.

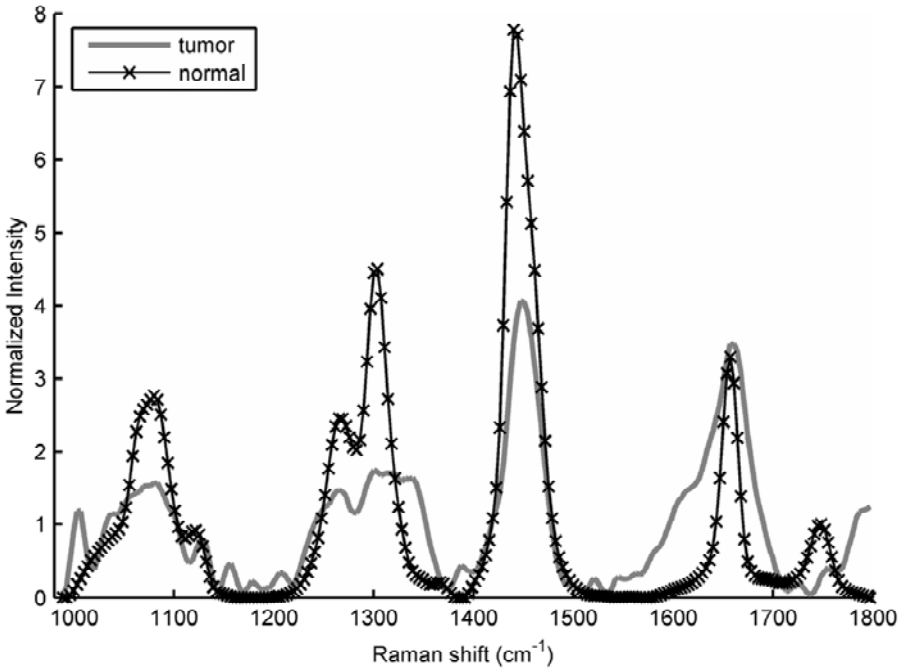

Figure 3.17 Typical normalized composite spectra from SORS probe of normal breast tissue versus malignant breast tumor tissue [192].

Figures 3.18 and 3.19 show H&E stained tissue sections and the SORS spectra from those sections from three different (Figure 3.18, Figure 3.19(a, b), Figure 3.19(c, d)) *in vitro* tumor samples. In all histological images, the "S" arrow indicates the placement of the source fiber, while the "R1," "R2," etc. labels denote the location of the individual collection fiber rings.

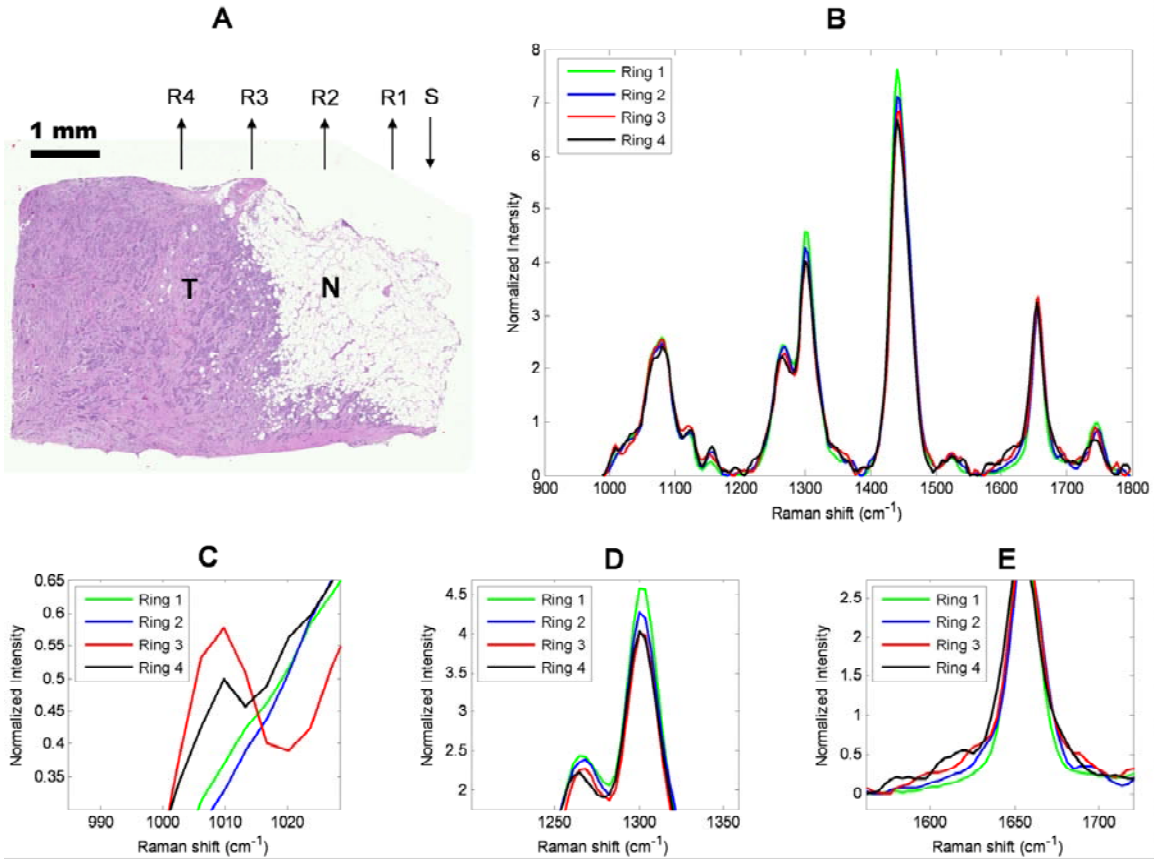

Figure 3.18 (a) H&E stained tissue section of IDC sample with large area of normal fat (white colored area with "N") on the right, and solid IDC tumor (darkly stained area with "T") on the left. Arrows indicate the placement of the source fiber (S) and each of the detector rings. (b) Binned SORS spectra for each detector ring from tissue in (a). To aid in the visualization of relevant, but subtle spectral changes, zoomed-in versions are shown for (c) the 1006 cm^{-1} phenylalanine peak, (d) the 1265 cm^{-1} amide III and 1303 cm^{-1} lipid peak, and (e) the shoulders of the 1656 cm^{-1} amide I peak [192].

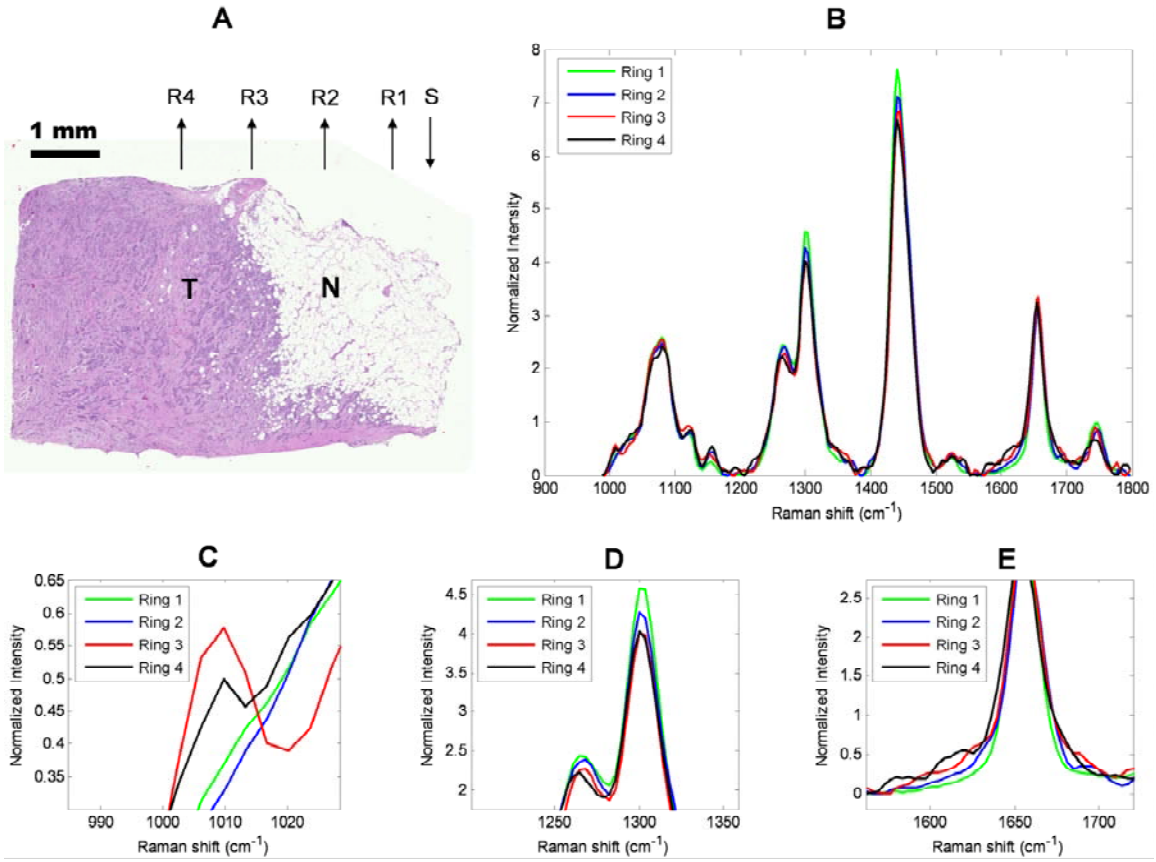

Figure 3.19 (a) H&E stained tissue section of ILC sample with pockets of normal fat ("N") near surface of otherwise darkly stained tumor tissue ("T"). Arrows again represent placements of fibers. (b) SORS spectra for each detector ring from tissue in (a). (c) H&E stained tissue section of IDC sample with underlying fat and (d) corresponding SORS spectra [192].

In the tissue sample from Figure 3.18(a), the probe was delivering light to a large fatty area, as seen by the whitish (formerly lipid-filled) vacuoles, while only the outermost collection fibers were placed over a portion of the tumor, which comprises the remainder of the darkly stained section. Since spectral differences among detector rings in Figure 3.18(b) are visually subtle, except for differences around 1445 cm^{-1}, close-ups of three spectral regions are shown in panels (c)-(e) of Figure 3.18. These plots show definite trends indicating that the closer rings are sampling normal tissue, while the outer rings

are picking up slight spectral contributions from the tumor as well. By qualitatively comparing the spectra in Figure 3.18(b) with the typical pure normal and tumor spectra from Figure 3.17, these trends include the increasing presence of the 1006 cm^{-1} peak, the lesser relative contributions from the 1303 and 1445 cm^{-1} peaks, and the increasing width of the 1656 cm^{-1} peak as source-detector offset increases. These trends are similar to those seen in the earlier report of SORS on layered breast tissues [165], but in this case, the tissue boundary was vertical rather than horizontal.

The example in Figure 3.19(a, b) provides an illustration of what happens with smaller layers of normal tissue over a tumor. Figure 3.19(a) shows a sample with a large tumor region but with pockets of normal adipose cells near the surface, including directly under the location where the excitation fiber from the probe was placed. From Figure 3.19(b), in comparison to Figure 3.17, the spectrum from the smallest S-D offset contains mostly features indicative of normal fatty breast tissue, while spectra from the larger S-D offsets contain features indicative of tumor spectral signatures, as noted above. The sample from Figure 3.19(c, d) is included to confirm that if the excitation side of the probe is placed on tumor tissue overlying normal tissue (i.e. the opposite of margin analysis), then the inner detector rings picked up tumor signatures, while the outer rings picked up the appropriate degree of normal spectral signatures. Thus, it is clear that the different detector rings are sampling different volumes, as desired.

To simplify the "margin analysis" procedure, the spectra from each detector ring were averaged to create one composite spectrum per *in vitro* sample. Thus, a single

histological classification could be correlated to a single spectral classification. Table 3.3 shows the confusion matrix for classification of these composite spectra with SMLR.

Table 3.3 Confusion matrix for "margin analysis" on *in vitro* specimens [192].

		Spectral Margin Status		
		Negative	Positive	
Histopathology Margin Status	Negative	15	0	Specificity: 100%
	Positive	1	19	Sensitivity: 95%
		NPV: 94%	PPV: 100%	

This analysis showed an excellent ability for SORS to evaluate margin status in breast specimens, with 95% sensitivity and 100% specificity, and an area under the ROC curve of 0.993. Alternatively, the discrimination was performed with 94% negative predictive value (NPV) and 100% positive predictive value (PPV). The one false negative came from a tumor sample which, after formalin fixation and sectioning, was found to have a ~1.5 mm layer of normal tissue between the measurement site and the tumor. Since it has been shown that normal tissue margins tend to shrink by an average of 33% during formalin fixation [199], it is possible that this normal layer was at least 2 mm thick when the spectra were obtained.

This section presents the design, testing, and implementation of a multi-separation SORS probe for use in evaluating surgical margin status following partial mastectomies. The design, as shown in Figure 3.15, was based on results from our earlier experimental and simulation-based studies [165, 169], and from the SNR simulation results from Figure 3.14. To ensure that the SNRs were comparable across the different detector rings, a series of measurements was performed using the common soft tissue optical phantom of chicken breast. As seen in Figure 3.16, the design of adding an additional collection fiber for each further-offset ring worked well to keep the SNR of each ring no more than ~30% different from the others. Given the exponential shape of Figure 3.14, it would be very difficult to design a probe to both sample the desired depths in tissue and achieve even better equilibration of SNR among the various detector rings. Besides the SNR balancing, the probe design from Figure 3.15 also appeared to sample tissue to the expected depths based on earlier experimental [165] and simulation [169] results. This conclusion is supported by the success shown in Table 3.3 for classifying spectra according to margin status using 2 mm as the cutoff value for negative vs. positive classification.

The ability of the detector rings to sample different volumes is demonstrated in Figures 3.18 and 3.19. From Figure 3.18(a), it is clear that the SORS probe was placed over two very different regions of tissue for that specimen. A large area of normal fatty tissue was found directly under the excitation fiber and the first 2-3 detector rings, while the outermost 1-2 detector rings were placed against the tumor. Comparing Figures 3.18(b-e) to the pure normal and tumor spectra from Figure 3.17, rings 1 and 2 show essentially no tumor spectral signatures. Given this, a standard Raman probe placed in the same spot

would not detect any positive margin findings at this point. The 3rd and 4th rings of the probe were able to detect slight tumor contributions though, indicating that they successfully sampled a different volume of tissue than the inner rings. While most spectral regions showed increasing tumor contribution from ring 1 to ring 4, ring 3 had a stronger relative 1006 cm^{-1} peak than ring 4. Possible causes for this include a slight mis-alignment between the probe and histology, especially considering rotation of the probe, or inconsistent biochemical composition of the tumor tissue sampled by rings 3 and 4. A similar situation to Figure 3.18 is seen in Figure 3.19(a, b), although only the first detector ring was sensitive to a small (< 1 mm thick) fat layer on the surface, while the outer rings sampled deeper and more radially distal tissue volumes. It should be noted that in the fixation of samples, the fat regions tend to shrink [199], so the measurement surface of these specimens were likely flatter during signal acquisition. Also, all specimens were cut after fixation and before sectioning to make a given section contain only the interrogated tissue region, so the fibers were never placed over the edge of any sample.

The opposite situation of the above two samples is shown in Figure 3.19(c, d), where the source fiber was placed over a tumor region ~1-1.5 mm thick, with normal tissue underneath; outer detector rings were placed over a considerably thinner tumor layer with more underlying normal tissue. Taken with the above results, these panels demonstrate that the spectral signatures collected with the SORS probe vary appropriately as a function of S-D offset according to tissue type and location, not via any systematic response. Since some normal Raman signatures are present even in the Ring 1 spectra,

Figure 3.19(c, d) also shows that the presence of normal tissue under tumor tissue would be easier to detect than the current problem, since fat is a stronger Raman scatterer than tumor tissue [169].

Given these findings regarding sampling depths and volumes, the composite spectra were used for margin analysis on intact breast specimens in the laboratory. Since the SNR is approximately equal in all four rings (see Figure 3.16), averaging them provides information about the entire sampling volume in a single spectrum. This method also simplifies the analysis procedure; if spectra from individual rings were used, it would be difficult to determine how to correlate certain ones with pathology findings. For example, although all spectra in Figures 3.18(b) and 3.19(b) were from tissue sites that would be deemed positive margins within the spatial extent of the probe, it is unlikely that the innermost rings were actually detecting any signal from tumor tissues. A possible approach for using the individual spectra would be to label a measurement site "positive" if any spectrum from the four rings is predicted to be from a positive margin, but the aforementioned correlation issue arises in the training of such an algorithm for a retrospective analysis. Many normal-looking spectra, like ring 1 from Figure 3.18(b), would be labeled as tumor and would likely cause difficulties for discrimination algorithms trying to create decision boundaries between negative and positive margins.

A binary diagnostic algorithm simpler than SMLR may seem like a more appropriate approach in this analysis, but the SMLR algorithm was able to significantly reduce the dimensionality of the data from the initial size of 232 variables (one per 3.5 cm^{-1} bin) to

perform its classification. In addition, SMLR provides a probability of class membership that would be very useful in a clinical application. A surgeon could act differently if the probability of a margin being negative is 99% versus 51%, although in either case, the diagnosis would be "negative."

The results from using SMLR to classify the composite SORS spectra according to margin status are shown in Table 3.3. With only one false negative, the sensitivity, specificity, NPV, and PPV were all at least 94%. For this clinical application, perhaps the most important variable for long-term studies is NPV, since a surgeon needs to be confident in any diagnosis of negative margin status to prevent recurrence of the disease or unnecessary second operations. For the single false negative result in this study, the normal layer overlying the tumor was found to be ~1.5 mm thick upon histological examination, but prior to formalin fixation, this layer was likely around or slightly greater than 2 mm thick [199], which would surpass the sampling capabilities of the SORS probe. It may also be possible that a slight mis-alignment between the probe and the point of the histological section led to an error in the margin size determination. In addition, there is not a universal standard among hospitals of minimum margin size required during breast conserving surgery; rather, some locations use 2 mm, some use 1 mm, and others simply require that no cancer cells be found on the surface of the specimen [173]. A value of 2 mm was used as the cutoff in this study because that value provides the best prognosis for patients [173] and is the most stringent standard for proving the value of SORS.

The classification results above compare extremely favorably with current intraoperative margin evaluation techniques [175-177, 190]. For example, the reported sensitivity of "touch prep" is as low as 8% [175]; simple visual examination has sensitivity and specificity of approximately 50% and 72%, respectively [177]; and frozen section pathology, though its sensitivity and specificity per slide are generally > 90%, suffers from sampling error that brings per-specimen classification accuracy (i.e. overall designation of whether a second operation is required) below 85% [190]. Another optical approach for intraoperative margin evaluation is to image an entire margin (i.e. one of the six facets of the "cuboidal" excised specimen) at once with autofluorescence and/or diffuse reflectance modalities. Using extracted optical properties of the tissue from visible diffuse reflectance, that group has achieved 79% sensitivity and 67% specificity for discriminating normal from positive or close (< 2 mm) margins for a set of 48 patients [200]. Better classification - 100% sensitivity and 82% specificity - was achieved by Nguyen *et al.* using OCT [201], though the sample size of 20 patients was much smaller, and the technology in its current state still relies on a subjective analysis of the images. The biggest challenge for the SORS approach presented here, especially compared with the above two techniques, is adapting the probe and other system components to interrogate larger areas of tissue in a shorter time.

The various optical approaches to intraoperative margin evaluation all hold significant potential for improving the standard of care, though each currently has its own strengths and weaknesses. To date, no method has demonstrated the combination of sampling speed, volume, and diagnostic accuracy needed for widespread clinical implementation.

The initial work presented here has demonstrated the feasibility and promise of using SORS to evaluate margin status on intact breast specimens in a laboratory setting. Studies are currently underway on using the same approach in a clinical setting, and initial results are equally as promising as the laboratory measurements.

Chapter 4

Monte Carlo models for tissues with irregular interfaces

Monte Carlo (MC) simulations are accurate and quantitative models for photon transport in biological tissue [75-77]. For layered tissues, MC codes frequently approximate the structure of each tissue layer as a homogeneous slab with flat upper and lower boundaries. Recently, MC codes have been developed for tissue models where the boundaries are defined by surface meshes (Figure 4.1); this technique has been applied to simulations of diffuse reflectance in bone [79] and fluorescence in a whole-mouse model [202]. Here we describe a MATLAB-based MC code for user-friendly simulation of time-resolved fluorescence in tissues with irregular interface geometry [203].

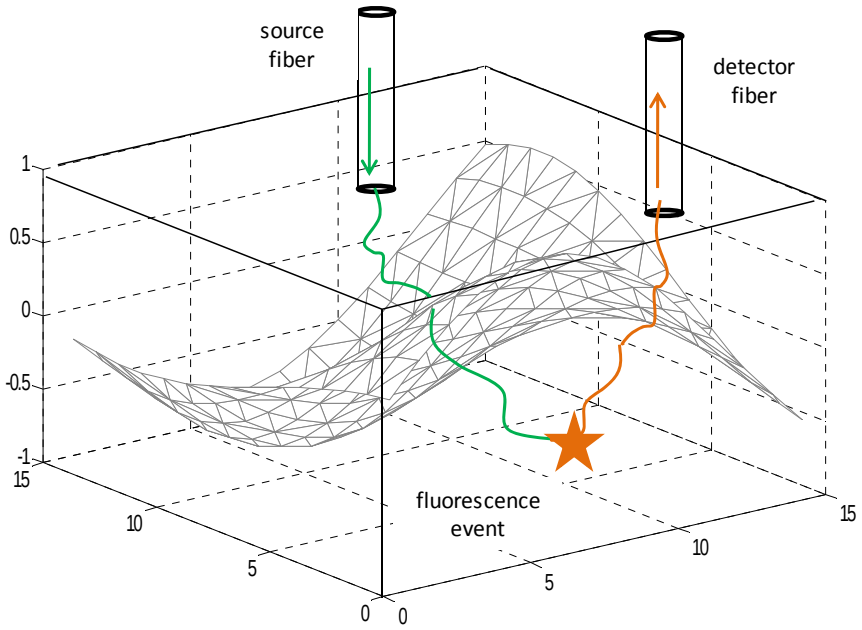

Figure 4.1 Representative path of photon in bi-layered tissue model where photons enter and exit at a top surface that is flat but can cross an irregular internal interface during their path in the tissue [203]. Here, the buried interface is given by the equation $z(x,y) = \sin(x/4)\cos(y/4)$ and represented as a triangle mesh. An excitation photon (green) can undergo a fluorescence event (orange star) and return to the surface as an emission photon (orange).

The MC algorithm described in this section is a modified version of a pre-existing code written in C [37, 76, 77]. The new code was written in MATLAB, which provides a uniform, cohesive environment for importing simulation inputs such as mesh geometries and optical property spectra, as well as performing the photon transport simulations and visualizing the results. The MATLAB language is intuitive and familiar to a wide range of scientists and engineers, so the code will be easy for researchers to modify as needed. The MATLAB code can be easily modified for a wide range of source-detector configurations, tissue properties, and interface geometries. The code can model temporally- and spatially-resolved fluorescence, and it can be easily modified to store the

spatial and temporal origins of all detected fluorescence events to enable 3D fluorescence visualizations [77].

The use of surface meshes to represent tissue interfaces allows the simulation of photon propagation in realistic tissue geometries. Meshes can be defined in MATLAB, created using CAD software, or imported from CT or MRI images. Incorporating mesh surfaces into the MC code increases the computation time due to the large number of surface elements that are examined to identify when a photon path intersects a boundary. One way to reduce this inefficiency is to automatically identify and process only those mesh faces that lie within a small region of specified volume around the photon's location. For this purpose, a spatial partitioning algorithm, similar to some previously described, is currently being developed to improve the MC simulation speed for complex mesh geometries [79].

Figure 4.2 shows validations of the MATLAB MC code against the lab's existing C MC code for time-resolved fluorescence at various source-detector separations. For this validation study, a bi-layered tissue model with slab shaped meshes (containing 12 faces) was employed to mimic the geometry of the C code. This geometry was employed to validate the ability of the MATLAB code to accurately process a user-defined mesh surface and use this surface to check for interface crossings.

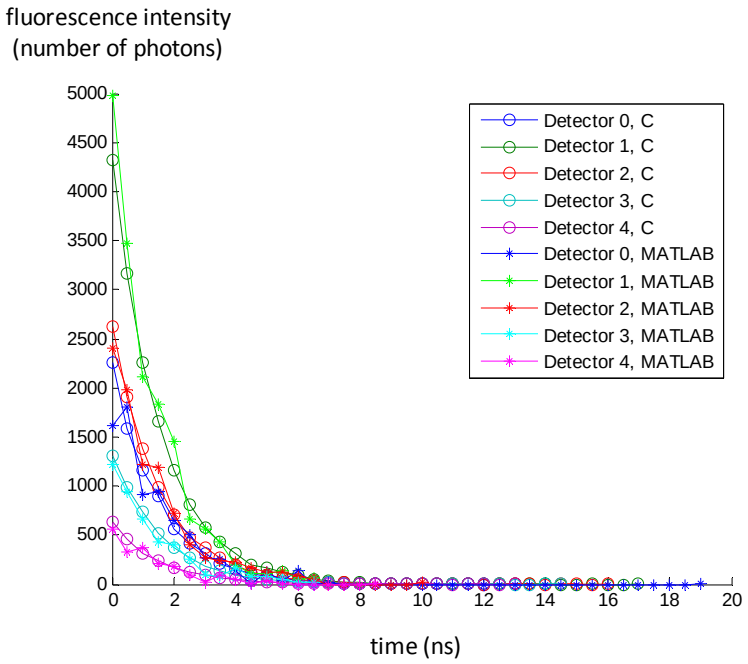

Figure 4.2 Time-resolved fluorescence simulated by mesh-surface MATLAB MC code (stars) versus that generated from previously-validated MC code in C (circles), for a layered slab-mesh tissue geometry [203]. Detector 0 was the source fiber (400 µm diameter); detectors 1-4 were rings of increasing radii, comprised of identical 400 µm fibers.

The thickness of the top layer was 300 µm, and the bottom layer thickness could be approximated as infinite. The photon transport parameters used in the model were the absorption and scattering coefficients μ_{ai} and μ_{si} in each layer i of the tissue, as well as the anisotropy g (kept at a constant value of 0.9), and refractive index n (kept at a constant value of 1.4). These tissue properties were defined at both the excitation and fluorescence emission wavelengths. At the excitation wavelength, μ_{a1} (μ_{a2}) was set to 3.8 (0.5) cm^{-1} and μ_{s1} (μ_{s2}) was set to 487 (487) cm^{-1}. At the emission wavelength, μ_{a1} (μ_{a2}) was set to 2.5 (2.5) cm^{-1} and μ_{s1} (μ_{s2}) was set to 376 (376) cm^{-1}. The fluorescence parameters in the tissue model were the fluorescence absorption coefficient μ_{afx} (set to 1.2

cm^{-1} in layer 1 and 5.0 cm^{-1} in layer 2), quantum yield Φ_{QY} (set to 1.0 in each layer to improve photon statistics), and mean fluorescence lifetime $<t>$ (set to 1.5 ns in both layers). The values of these optical properties (except for Φ_{QY}) were chosen to be within a range expected for biological tissue.

Figure 4.2 shows that the MATLAB MC algorithm reproduced the time-resolved fluorescence curves from the previously-validated C code for a variety of source-detector separations, with a mean percent error of less than 6%. These results suggest that the MATLAB MC code has the potential to accurately model time-resolved fluorescence in tissue models defined by mesh surfaces.

We have developed a versatile, user-friendly MATLAB MC code to model time-resolved fluorescence in layered biological tissues containing an irregular interface defined by a mesh surface. To the best of our knowledge, this is the first demonstration of such an approach for time-resolved fluorescence MC coding that can accommodate arbitrarily-shaped tissue interfaces. The code should be useful for quantitative fluorescence lifetime sensing applications in complex biological tissues that require realistic computational models to account for effects caused by irregular interface geometry.

Now we describe the development and verification of a version of the aforementioned user-friendly, MATLAB-based Monte Carlo code that uses analytically-defined surface meshes to model heterogeneous tissue geometry [204]. The code can use information from non-linear optical microscopy images to discriminate the fluorescence photons

(from endogenous or exogenous fluorophores) detected from different layers of complex turbid media. We present a specific application of modeling a layered human tissue-engineered construct (*Ex Vivo* Produced Oral Mucosa Equivalent, EVPOME) designed for use in repair of oral tissue following surgery. Second-harmonic generation microscopic imaging of an EVPOME construct (oral keratinocytes atop a scaffold coated with human type IV collagen) was employed to determine an approximate analytical expression for the complex shape of the interface between the two layers. This expression can then be inserted into the code to correct the simulated fluorescence for the effect of the irregular tissue geometry.

Fluorescence spectroscopy is frequently employed for tissue sensing because it has the potential to provide quantitative information about the relative contributions of native tissue fluorophores (such as collagen, NADH, and FAD) to the detected signal [3, 7, 10, 205]. However, the detected fluorescence signal can often be distorted by tissue absorption and scattering. Monte Carlo (MC) simulations, the current gold standard for describing photon propagation in turbid media, are often employed to quantitatively model tissue fluorescence in a manner that accounts for tissue geometry and attenuation from absorption and scattering [76, 77]. This problem becomes particularly challenging in tissue models with complex geometries [78, 79, 206, 207]. Here, we describe the development of a versatile Monte Carlo (MC) code that can use easily-interchangeable, analytically-defined surface meshes to predict the effect of absorption and scattering on the detected fluorescence from tissues with irregular geometries.

Fluorescence microscopy and spectroscopy are being investigated to assess the viability of a human tissue-engineered construct (*Ex Vivo* Produced Oral Mucosa Equivalent; EVPOME [208-210]) pre- and post-implantation. The EVPOME construct (histology image shown in Figure 4.3) consists of primary human oral keratinocytes atop a collagen-like scaffold. As the construct develops, the cells stratify and produce a top layer of non-viable cells containing cross-linked keratin. The goal of the fluorescence sensing techniques is to extract the redox ratio of the construct on various days of development and under different environmental conditions. To accomplish this goal, it is necessary to obtain the intrinsic fluorescence signals from the endogenous fluorophores NADH and FAD in the cellular layer of the construct [210]. However, the structure of the EVPOME poses a significant challenge, because the viable cellular layer is located between the keratin layer and scaffold, each of which has its own absorption, scattering, and fluorescence properties. Therefore, it is important to develop an accurate model of photon propagation in the EVPOME construct in order to quantify the effect of the optical properties of each layer on the detected fluorescence signal, and consequently, the detected redox ratio. Furthermore, as Figure 4.3 illustrates, the interface between the cell layer and scaffold is irregular in shape, so it is also important to develop a model that can quantitatively predict the effect of the construct geometry on the detected fluorescence.

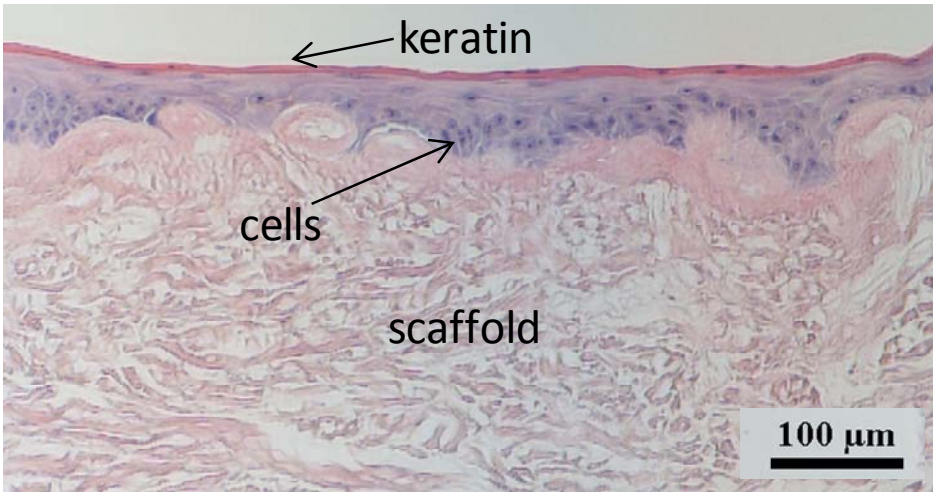

Figure 4.3 Histology image of an *Ex Vivo* Produced Oral Mucosa Equivalent (EVPOME) construct, comprised of scaffold (bottom layer, stained light pink), cells (middle layer, stained purple), and keratin-containing non-viable cell layer (top layer, stained dark pink) [204]. The interface between the cellular layer and the scaffold is noticeably irregular in shape.

Non-linear optical microscopy images of EVPOME constructs were acquired using an 880 nm femtosecond-pulsed laser source coupled to an inverted microscope (Leica) with a 25x water objective. Second-harmonic generation (SHG) cross-sectional (*x*-*z*) images were obtained at 420-460 nm emission (to detect collagen). From this data, the interface between the cells and the scaffold could be approximated as a sinusoid (Figure 4.4). The period and amplitude of the interface were estimated from Figure 4.4 to be 235 µm and 20 µm, respectively. This data was then employed to generate a three-dimensional surface mesh of the interface between the stratified cellular layer and scaffold of the EVPOME construct (Figure 4.5).

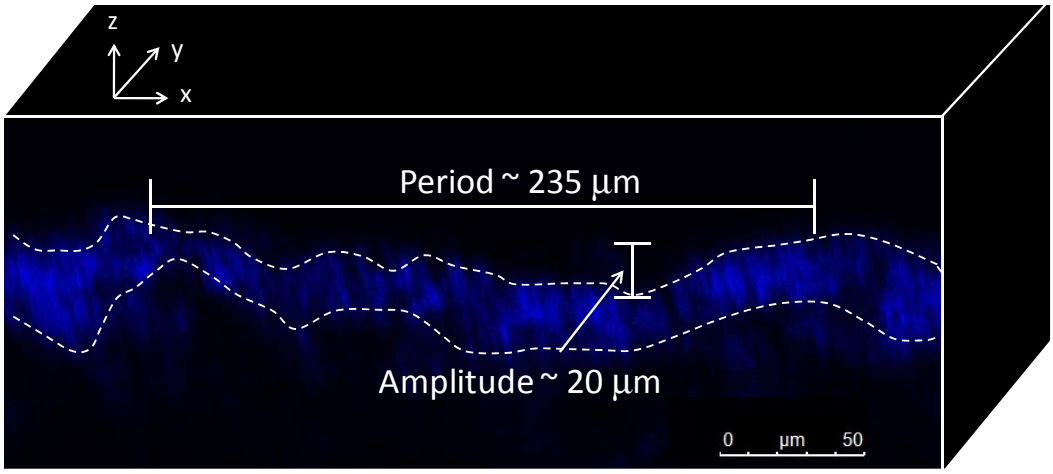

Figure 4.4 Second-harmonic generation cross-sectional image of the scaffold of an EVPOME construct acquired with non-linear optical microscopy and overlaid onto a three-dimensional schematic of a tissue [204]. The interface between the stratified cellular layer and scaffold can be approximated as a sinusoid with amplitude 20 µm and period 235 µm.

To simulate photon propagation in complex tissues, the pre-existing MC code was translated to MATLAB and the geometry of each layer was re-defined as a surface mesh. The MATLAB programming language is intuitive and widely used in science and engineering, so the code can be easily modified to change the source-detector configuration, tissue optical properties, and tissue geometry [203]. Each interface can be analytically defined as an expression for the depth as a function of the other two spatial coordinates: $z(x,y)$. An example of this feature, for the equation corresponding to the cell-scaffold interface in an EVPOME construct (Figure 4.4), is shown in Figure 4.5. For more complicated surfaces that are not easily represented by analytical functions, the meshes can be imported from external data sources such as CT or MRI images.

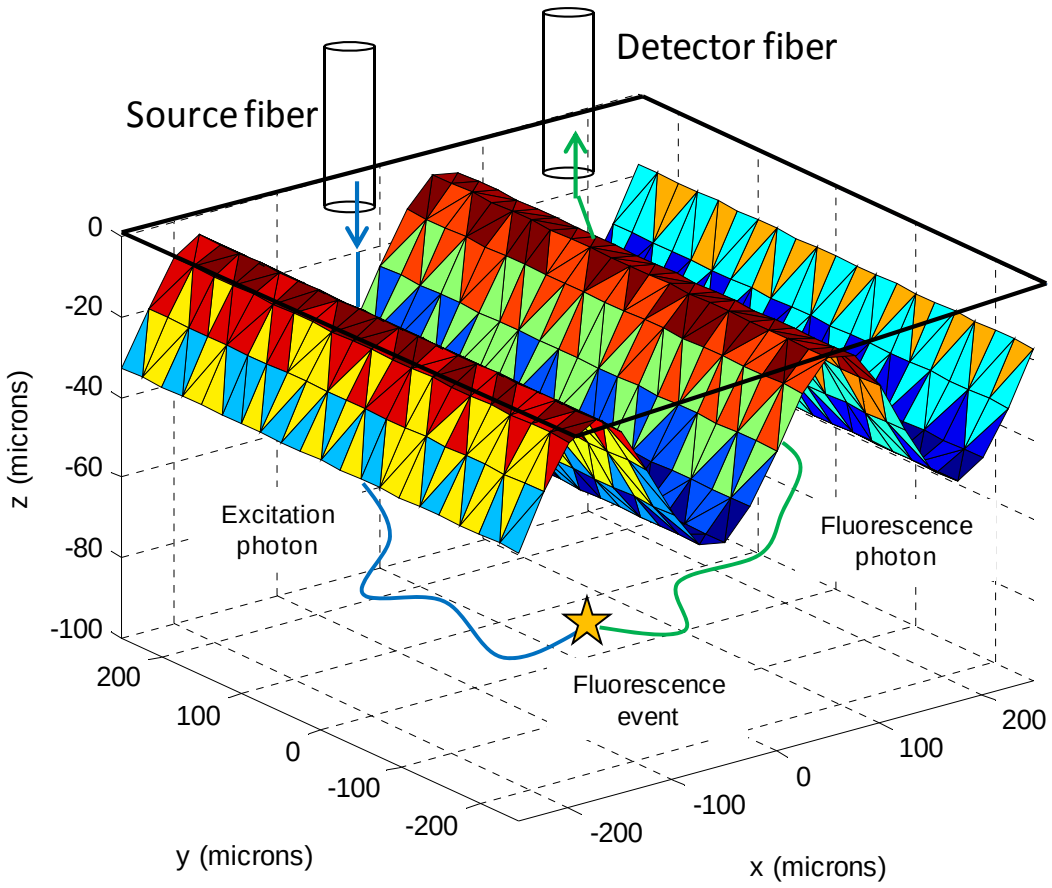

Figure 4.5 Surface mesh employed to model the interface between the cellular layer and scaffold in an EVPOME construct [204]. The equation of the irregular surface (based on the image in Figure 4.4) was $z(x) = 20\sin(2\pi x/235) - 25$. Excitation light (blue) enters the tissue from the source optical fiber, and detected fluorescence (green) arrives back at the surface.

A flow chart of code inputs and outputs illustrating the differences between the mesh-based MATLAB MC code and the previously-developed slab-based MC code is shown in Figure 4.6.

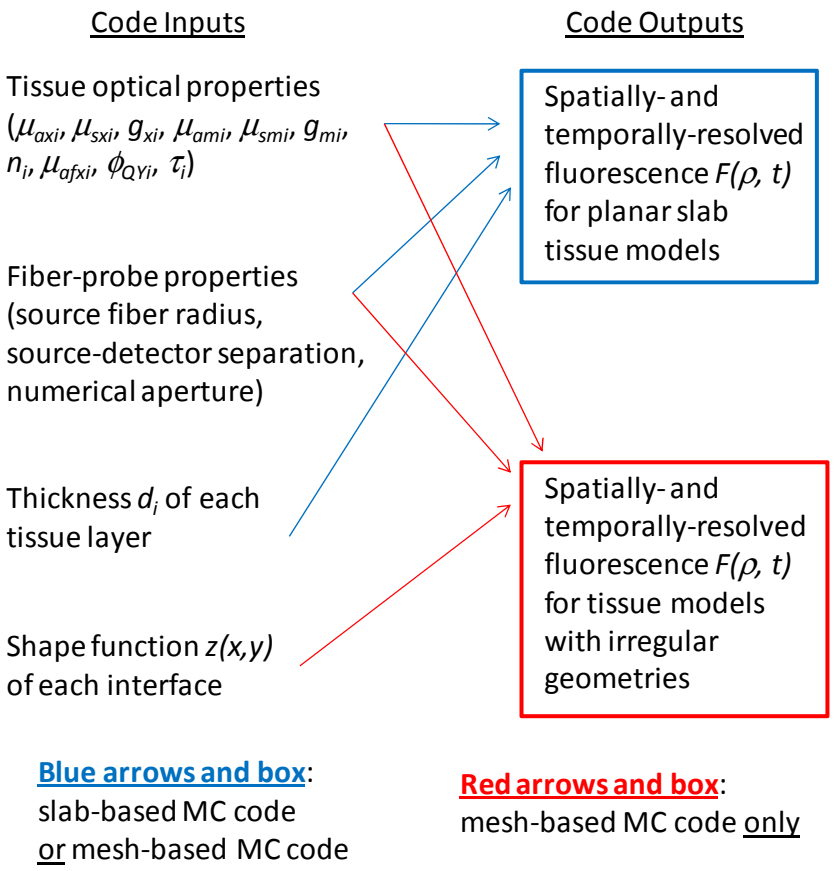

Figure 4.6. Chart of inputs and outputs for slab-based Monte Carlo code (blue arrows and box) and mesh-based Monte Carlo code (red arrows and box) [204]. Both codes predict the spatially- and temporally-resolved fluorescence $F(\rho,t)$, but the mesh-based code can generate this information for tissue models with irregular geometries as well as layered slab models. The subscript x (m) denotes the excitation (emission) wavelength, and the subscript i denotes the tissue layer. Both codes can also model multiple fluorophores in each tissue layer.

Both codes require the same set of tissue optical properties and fiber probe properties: namely, the tissue absorption coefficients (μ_{axi}, μ_{ami}), scattering coefficients (μ_{sxi}, μ_{smi}), and anisotropy values (g_{xi}, g_{mi}) at the excitation and emission wavelengths, the refractive

index n_i of each tissue layer, the fluorophore absorption coefficients μ_{afxi}, the fluorophore lifetimes τ_i, and the fluorophore quantum yields ϕ_{QYi}. The subscript x (m) denotes the excitation (emission) wavelength, and the subscript i denotes the tissue layer. Both codes can also model multiple fluorophores in each tissue layer.

The slab-based code requires the thickness of each individual (planar) tissue layer, while the mesh-based code takes a general shape function $z(x,y)$ as its input for the geometry of each tissue interface. Both codes generate the spatially- and temporally-resolved tissue fluorescence $F(\rho,t)$, but the mesh-based code can provide this information for tissue models with non-planar interfaces.

To validate the analytical mesh-based MC code, a bi-layered slab model was created in MATLAB (where the two interfaces were defined analytically (as $z(x,y) = 0$ and $z(x,y) =$ 250 μm) according to a procedure that could be extended to more complex surfaces. The spatially-resolved fluorescence from the MATLAB MC code was compared to that from a previously-validated MC code [76, 77] written in C for tissue models approximated as stacks of homogeneous slabs. The scattering coefficients used in the validation were: μ_{sx1} = 120 cm^{-1}, μ_{sx2} = 100 cm^{-1}, μ_{sm1} =80 cm^{-1}, μ_{sm2} = 70 cm^{-1}. The other optical properties were constant for both layers and both wavelengths: the absorption coefficient μ_a was set equal to 0.1 cm^{-1} everywhere, and the anisotropy g was set to a constant value of 0.9. Photons were launched with a 600 μm diameter fiber and detected by rings of 600 μm thickness. Validation results are shown in Figure 4.7 (linear scale) and Figure 4.8

(logarithmic scale). The mean difference in simulated fluorescence between the two codes was less than 6%.

The results suggest that the mesh-based MATLAB MC code has the potential to accurately simulate fluorescence in complex layered tissues where the interfaces between layers are defined analytically with surface meshes. This code provides a user-friendly framework for simulations of photon propagation, allowing for rapid variation of tissue interface geometry by interchanging analytical expressions in small subsections of the code. The mesh-based MC code can potentially be integrated with tissue morphology information from non-linear optical microscopy images to discriminate the detected fluorescence from different spatial locations within complex layered turbid media. This code can also potentially be employed to model inelastic (Raman) scattering in layered tissue models with irregular geometries, allowing for predictions of detected Raman signal as a function of source and detector position [169, 192].

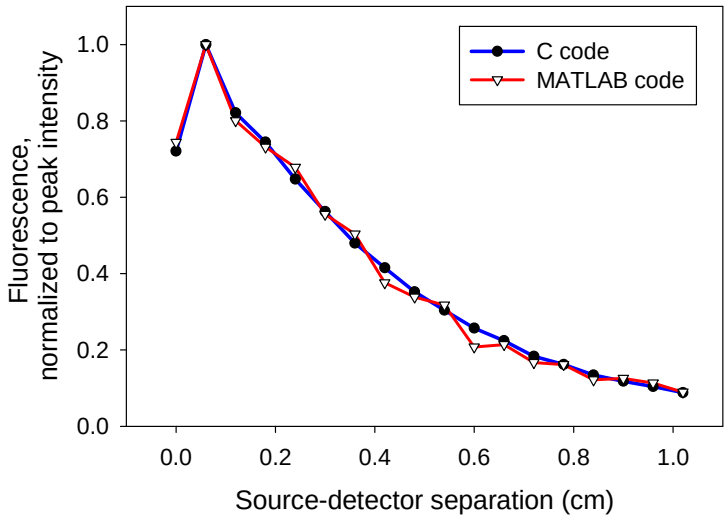

Figure 4.7 Comparison of plane-mesh MATLAB code (red line, triangles) with slab-based C code (blue line, circles) for spatially resolved fluorescence on a linear scale [204]. The mean percent difference between the two codes was less than 6%.

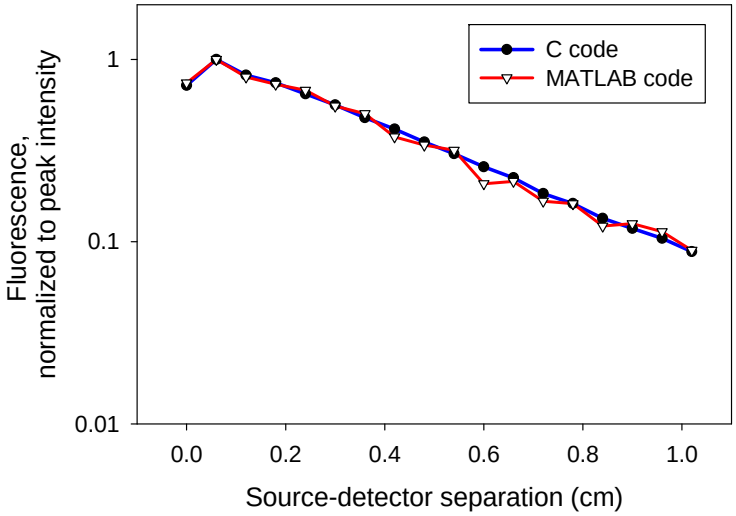

Figure 4.8 Comparison of plane-mesh MATLAB code (red line, triangles) with slab-based C code (blue line, circles) for spatially-resolved fluorescence on a logarithmic scale. The mean percent difference between the two codes was less than 6% [204].

Chapter 5

Discussion and conclusions

5.1. Major contributions of this dissertation

The work presented in this dissertation describes the development and application of DA, MC, and semi-empirical models to analyze reflectance, fluorescence, and Raman spectroscopy data from human tissues for tissue sensing and disease diagnostics. The tissue properties extracted by these models were often shown to be different for normal and diseased tissue, thereby illustrating the potential of optical spectroscopy to enable quantitative diagnostics in a wide range of human tissues. The work described in this dissertation focuses on the potential of three different types of mathematical models (diffusion theory, Monte Carlo simulations, and semi-empirical models) to accurately analyze measured reflectance and fluorescence spectra from human tissues. When fit to measured spectral data, the models have the capability to extract parameters related to tissue composition, vasculature, morphology, and metabolic function. These parameters can then be employed to distinguish between normal and diseased human tissues, thereby suggesting that optical spectroscopy has the potential to help improve human disease diagnostics.

The major contributions of this dissertation can be summarized as follows:

Chapter 2

- We developed the first-ever photon-tissue interaction (PTI) model of reflectance and fluorescence from human pancreatic tissue. We employed this model to extract biophysically-relevant tissue parameters from reflectance and fluorescence spectra of human pancreatic tissues for the first time.
- We employed the PTI model to obtain the first-ever values of the optical absorption and scattering coefficients of normal and diseased (pancreatitis, adenocarcinoma) human pancreatic tissues.
- We performed the first-ever comparison between results of the PTI model and those of histopathology, the diagnostic gold-standard. We showed for the first time that changes in PTI model parameters were consistent with those observed at histology.
- We fit the PTI model to individual reflectance and fluorescence measurements to extract biophysically-relevant parameters from individual tissue sites for the first time and demonstrate the statistical significance of these parameters.
- We incorporated the PTI parameters into a novel tissue classification algorithm that employed Generalized Estimating Equations to account for correlations in the data. The algorithm was able to accurately distinguish adenocarcinoma from the non-malignant tissue types (normal and pancreatitis).

Chapter 3

- We developed the first-ever Monte Carlo model of Raman scattering in a multi-layered model of human bone tissue to examine the effect of tissue and probe properties on the detected Raman signal.

- We developed the first-ever Monte Carlo model of Raman scattering in a multi-layered model of human breast tissue to examine the effect of tissue and probe properties on the detected Raman signal.
- We validated the predictions of spatially-resolved Raman signal for the novel layered Monte Carlo model against experimental data acquired from bi-layered tissue phantoms consisting of normal and cancerous human breast tissue.
- We employed the novel layered Monte Carlo model to optimize and characterize the design of a fiber-optic Raman spectroscopy probe for accurate detection of breast tumor margins following surgery.

Chapter 4

- We developed novel user-friendly, versatile, MATLAB-based models of steady-state and time-resolved fluorescence from tissue models with irregular geometries.

The work in this dissertation has been presented and documented as cited below:

Journal articles and manuscripts in preparation:

Chapter 1

- R. H. Wilson and M.-A. Mycek, "Models of light propagation in human tissue applied to cancer diagnostics," *Technology in Cancer Research and Treatment* **10**, 121, 2011 (14 pages).
- W. R. Lloyd, R. H. Wilson, C.-W. Chang, G. D. Gillispie, and M.-A. Mycek, "Instrumentation to rapidly acquire fluorescence wavelength-time matrices of biological tissues," *Biomedical Optics Express* **1**, 574, 2010 (13 pages).

Chapter 2

- R. H. Wilson, M. Chandra, L.-C. Chen, W. Lloyd, J. Scheiman, D. Simeone, J. Purdy, B. McKenna, and M.-A. Mycek, "Photon-tissue interaction model enables quantitative optical analysis of human pancreatic tissues," *Optics Express* **18**, 21612, 2010 (10 pages).
- R. H. Wilson, M. Chandra, J. Scheiman, D. Simeone, B. McKenna, J. Purdy, and M.-A. Mycek, "Optical spectroscopy detects histological hallmarks of pancreatic cancer," *Optics Express* **17**, 17502, 2009 (15 pages).
- R. H. Wilson, M. Chandra, L.-C. Chen, W. Lloyd, J. Scheiman, D. Simeone, B. McKenna, and M.-A. Mycek, "Photon-tissue interaction model consistently distinguishes optical characteristics of human pancreatic disease," manuscript in preparation.
- R. H. Wilson*, M. Chandra*, J. Scheiman, O. E. Lee, B. McKenna, D. Simeone, J. M. G. Taylor, and M.-A. Mycek, "Optical spectroscopy distinguishes pancreatic cancer from non-malignant pancreatic tissues," manuscript in preparation. (*Equal contribution to authorship)

Chapter 3

- M. D. Keller, E. Vargis, N. de Matos Granja, R. H. Wilson, M.-A. Mycek, M. C. Kelley, and A. Mahadevan-Jansen, "Development of a spatially offset Raman spectroscopy probe for breast tumor surgical margin evaluation," *Journal of Biomedical Optics* **16**, 077006, 2011 (8 pages).
- M. D. Keller*, R. H. Wilson*, M.-A. Mycek, and A. Mahadevan-Jansen, "Monte Carlo model of spatially offset Raman spectroscopy for breast tumor margin

analysis," *Applied Spectroscopy* **64**, 607, 2010 (8 pages). (*Equal contribution to authorship)

- M. Raghavan, N. D. Sahar, R. H. Wilson, M.-A. Mycek, N. Pleshko, D. H. Kohn, and M. D. Morris, "Quantitative polarized Raman spectroscopy in highly turbid bone tissue," *Journal of Biomedical Optics* **15**, 037001, 2010 (7 pages).

Conference proceedings:

Chapter 1

- W. R. Lloyd, R. H. Wilson, L.-C. Chen, G. D. Gillispie, and M.-A. Mycek, "Fluorescence wavelength-time matrix acquisition for biomedical tissue diagnostics," *Clinical and Biomedical Spectroscopy and Imaging II*, Nirmala Ramanujam, Jürgen Popp, Editors, Proc. SPIE Int. Soc. Opt. Eng. 8087, 80870Y, 2011 (7 pages).
- C.-W. Chang, W. Lloyd, R. Wilson, G. D. Gillispie, and M.-A. Mycek, "Clinically compatible instrumentation for accurate detection of fluorescence intensity and lifetime in turbid media," *Advanced Biomedical and Clinical Diagnostic Systems VIII*, Tuan Vo-Dinh, Warren S. Grundfest, Anita Mahadevan-Jansen, Editors, Proc. SPIE Int. Soc. Opt. Eng. 7555, 755503, 2010 (6 pages).
- R. H. Wilson, K. Vishwanath, and M.-A. Mycek, "Combined Monte Carlo and path-integral method for simulated library of time-resolved reflectance curves from layered tissue models," *Optical Interactions with Tissues and Cells XX*, Steven L. Jacques, E. Duco Jansen, William P. Roach, Editors, Proc. SPIE Int. Soc. Opt. Eng. 7175, 717518, 2009 (9 pages).

- R. H. Wilson, K. Vishwanath, and M.-A. Mycek, "Semi-analytical method for rapid simulation of time-resolved reflectance in layered epithelial tissues," in *Frontiers in Optics 2008, OSA Technical Digest* (Optical Society of America), FTuK3 (1 page).
- R. H. Wilson, K. Vishwanath, and M.-A. Mycek, "Semi-analytical method for rapid calculation of time-resolved reflectance from bi-layered tissue models," *Diagnostic Optical Spectroscopy in Biomedicine IV*, Dietrich Schweitzer, Maryann Fitzmaurice, Editors, Proc. SPIE Int. Soc. Opt. Eng. 6628, 66280W, 2007 (10 pages).
- R. H. Wilson, K. Vishwanath, and M.-A. Mycek, "Time-resolved reflectance of two-layered tissue models via scaling of 'white' Monte Carlo simulations," in *Biomedical Optics 2006 Technical Digest* (Optical Society of America), ME1 (3 pages).

Chapter 2

- R. H. Wilson, M. Chandra, W. Lloyd, L.-C. Chen, J. Scheiman, D. Simeone, B. McKenna, and M.-A. Mycek, "Optical spectroscopy for quantitative sensing in human pancreatic tissues," *Clinical and Biomedical Spectroscopy and Imaging II*, Nirmala Ramanujam, Jürgen Popp, Editors, Proc. SPIE Int. Soc. Opt. Eng. 8087, 808713, 2011 (7 pages).
- R. H. Wilson, M. Chandra, W. R. Lloyd, J. Scheiman, D. Simeone, J. Purdy, B. McKenna, and M.-A. Mycek, "Quantitative optical spectroscopy for pancreatic cancer detection," in *Biomedical Optics 2010 Technical Digest* (Optical Society of America), BWB6 (3 pages).
- M. Chandra, R. H. Wilson, J. Scheiman, D. Simeone, B. McKenna, J. Purdy, and M.-A. Mycek, "Optical spectroscopy for clinical detection of pancreatic cancer," *Clinical*

and Biomedical Spectroscopy, Irene Georgakoudi, Jürgen Popp, Katarina Svanberg, Editors, Proc. SPIE. Int. Soc. Opt. Eng. 7368, 73681G, 2009 (6 pages).

- R. H. Wilson. M. Chandra, J. Scheiman, D. Simeone, B. McKenna, J. Purdy, and M.-A. Mycek, "Mathematical modeling of reflectance and intrinsic fluorescence for cancer detection in human pancreatic tissue," *Biomedical Applications of Light Scattering III*, Adam Wax, Vadim Backman, Editors, Proc. SPIE Int. Soc. Opt. Eng. 7187, 71870H, 2009 (9 pages).
- R. H. Wilson, M. Chandra, J. Scheiman, D. Heidt, D. Simeone, B. McKenna, and M.-A. Mycek, "Modeling reflectance and fluorescence spectra of human pancreatic tissues for cancer diagnostics," in *Frontiers in Optics 2008, OSA Technical Digest* (Optical Society of America), FTuK5 (1 page).

Chapter 3

- M. Raghavan, N. D. Sahar, R. H. Wilson, M.-A. Mycek, N. Pleshko, D. H. Kohn, and M. D. Morris, "Polarized Raman spectroscopy of bone tissue: watch the scattering," *Photonic Therapeutics and Diagnostics VI*, Nikiforos Kollias, Bernard Choi, Haishan Zeng, Reza S. Malek, Brian J. Wong, Justus F. R. Ilgner, Kenton W. Gregory, Guillermo J. Tearney, Laura Marcu, Henry Hirschberg, Steen J. Madsen, Andreas Mandelis, Anita Mahadevan-Jansen, E. Duco Jansen, Editors, Proc. SPIE Int. Soc. Opt. Eng. 7548, 754848, 2010 (5 pages).
- R. H. Wilson, K. A. Dooley, M. D. Morris, and M.-A. Mycek, "Monte Carlo modeling of photon transport in buried bone tissue layer for quantitative Raman spectroscopy," *Optics in Bone Biology and Diagnostics*, Andreas Mandelis, Editor, Proc. SPIE Int. Soc. Opt. Eng. 7166, 716604, 2009 (10 pages).

- R. H. Wilson, M. D. Morris, and M.-A. Mycek, "Monte Carlo simulations of Raman scattering from bone within a multi-layered tissue model," in *Frontiers in Optics 2008, OSA Technical Digest* (Optical Society of America), FTuK2 (1 page).

Chapter 4

- R. H. Wilson, L.-C. Chen, W. Lloyd, S. Kuo, C. Marcelo, S. E. Feinberg, and M.-A. Mycek, "Mesh-based Monte Carlo code for fluorescence modeling in complex tissues with irregular boundaries," *Novel Biophotonic Techniques and Applications*, Henricus J. C. M. Sterenborg, I. Alex Vitkin, Editors, Proc. SPIE Int. Soc. Opt. Eng. 8090, 80900E, 2011 (7 pages).
- L.-C. Chen, W. R. Lloyd, R. H. Wilson, S. Kuo, C. L. Marcelo, S. E. Feinberg, and M.-A. Mycek, "Nonlinear optical molecular imaging enables metabolic redox sensing in tissue-engineered constructs," *Molecular Imaging III*, Charles P. Lin, Vasilis Ntziachristos, Editors, Proc. SPIE Int. Soc. Opt. Eng. 8089, 80890J, 2011 (7 pages).
- V. Schweller*, R. H. Wilson*, and M.-A. Mycek, "User-friendly Monte Carlo code for time-resolved fluorescence models of tissues with irregular interfaces," in *Biomedical Optics 2010 Technical Digest* (Optical Society of America), BME8 (3 pages). (*Equal contribution to authorship)
- R. H. Wilson, M. Chandra, W.-L. Lo, K. Vishwanath, K. Izumi, S. E. Feinberg, and M.-A. Mycek, "Simulated fiber-optic interrogation of autofluorescence from superficial layer of tissue-engineered construct," in *Frontiers in Optics 2008, OSA Technical Digest* (Optical Society of America), FTuK6 (1 page).

- M. Chandra, R. H. Wilson, W.-L. Lo, K. Vishwanath, K. Izumi, S. E. Feinberg, and M.-A. Mycek, "Sensing metabolic activity in tissue-engineered constructs," *Diagnostic Optical Spectroscopy in Biomedicine IV*, Dietrich Schweitzer, Maryann Fitzmaurice, Editors, Proc. SPIE Int. Soc. Opt. Eng. 6628, 66280B, 2007 (7 pages).

Note: The appropriate permissions have been obtained for the inclusion of previously published material in this dissertation.

Note: In between the publication of the 2009 and 2010 Optics Express articles included in Chapter 2, several errors in the pancreatic data analysis procedure were caught and fixed. These errors were not expected to change the main conclusions of Section 2.1.

5.2 Future work

Including time-resolved fluorescence data in pancreatic tissue classification algorithms

In addition to the steady-state reflectance and fluorescence data described in Chapter 2, time-resolved data was obtained from each pancreatic tissue site. We have employed a variety of mathematical models to analyze the time-resolved data, and the extracted parameters have been incorporated into tissue classification algorithms. A systematic evaluation of the effect of these time-resolved parameters on the classification power of the algorithms is underway, and the following manuscript is in preparation:

R. H. Wilson*, M. Chandra*, J. Scheiman, D. Simeone, B. McKenna, W. Lloyd, L.-C. Chen, O. E. Lee, J. M. G. Taylor, and M.-A. Mycek, "Combined steady-state and time-

resolved optical spectroscopy improves pancreatic disease diagnostics" (in preparation). (*equal contribution to authorship)

Unified model of steady-state and time-resolved fluorescence

For each individual pancreatic tissue site, there should be equivalence between the information extracted from the steady-state fluorescence data and the time-resolved fluorescence data. A study is underway to compare the percentage contributions of endogenous tissue fluorophores extracted by the PTI model of steady-state fluorescence with the contributions of each component extracted from the different models of time-resolved fluorescence.

Using photon-tissue interaction model to distinguish other pancreatic tissue types

In addition to the optical spectra of normal pancreatic tissue, pancreatitis, and adenocarcinoma sites described in Chapter 2, reflectance and fluorescence measurements were also performed on pre-cancerous tissues (pancreatic intraepithelial neoplasia and intraductal papillary mucinous neoplasm) and benign tumors (serous cystadenoma). A study is in progress to determine whether parameters from the data analysis methods described in Chapter 2 can be employed to accurately distinguish pre-cancers from normal pancreatic tissue and pancreatitis, and to accurately distinguish benign tumors from malignant tumors.

Using photon-tissue interaction model to analyze pancreatic optical spectra acquired in vivo

We have begun an IRB-approved study to acquire reflectance and fluorescence data from human pancreatic tissues *in vivo* during pancreatic surgery. Work is underway to employ

the photon-tissue interaction (PTI) model described in Chapter 2 to analyze the *in vivo* data and compare the extracted parameters with those obtained from spectra measured *ex vivo* from the same tissue sites. This analysis will also include a more detailed quantitative investigation of how the PTI model describes the effect of changing the properties of the fiber-optic probe, since the geometry of the *in vivo* fiber-probe is different than that of the probe used in the *ex vivo* study described in Chapter 2. This work will help us to determine whether the PTI model needs to be modified for analysis of *in vivo* data.

Quantitative image analysis of pancreatic tissue histology

A study is underway to employ image analysis software for more detailed quantitative analysis of the histology images obtained from the pancreatic tissue sites measured in the study described in Chapter 2. Quantitative information about the distribution of sizes of cell nuclei, collagen content, and other morphological features of the tissue, obtained from systematic image analysis, can potentially be employed to verify or improve components of the PTI model described in Chapter 2.

Bone and breast tissue characterization with Raman spectroscopy

Work is underway to employ the irregular-interface Monte Carlo models described in Chapter 4 for more accurate simulation of Raman scattering in bone. The Raman models described in Chapter 3 assumed that each tissue layer was flat, but for bone and the overlying tissues, the geometry is closer to cylindrical. Monte Carlo codes for more realistic tissue geometries (such as nested cylinders) have been written in MATLAB for more accurate description of the effect of tissue geometry on the detected Raman signal.

A comprehensive verification of these codes against pre-existing analytical and computational models is in progress, and experimental validation of these codes against measured data from tissue-simulating phantoms is also underway.

Monte Carlo models for tissues with irregular interfaces

In addition to the verification and validation studies described previously, work is underway to develop semi-analytical "scaling" methods to decrease the computation time required for simulation of spatially- and temporally-resolved photon propagation from a set of tissues with different optical and geometrical properties. These methods involve the use of path-integral models of photon transport in turbid media to obtain analytical equations for the average classical path of a photon in each tissue model of interest. The path-integral models can also be employed to visualize the distribution of photons within biological tissues for varying optical properties and fiber-probe geometries. The following manuscript is in preparation:

R. H. Wilson and M.-A. Mycek, "Path-integral method for rapid, closed-form description of photon migration in layered biological tissues" (in preparation).

Funding Acknowledgements

Chapter 1

This work was supported in part by funding from The Wallace H. Coulter Foundation and the National Institutes of Health (NIH-CA-114542).

Chapter 2

This work was supported in part by the Wallace H. Coulter Foundation, the National Pancreas Foundation, the U of M Comprehensive Cancer Center, a grant from the U of M Medical School Translational Research Program, and the National Institutes of Health (NIH-CA-114542, NIH T32 CA083654).

Chapter 3

This work is supported in part via grants from the National Institutes of Health (AR055222-02, NIH CA-114542). The authors acknowledge the financial support of the Department of Defense Breast Cancer Research Program Idea Award #W81XWH-09-1-0037, a DOD BCRP predoctoral fellowship, and a Vanderbilt University Graduate School dissertation enhancement grant to support travel between universities.

Chapter 4

This work was supported in part by the National Institutes of Health (NIH R01-DE-019431, NIH R01-AR-055222).

References

1. A. J. Welch and M. J. C. van Gemert, eds., *Optical-Thermal Response of Laser-Irradiated Tissue* (Plenum Press, New York, 1995).

2. M.-A. Mycek and B. W. Pogue, eds., *Handbook of Biomedical Fluorescence* (Marcel Dekker, Inc., New York, 2003).

3. R. H. Wilson and M.-A. Mycek, "Models of light propagation in human tissue applied to cancer diagnostics," Technol. Cancer Res. Treat. **10**, 121-134 (2011).

4. J. Q. Brown, K. Vishwanath, G. M. Palmer, and N. Ramanujam, "Advances in quantitative UV-visible spectroscopy for clinical and pre-clinical application in cancer," Curr. Opin. Biotechnol. **20**, 119-131 (2009).

5. G. Zonios, L. T. Perelman, V. Backman, R. Manoharan, M. Fitzmaurice, J. V. Dam, and M. S. Feld, "Diffuse reflectance spectroscopy of human adenomatous colon polyps *in vivo*," Appl. Opt. **38**, 6628-6637 (1999).

6. I. Georgakoudi and M. S. Feld, "The combined use of fluorescence, reflectance, and light-scattering spectroscopy for evaluating dysplasia in Barrett's esophagus," Gastrointest. Endosc. Clin. N. Am. **14**, 519-537 (2004).

7. S. K. Chang, N. Marin, M. Follen, and R. Richards-Kortum, "Model-based analysis of clinical fluorescence spectroscopy for *in vivo* detection of cervical intraepithelial dysplasia," J. Biomed. Opt. **11**, 024008 (2006).

8. C. Zhu, G. M. Palmer, T. M. Breslin, J. Harter, and N. Ramanujam, "Diagnosis of breast cancer using fluorescence and diffuse reflectance spectroscopy: a Monte-Carlo-model-based approach," J. Biomed. Opt. **13**, 034015 (2008).

9. Z. Volynskaya, A. S. Haka, K. L. Bechtel, M. Fitzmaurice, R. Shenk, N. Wang, J. Nazemi, R. R. Dasari, and M. S. Feld, "Diagnosing breast cancer using diffuse reflectance spectroscopy and intrinsic fluorescence spectroscopy," J. Biomed. Opt. **13**, 024012 (2008).

10. R. H. Wilson, M. Chandra, L.-C. Chen, W. Lloyd, J. Scheiman, D. Simeone, J. Purdy, B. McKenna, and M.-A. Mycek, "Photon-tissue interaction model enables quantitative optical analysis of human pancreatic tissues," Opt. Express **18**, 21612-21621 (2010).

11. R. R. Alfano, G. C. Tang, A. Pradhan, W. Lam, D. S. J. Choy, and E. Opher, "Fluorescence spectra from cancerous and normal human breast and lung tissues," IEEE J. Quantum Electron. **23**, 1806-1811 (1987).

12. G. C. Tang, A. Pradhan, and R. Alfano, "Spectroscopic differences between human cancer and normal lung and breast tissues," Lasers Surg. Med. **9**, 290-295 (1989).

13. R. R. Alfano, B. B. Das, J. Cleary, R. Prudente, and E. J. Celmer, "Light sheds light on cancer - distinguishing malignant tumors from benign tissues and tumors," Bull. N. Y. Acad. Med. **67**, 143-150 (1991).

14. C.-H. Liu, B. B. Das, W. L. Sha Glassman, G. C. Tang, K. M. Yoo, H. R. Zhu, D. L. Akins, S. S. Lubicz, J. Cleary, R. Prudente, E. Celmer, A. Caron, and R. R. Alfano, "Raman, fluorescence, and time-resolved light scattering as optical diagnostic techniques to separate diseased and normal biomedical media," J. Photochem. Photobiol. B **16**, 187-209 (1992).

15. S. P. Schantz, V. Kolli, H. E. Savage, G. P. Yu, J. P. Shah, D. E. Harris, A. Katz, R. R. Alfano, and A. G. Huvos, "*In vivo* native cellular fluorescence and histological characteristics of head and neck cancer," Clin. Cancer Res. **4**, 1177-1182 (1998).

16. J. R. Mourant, I. J. Bigio, J. Boyer, R. L. Conn, T. Johnson, and T. Shimada, "Spectroscopic diagnosis of bladder cancer with elastic light scattering," Lasers Surg. Med. **17**, 350-357 (1995).

17. I. Bigio and J. Mourant, "Ultraviolet and visible spectroscopies for tissue diagnostics: fluorescence spectroscopy and elastic-scattering spectroscopy," Phys. Med. Biol. **42**, 803-814 (1997).

18. I. J. Bigio, S. G. Brown, G. Briggs, C. Kelley, S. Lakhani, D. Picard, P. M. Ripley, I. G. Rose, and C. Saunders, "Diagnosis of breast cancer using elastic-scattering spectroscopy: preliminary clinical results," J. Biomed. Opt. **5**, 221-228 (2000).

19. R. Cothren, R. Richards-Kortum, M. Sivak, M. Fitzmaurice, R. Rava, G. Boyce, M. Doxtader, R. Blackman, T. Ivanc, G. Hayes, M. Feld, and R. Petras, "Gastrointestinal tissue diagnosis by laser induced fluorescence spectroscopy at endoscopy," Gastrointest. Endosc. **36**, 105-111 (1990).

20. R. Cothren, M. Sivak, J. Van Dam, R. Petras, M. Fitzmaurice, and J. Crawford, "Detection of dysplasia at colonoscopy using laser-induced fluorescence: a blinded study," Gastrointest. Endosc. **44**, 168-176 (1996).

21. J. Dhingra, D. J. Perreault, K. McMillan, E. Rebeiz, S. Kabani, R. Manohran, I. Itzkan, M. Feld, and S. Shapshay, "Early diagnosis of upper aerodigestive tract cancer by autofluorescence," Arch. Otolaryngol. Head Neck Surg. **122**, 1181-1186 (1996).

22. D. R. Ingrams, J. K. Dhingra, K. Roy, D. F. Perrault, Jr., I. D. Bottrill, S. Kabani, E. E. Rebeiz, M. M. Pankratov, S. M. Shapshay, R. Manoharan, I. Itzkan, and M. S. Feld, "Autofluorescence characteristics of oral mucosa," Head Neck **19**, 27-32 (1997).

23. I. Georgakoudi, B. C. Jacobson, J. Van Dam, V. Backman, M. B. Wallace, M. G. Müller, Q. Zhang, K. Badizadegan, D. Sun, G. A. Thomas, L. T. Perelman, and M. S. Feld, "Fluorescence, reflectance, and light-scattering spectroscopy for

evaluating dysplasia in patients with Barrett's esophagus," Gastroenterology **120**, 1620-1629 (2001).

24. I. Georgakoudi, B. C. Jacobson, M. G. Müller, E. E. Sheets, K. Badizadegan, D. L. Carr-Locke, C. P. Crum, C. W. Boone, R. R. Dasari, J. Van Dam, and M. S. Feld, "NAD(P)H and collagen as *in vivo* quantitative fluorescent biomarkers of epithelial precancerous changes," Cancer Res. **62**, 682-687 (2002).

25. I. Georgakoudi, E. E. Sheets, M. G. Müller, V. Backman, C. P. Crum, K. Badizadegan, R. R. Dasari, and M. S. Feld, "Trimodal spectroscopy for the detection and characterization of cervical precancers *in vivo*," Am. J. Obstet. Gynecol. **186**, 374-382 (2002).

26. M. G. Müller, T. A. Valdez, I. Georgakoudi, V. Backman, C. Fuentes, S. Kabani, N. Laver, Z. Wang, C. W. Boone, R. R. Dasari, S. M. Shapshay, and M. S. Feld, "Spectroscopic detection and evaluation of morphologic and biochemical changes in early human oral carcinoma," Cancer **97**, 1681-1692 (2003).

27. N. Bedard, M. Pierce, A. El-Naggar, S. Anandasabapathy, A. Gillenwater, and R. Richards-Kortum, "Emerging roles for multimodal optical imaging in early cancer detection: a global challenge," Technol. Cancer Res. Treat. **9**, 211-218 (2010).

28. M. Chandra, J. Scheiman, D. Heidt, D. Simeone, B. McKenna, and M.-A. Mycek, "Probing pancreatic disease using tissue optical spectroscopy," J. Biomed. Opt. **12**, 060501 (2007).

29. U. Utzinger and R. Richards-Kortum, "Fiber optic probes for biomedical optical spectroscopy," J. Biomed. Opt. **8**, 121-147 (2003).

30. H.-W. Wang, J.-K. Jiang, C.-H. Lin, J.-K. Lin, G.-J. Huang, and J.-S. Yu, "Diffuse reflectance spectroscopy detects increased hemoglobin concentration and decreased oxygenation during colon carcinogenesis from normal to malignant tumors," Opt. Express **17**, 2805–2817 (2009).

31. G. Zonios, A. Dimou, I. Bassukas, D. Galaris, A. Tsolakidis, and E. Kaxiras, "Melanin absorption spectroscopy: new method for noninvasive skin investigation and melanoma detection," J. Biomed. Opt. **13**, 014017 (2008).

32. R. H. Wilson, M. Chandra, J. Scheiman, D. Simeone, B. McKenna, J. Purdy, and M. A. Mycek, "Optical spectroscopy detects histological hallmarks of pancreatic cancer," Opt. Express **17**, 17502-17516 (2009).

33. I. S. Saidi, S. L. Jacques, and F. K. Tittel, "Mie and Rayleigh modeling of visible-light scattering in neonatal skin," Appl. Optics **34**, 7410-7418 (1995).

34. J. R. Lakowicz, *Principles of Fluorescence Spectroscopy* (Kluwer Academic/Plenum, New York, 1999).

35. S. K. Chang, Y. N. Mirabal, E. N. Atkinson, D. Cox, A. Malpica, M. Follen, and R. Richards-Kortum, "Combined reflectance and fluorescence spectroscopy for *in vivo* detection of cervical pre-cancer," J. Biomed. Opt. **10**, 024031 (2005).

36. M.-A. Mycek, K. Schomacker, and N. Nishioka, "Colonic polyp differentiation using time resolved autofluorescence spectroscopy," Gastrointest. Endosc. **48**, 390-394 (1998).

37. K. Vishwanath and M.-A. Mycek, "Do fluorescence decays remitted from tissues accurately reflect intrinsic fluorophore lifetimes?" Opt. Lett. **29**, 1512-1514 (2004).

38. W. Lloyd, R. H. Wilson, C.-W. Chang, G. D. Gillispie, and M.-A. Mycek, "Instrumentation to rapidly acquire fluorescence wavelength-time matrices of biological tissues," Biomed. Opt. Express **1**, 574-586 (2010).

39. P. Matousek, E. R. C. Draper, A. E. Goodship, I. P. Clark, K. L. Ronayne, and A. W. Parker, "Noninvasive Raman spectroscopy of human tissue *in vivo*," Appl. Spectrosc. **60**, 758-763 (2006).

40. N. Rajaram, T. J. Aramil, K. Lee, J. S. Reichenberg, T. H. Nguyen, and J. W. Tunnell, "Design and validation of a clinical instrument for spectral diagnosis of cutaneous malignancy," Appl. Opt. **49**, 142-152 (2010).

41. N. Ghosh, S. K. Mohanty, S. K. Majumder, and P. K. Gupta, "Measurement of optical transport properties of normal and malignant human breast tissue," Appl. Opt. **40**, 176-184 (2001).

42. J. Sun, K. Fu, A. Wang, A. W. H. Lin, U. Utzinger, and R. Drezek, "Influence of fiber optic probe geometry on the applicability of inverse models of tissue reflectance spectroscopy: computational models and experimental measurements," Appl. Opt. **45**, 8152–8162 (2006).

43. G. M. Palmer, C. Zhu, T. M. Breslin, F. Xu, K. W. Gilchrist, and N. Ramanujam, "Monte Carlo-based inverse model for calculating tissue optical properties. Part II: Application to breast cancer diagnosis," Appl. Opt. **45**, 1072-1078 (2006).

44. V. T.-C. Chang, P. S. Cartwright, S. M. Bean, G. M. Palmer, R. C. Bentley, and N. Ramanujam, "Quantitative physiology of the precancerous cervix *in vivo* through optical spectroscopy," Neoplasia **11**, 325-332 (2009).

45. E. Salomatina, B. Jiang, J. Novak, and A. N. Yaroslavsky, "Optical properties of normal and cancerous human skin in the visible and near-infrared spectral range," J. Biomed. Opt. **11**, 064026 (2006).

46. D. Arifler, C. MacAulay, M. Follen, and R. Richards-Kortum, "Spatially resolved reflectance spectroscopy for diagnosis of cervical precancer: Monte Carlo modeling and comparison to clinical measurements," J. Biomed. Opt. **11**, 064027 (2006).

47. J. N. Winn, L. T. Perelman, K. Chen, J. Wu, R. R. Dasari, and M. S. Feld, "Distribution of the paths of early-arriving photons traversing a turbid medium," Appl. Opt. **37**, 8085-8091 (1998).

48. K. M. Yoo, F. Liu, and R. R. Alfano, "When does the diffusion approximation fail to describe photon transport in random media?" Phys. Rev. Lett. **64** (1990).

49. C. F. Bohren and D. A. Huffman, *Absorption and Scattering of Light by Small Particles* (John Wiley & Sons, New York, 1983).

50. C.-C. Yu, C. Lau, G. O'Donoghue, J. Mirkovic, S. McGee, L. Galindo, A. Elackttu, E. Stier, G. Grillone, K. Badizadegan, R. R. Dasari, and M. S. Feld, "Quantitative spectroscopic imaging for non-invasive early cancer detection," Opt. Express **16**, 16227-16239 (2008).

51. A. Sefkow, M. Bree, and M.-A. Mycek, "A method for measuring cellular optical absorption and scattering evaluated using dilute cell suspension phantoms," Appl. Spectrosc. **55**, 1495-1501 (2001).

52. R. Reif, M. S. Amorosino, K. W. Calabro, O. A'Amar, S. K. Singh, and I. J. Bigio, "Analysis of changes in reflectance measurements on biological tissues subjected to different probe pressures," J. Biomed. Opt. **13**, 010502 (2008).

53. M. G. Giacomelli, K. J. Chalut, J. H. Ostrander, and A. Wax, "Application of the T-matrix method to determine the structure of spheroidal cell nuclei with angle-resolved light scattering," Opt. Lett. **33**, 2452-2454 (2008).

54. S. K. Chang, D. Arifler, R. Drezek, M. Follen, and R. Richards-Kortum, "Analytical model to describe fluorescence spectra of normal and preneoplastic epithelial tissue: comparison with Monte Carlo simulations and clinical measurements," J. Biomed. Opt. **9**, 511-522 (2004).

55. M. S. Nair, N. Ghosh, N. S. Raju, and A. Pradhan, "Determination of optical parameters of human breast tissue from spatially resolved fluorescence: a diffusion theory model," Appl. Opt. **41**, 4024-4035 (2002).

56. R. Drezek, K. Sokolov, U. Utzinger, I. Boiko, A. Malpica, M. Follen, and R. Richards-Kortum, "Understanding contributions of NADH and collagen to cervical tissue fluorescence spectra: Modeling, measurements, and implications," J. Biomed. Opt. **6**, 385-396 (2001).

57. I. Pavlova, C. Redden Weber, R. A. Schwarz, M. Williams, A. El-Naggar, A. Gillenwater, and R. Richards-Kortum, "Monte Carlo model to describe depth selective fluorescence spectra of epithelial tissue: applications for diagnosis of oral precancer," J. Biomed. Opt. **13**, 064012 (2008).

58. I. Pavlova, C. Redden Weber, R. A. Schwarz, M. D. Williams, A. M. Gillenwater, and R. Richards-Kortum, "Fluorescence spectroscopy of oral tissue: Monte Carlo modeling with site-specific tissue properties," J. Biomed. Opt. **14**, 014009 (2009).

59. C. Redden Weber, R. A. Schwarz, E. N. Atkinson, D. D. Cox, C. Macaulay, M. Follen, and R. Richards-Kortum, "Model-based analysis of reflectance and fluorescence spectra for *in vivo* detection of cervical dysplasia and cancer," J. Biomed. Opt. **13**, 064016 (2008).

60. W. M. Star, J. P. A. Marijnissen, and M. J. C. van Gemert, "Light Dosimetry in optical phantoms and in tissues: I. Multiple flux and transport theory," Phys. Med. Biol. **33**, 437-454 (1988).

61. T. J. Farrell, M. S. Patterson, and B. C. Wilson, "A diffusion theory model of spatially resolved, steady-state diffuse reflectance for the noninvasive determination of tissue optical properties *in vivo*," Med. Phys. **19**, 879-888 (1992).

62. M. S. Patterson and B. W. Pogue, "Mathematical model for time-resolved and frequency-domain fluorescence spectroscopy in biological tissues," Appl. Opt. **33**, 1963-1974 (1994).

63. A. Kienle and M. S. Patterson, "Improved solutions of the steady-state and the time-resolved diffusion equations for reflectance from a semi-infinite turbid medium," J. Opt. Soc. Am. A Opt. Image Sci. Vis. **14**, 246-254 (1997).

64. W. Cai, M. Xu, M. Lax, and R. R. Alfano, "Diffusion coefficient depends on time, not on absorption," Opt. Lett. **27**, 731-733 (2002).

65. M. E. Zevallos, A. Ya Polischuck, B. B. Das, F. Liu, and R. R. Alfano, "Time-resolved photon-scattering measurements from scattering media fitted to non-Euclidean and conventional diffusion models," Phys. Rev. E **57**, 7244-7253 (1998).

66. E. L. Hull and T. H. Foster, "Steady-state reflectance spectroscopy in the P_3 approximation," J. Opt. Soc. Am. A Opt. Image Sci. Vis. **18**, 584-599 (2001).

67. K. G. Phillips and S. L. Jacques, "Solution of transport equations in layered media with refractive index mismatch using the P_N-method," J. Opt. Soc. Am. A Opt. Image Sci. Vis. **26**, 2147-2162 (2009).

68. G. Zonios, I. Bassukas, and A. Dimou, "Comparative evaluation of two simple diffuse reflectance models for biological tissue applications," Appl. Opt. **47**, 4965-4973 (2008).

69. G. Zonios and A. Dimou, "Modeling diffuse reflectance from semi-infinite turbid media: application to the study of skin optical properties," Opt. Express **14**, 8661-8674 (2006).

70. A. Garofalakis, G. Zacharakis, G. Filippidis, E. Sanidas, D. D. Tsiftsis, E. Stathopoulos, M. Kafousi, J. Ripoll, and T. G. Papazoglou, "Optical characterization of thin female breast biopsies based on the reduced scattering coefficient," Phys. Med. Biol. **50**, 2583-2596 (2005).

71. Y. S. Fawzy, M. Petek, M. Tercelj, and H. Zeng, "*In vivo* assessment and evaluation of lung tissue morphologic and physiological changes from non-contact endoscopic reflectance spectroscopy for improving lung cancer detection," J. Biomed. Opt. **11**, 044003 (2006).

72. B. C. Wilson and G. Adam, "A Monte Carlo model for the absorption and flux distribution of light in tissue," Med. Phys. **10**, 824-830 (1983).

73. S. T. Flock, M. S. Patterson, B. C. Wilson, and D. R. Wyman, "Monte Carlo modeling of light propagation in highly scattering tissues-I: Model predictions

and comparison with diffusion theory," IEEE Trans. Biomed. Eng. **36**, 824-830 (1989).

74. S. T. Flock, B. C. Wilson, and M. S. Patterson, "Monte Carlo modeling of light propagation in highly scattering tissues-II: Comparsion with measurements in phantoms," IEEE Trans. Biomed. Eng. **36**, 1169-1173 (1989).

75. L. Wang, S. L. Jacques, and L. Zheng, "MCML - Monte Carlo modeling of photon transport in multi-layered tissues," Comput. Methods Programs Biomed. **47**, 131-146 (1995).

76. K. Vishwanath, B. W. Pogue, and M.-A. Mycek, "Quantitative fluorescence lifetime spectroscopy in turbid media: comparison of theoretical, experimental and computational methods," Phys. Med. Biol. **47**, 3387-3405 (2002).

77. K. Vishwanath and M.-A. Mycek, "Time-resolved photon migration in bi-layered tissue models," Opt. Express **13**, 7466-7482 (2005).

78. D. A. Boas, J. P. Culver, J. J. Stott, and A. K. Dunn, "Three dimensional Monte Carlo code for photon migration through complex heterogeneous media including the adult human head," Opt. Express **10**, 159-170 (2002).

79. E. Margallo-Balbás and P. J. French, "Shape based Monte Carlo code for light transport in complex heterogeneous tissues," Opt. Express **15**, 14086-14098 (2007).

80. G. Ma, J.-F. Delorme, P. Gallant, and D. A. Boas, "Comparison of simplified Monte Carlo simulation and diffusion approximation for the fluorescence signal from phantoms with typical mouse tissue optical properties," Appl. Opt. **46**, 1686-1692 (2007).

81. T. J. Pfefer, A. Agrawal, and R. A. Drezek, "Oblique-incidence illumination and collection for depth-selective fluorescence spectroscopy," J. Biomed. Opt. **10**, 044016 (2005).

82. A. Wang, V. Nammalavar, and R. Drezek, "Targeting spectral signatures of progressively dysplastic stratified epithelia using angularly variable fiber geometry in reflectance Monte Carlo simulations," J. Biomed. Opt. **12**, 044012 (2007).

83. E. Alerstam, T. Svensson, and S. Andersson-Engels, "Parallel computing with graphics processing units for high-speed Monte Carlo simulation of photon migration," J. Biomed. Opt. **13**, 060504 (2008).

84. Q. Fang and D. A. Boas, "Monte Carlo simulation of photon migration in 3D turbid media accelerated by graphics processing units," Opt. Express **17**, 20178-20190 (2009).

85. N. Ren, J. Liang, X. Qu, J. Li, B. Lu, and J. Tian, "GPU-based Monte Carlo simulation for light propagation in complex heterogeneous tissues," Opt. Express **18**, 6811-6823 (2010).

86. R. Graaff, M. H. Koelink, F. F. M. de Mul, W. G. Zijlstra, A. C. M. Dassel, and J. G. Aarnoudse, "Condensed Monte Carlo simulations for the description of light transport," Appl. Opt. **32**, 426-434 (1993).

87. Q. Liu and N. Ramanujam, "Scaling method for fast Monte Carlo simulation of diffuse reflectance spectra from multilayered turbid media," J. Opt. Soc. Am. A Opt. Image Sci. Vis. **24**, 1011-1025 (2007).

88. J. Swartling, A. Pifferi, A. M. K. Enejder, and S. Andersson-Engels, "Accelerated Monte Carlo models to simulate fluorescence spectra from layered tissues," J. Opt. Soc. Am. A Opt. Image Sci. Vis. **20**, 714-727 (2003).

89. A. Kienle and M. S. Patterson, "Determination of the optical properties of turbid media from a single Monte Carlo simulation," Phys. Med. Biol. **41**, 2221-2227 (1996).

90. E. Péry, W. C. P. M. Blondel, C. Thomas, and F. Guillemin, "Monte Carlo modeling of multilayer phantoms with multiple fluorophores: simulation algorithm and experimental validation," J. Biomed. Opt. **14**, 024048 (2009).

91. C. Zhu, G. M. Palmer, T. M. Breslin, J. Harter, and N. Ramanujam, "Diagnosis of breast cancer using diffuse reflectance spectroscopy: Comparison of a Monte Carlo versus partial least squares analysis based feature extraction technique," Lasers Surg. Med. **38**, 714-724 (2006).

92. C. Zhu, T. M. Breslin, J. Harter, and N. Ramanujam, "Model based and empirical spectral analysis for the diagnosis of breast cancer," Opt. Express **16**, 14961-14978 (2008).

93. R. Reif, O. A'Amar, and I. J. Bigio, "Analytical model of light reflectance for extraction of the optical properties in small volumes of turbid media," Appl. Opt. **46**, 7317-7328 (2007).

94. R. Marchesini, A. Bono, and M. Carrara, "*In vivo* characterization of melanin in melanocytic lesions: spectroscopic study on 1671 pigmented skin lesions," J. Biomed. Opt. **14**, 014027 (2009).

95. "Cancer Facts & Figures 2011" (American Cancer Society), *www.cancer.org*.

96. W. Hartwig, L. Schneider, M. K. Diener, F. Bergmann, M. W. Büchler, and J. Werner, "Preoperative tissue diagnosis for tumours of the pancreas," Br. J. Surg. **96**, 5-20 (2009).

97. A. Fritscher-Ravens, L. Brand, W. T. Knöfel, C. Bobrowski, T. Topalidis, F. Thonke, A. de Werth, and N. Soehendra, "Comparison of endoscopic ultrasound-guided fine needle aspiration for focal pancreatic lesions in patients with normal parenchyma and chronic pancreatitis," Am. J. Gastroenterol. **97**, 2768-2775 (2002).

98. S. C. Abraham, R. E. Wilentz, C. J. Yeo, T. A. Sohn, J. L. Cameron, J. K. Boitnott, and R. H. Hruban, "Pancreaticoduodenectomy (Whipple resections) in

patients without malignancy: are they all `chronic pancreatitis'?" Am. J. Surg. Pathol. **27**, 110-120 (2003).

99. P. A. Testoni, B. Mangiavillano, L. Albarello, P. G. Arcidiacono, A. Mariani, E. Masci, and C. Doglioni, "Optical coherence tomography to detect epithelial lesions of the main pancreatic duct: an *ex vivo* study," Am. J. Gastroenterol. **100**, 2777-2783 (2005).

100. P. A. Testoni, A. Mariani, B. Mangiavillano, P. G. Arcidiacono, S. Di Pietro, and E. Masci, "Intraductal optical coherence tomography for investigating main pancreatic duct strictures," Am. J. Gastroenterol. **102**, 269-274 (2007).

101. V. R. Kondepati, J. Zimmermann, M. Keese, J. Sturm, B. C. Manegold, and J. Backhaus, "Near-infrared fiber optic spectroscopy as a novel diagnostic tool for the detection of pancreatic cancer," J. Biomed. Opt. **10**, 054016 (2005).

102. H. Subramanian, P. Pradhan, Y. Liu, I. R. Capoglu, J. D. Rogers, H. K. Roy, R. E. Brand, and V. Backman, "Partial-wave microscopic spectroscopy detects subwavelength refractive index fluctuations: an application to cancer diagnosis," Opt. Lett. **34**, 518-520 (2009).

103. V. Krishnaswamy, P. J. Hoopes, K. S. Samkoe, J. A. O'Hara, T. Hasan, and B. W. Pogue, "Quantitative imaging of scattering changes associated with epithelial proliferation, necrosis, and fibrosis in tumors using microsampling reflectance spectroscopy," J. Biomed. Opt. **14**, 014004 (2009).

104. M. Chandra, D. Heidt, D. Simeone, B. McKenna, J. Scheiman, and M.-A. Mycek, "Pancreatic tissue assessment using fluorescence and reflectance spectroscopy," Proc. SPIE Int. Soc. Opt. Eng. **6628**, 66281R (2007).

105. R. H. Wilson, M. Chandra, J. Scheiman, D. Simeone, B. McKenna, J. Purdy, and M.-A. Mycek, "Mathematical modeling of reflectance and intrinsic fluorescence for early cancer detection in human pancreatic tissue," Proc. SPIE Int. Soc. Opt. Eng. **7187**, 71870H (2009).

106. M. Chandra, K. Vishwanath, G. D. Fichter, E. Liao, S. J. Hollister, and M.-A. Mycek, "Quantitative molecular sensing in biological tissues: an approach to non-invasive optical characterization," Opt. Express **14**, 6157-6171 (2006).

107. L. T. Perelman, V. Backman, M. Wallace, G. Zonios, R. Manoharan, A. Nusrat, S. Shields, M. Seiler, C. Lima, T. Hamano, I. Itzkan, J. Van Dam, J. M. Crawford, and M. S. Feld, "Observation of periodic fine structure in reflectance from biological tissue: a new technique for measuring nuclear size distribution," Phys. Rev. Lett. **80**, 627-630 (1998).

108. V. Backman, R. Gurjar, K. Badizadegan, L. Itzkan, R. R. Dasari, L. T. Perelman, and M. S. Feld, "Polarized light scattering spectroscopy for quantitative measurement of epithelial cellular structures *in situ*," IEEE J. Sel. Top. Quantum Electron. **5**, 1019-1026 (1999).

109. M. B. Cohen, D. P. Egerter, E. A. Holly, D. K. Ahn, and T. R. Miller, "Pancreatic adenocarcinoma: regression analysis to identify improved cytologic criteria," Diagn. Cytopathol. **7**, 341-345 (1991).

110. R. J. Sears, C. W. Duckworth, C. Decaestecker, N. Bourgeois, T. Ledent, J. Deviere, I. Salmon, R. Kiss, and P. Yeaton, "Image cytometry as a discriminatory tool for cytologic specimens obtained by endoscopic retrograde cholangiopancreatography," Cancer **84**, 119-126 (1998).

111. F. Lin and G. Staerkel, "Cytologic criteria for well differentiated adenocarcinoma of the pancreas in fine-needle aspiration biopsy samples," Cancer **99**, 44-50 (2003).

112. T. Imamura, H. Iguchi, T. Manabe, G. Ohshio, T. Yoshimura, Z. H. Wang, H. Suwa, S. Ishigami, and M. Imamura, "Quantitative analysis of collagen and collagen subtypes I, III, and V in human pancreatic cancer, tumor-associated chronic pancreatitis, and alcoholic chronic pancreatitis," Pancreas **11**, 357-364 (1995).

113. S. Prahl, "Optical Absorption of Hemoglobin" (Oregon Medical Laser Center, 1999), *http://omlc.ogi.edu/spectra/hemoglobin*.

114. R. L. P. van Veen, W. Verkruysse, and H. J. C. M. Sterenborg, "Diffuse-reflectance spectroscopy from 500 to 1060 nm by correction for inhomogeneously distributed absorbers," Opt. Lett. **27**, 246-248 (2002).

115. R. Rzepko, K. Jaśkiewicz, M. Klimkowska, A. Nalecz, and E. Izycka-Swieszewska, "Microvascular density in chronic pancreatitis and pancreatic ductal adenocarcinoma," Folia Histochem. Cytobiol. **41**, 237-239 (2003).

116. P. Hillemanns, J. Reiff, H. Stepp, and P. Soergel, "Lymph node metastasis detection of ovarian cancer by porphyrin fluorescence photodetection: case report," Lasers Med. Sci. **22**, 131-135 (2007).

117. J. C. Finlay and T. H. Foster, "Effect of pigment packaging on diffuse reflectance spectroscopy of samples containing red blood cells," Opt. Lett. **29**, 965-967 (2004).

118. J. Köninger, N. A. Giese, F. F. di Mola, P. Berberat, T. Giese, I. Esposito, M. G. Bachem, M. W. Büchler, and H. Friess, "Overexpressed decorin in pancreatic cancer: potential tumor growth inhibition and attenuation of chemotherapeutic action," Clin. Cancer Res. **10**, 4776-4783 (2004).

119. R. H. Hruban, K. Takaori, D. S. Klimstra, N. V. Adsay, J. Albores-Saavedra, A. V. Biankin, S. A. Biankin, C. Compton, N. Fukushima, T. Furukawa, M. Goggins, Y. Kato, G. Klöppel, D. S. Longnecker, J. Lüttges, A. Maitra, G. J. Offerhaus, M. Shimizu, and S. Yonezawa, "An illustrated consensus on the classification of pancreatic intraepithelial neoplasia and intraductal papillary mucinous neoplasms," Am. J. Surg. Pathol. **28**, 977-987 (2004).

120. R. H. Hruban, N. V. Adsay, J. Albores-Saavedra, C. Compton, E. S. Garrett, S. N. Goodman, S. E. Kern, D. S. Klimstra, G. Klöppel, D. S. Longnecker, J. Lüttges,

and G. J. Offerhaus, "Pancreatic intraepithelial neoplasia: a new nomenclature and classification system for pancreatic duct lesions," Am. J. Surg. Pathol. **25**, 579-586 (2001).

121. J. R. Mourant, J. P. Freyer, A. H. Hielscher, A. A. Eick, D. Shen, and T. M. Johnson, "Mechanisms of light scattering from biological cells relevant to noninvasive optical-tissue diagnostics," Appl. Opt. **37**, 3586-3593 (1998).

122. M. Xu, T. T. Wu, and J. Y. Qu, "Unified Mie and fractal scattering by cells and experimental study on application in optical characterization of cellular and subcellular structures," J. Biomed. Opt. **13**, 024015 (2008).

123. M. G. Müller, I. Georgakoudi, Q. Zhang, J. Wu, and M. S. Feld, "Intrinsic fluorescence spectroscopy in turbid media: disentagling effects of scattering and absorption," Appl. Opt. **40**, 4633-4646 (2001).

124. G. M. Palmer and N. Ramanujam, "Monte-Carlo-based model for the extraction of intrinsic fluorescence from turbid media," J. Biomed. Opt. **13**, 024017 (2008).

125. J. C. Finlay and T. H. Foster, "Hemoglobin oxygen saturations in phantoms and *in vivo* from measurements of steady-state diffuse reflectance at a single, short source-detector separation," Med. Phys. **31**, 1949-1959. (2004).

126. B. W. Killough, C. A. Nichols, J. A. Nicholson, and T. S. Gansler, "Diagnosis of pancreatic carcinoma by fine needle aspiration cytology and computerized cytomorphometry," Anal. Quant. Cytol. Histol. **11**, 238-242 (1989).

127. A. R. Weger and J. L. Lindholhm, "Discrimination of pancreatic adenocarcinomas from chronic pancreatitis by morphometric analysis," Pathol. Res. Pract. **188**, 44-48 (1992).

128. M. Chandra, J. Scheiman, D. Simeone, B. McKenna, J. Purdy, and M.-A. Mycek, "Spectral areas and ratios classifier algorithm for pancreatic tissue classification using optical spectroscopy," J. Biomed. Opt. **15**, 010514 (2010).

129. P. M. Pour, Y. Konishi, G. Klöppel, and D. S. Longnecker, *Atlas of exocrine pancreatic tumors* (Springer-Verlag, Tokyo, 1994).

130. A. C. Koong, V. K. Mehta, Q. T. Le, G. A. Fisher, D. J. Terris, J. M. Brown, A. J. Bastidas, and M. Vierra, "Pancreatic tumors show high levels of hypoxia," Int. J. Radiat. Oncol. Biol. Phys. **48**, 919-922 (2000).

131. S. Kersting, R. Konopke, F. Kersting, A. Volk, M. Distler, H. Bergert, H.-D. Saeger, R. Grützmann, and A. Bunk, "Quantitative perfusion analysis of transabdominal contrast-enhanced ultrasonography of pancreatic masses and carcinomas," Gastroenterology **137**, 1903-1911 (2009).

132. D. C. G. de Veld, M. Skurichina, M. J. H. Witjes, R. P. W. Duin, H. J. C. M. Sterenborg, and J. L. N. Roodenburg, "Autofluorescence and diffuse reflectance spectroscopy for oral oncology," Lasers Surg. Med. **36**, 356-364 (2005).

133. M. D. Keller, S. K. Majumder, M. C. Kelley, I. M. Meszoely, F. I. Boulos, G. M. Olivares, and A. Mahadevan-Jansen, "Autofluorescence and diffuse reflectance

spectroscopy and spectral imaging for breast surgical margin analysis," Lasers Surg. Med. **42**, 15-23 (2010).

134. I. T. Jolliffe, *Principal Component Analysis* (Springer, New York, 2002).

135. J. A. Hanley, A. Negassa, M. D. Eduardes, and J. E. Forrester, "Statistical analysis of correlated data using generalized estimating equations: an orientation," Am. J. Epidemiol. **157**, 364-375 (2003).

136. P. Burton, L. Gurrin, and P. Sly, "Extending the simple linear regression model to account for correlated responses: An introduction to generalized estimating equations and multi-level mixed modelling," Stat. Med. **17**, 1261-1291 (1998).

137. O. Kuss and D. McLerran, "A note on the estimation of the multinomial logistic model with correlated responses in SAS," Comput. Methods Programs Biomed. **87**, 262-269 (2007).

138. G. Vizzeri, R. N. Weinreb, A. O. Gonzalez-Garcia, C. Bowd, F. A. Medeiros, P. A. Sample, and L. M. Zangwill, "Agreement between spectral-domain and time-domain OCT for measuring RNFL thickness," Br. J. Ophthalmol. **93**, 775-781 (2009).

139. D. L. Fortes, M. S. Allen, V. J. Lowe, K.-H. R. Shen, D. A. Wigle, S. D. Cassivi, F. C. Nichols, and C. Deschamps, "The sensitivity of 18F-fluorodeoxyglucose positron emission tomography in the evaluation of metastatic pulmonary nodules," Eur. J. Cardiothorac. Surg. **34**, 1223-1227 (2008).

140. R. F. Brem, A. C. Floerke, J. A. Rapelyea, C. Teal, T. Kelly, and V. Mathur, "Breast-specific Gamma imaging as an adjunct imaging modality for the diagnosis of breast cancer," Radiology **247**, 651-657 (2008).

141. A. Toi, M. G. Neill, G. A. Lockwood, J. M. Sweet, L. A. Tammsalu, and N. E. Fleshner, "The continuing importance of transrectal ultrasound identification of prostatic lesions," J. Urol. **177**, 516-520 (2007).

142. A. Amelink, O. P. Kaspers, H. J. Sterenborg, J. E. van der Wal, J. L. Roodenburg, and M. J. Witjes, "Non-invasive measurement of the morphology and physiology of oral mucosa by use of optical spectroscopy," Oral Oncol. **44**, 65-71 (2008).

143. R. A. Schwarz, W. Gao, D. Daye, M. D. Williams, R. Richards-Kortum, and A. M. Gillenwater, "Autofluorescence and diffuse reflectance spectroscopy of oral epithelial tissue using a depth-sensitive fiber-optic probe," Appl. Opt. **47**, 825-834 (2008).

144. "Condition Kit on Osteoporosis" (United States Bones and Joint Decade, NFP, 2004).

145. J. D. Lee, Y. Chen, X. Zeng, A. Eskandarian, and M. Oskard, "Modeling and simulation of osteoporosis and fracture of trabecular bone by meshless method," Int. J. Eng. Sci. **45**, 329-338 (2007).

146. A. Carden and M. D. Morris, "Application of vibrational spectroscopy to the study of mineralized tissues (review)," J. Biomed. Opt. **5**, 259-268 (2000).

147. M. V. Schulmerich, K. A. Dooley, M. D. Morris, T. M. Vanasse, and S. A. Goldstein, "Transcutaneous fiber optic Raman spectroscopy of bone using annular illumination and a circular array of collection fibers," J. Biomed. Opt. **11**, 060502 (2006).

148. M. V. Schulmerich, J. H. Cole, K. A. Dooley, M. D. Morris, J. M. Kreider, S. A. Goldstein, S. Srinivasan, and B. W. Pogue, "Noninvasive Raman tomographic imaging of canine bone tissue," J. Biomed. Opt. **13**, 020506 (2008).

149. M. V. Schulmerich, K. A. Dooley, T. M. Vanasse, S. A. Goldstein, and M. D. Morris, "Subsurface and transcutaneous Raman spectroscopy and mapping using concentric illumination rings and collection with a circular fiber-optic array," Appl. Spectrosc. **61**, 671-678 (2007).

150. S. L. Jacques and L. Wang, "Monte Carlo modeling of light transport in tissue," in *Optical-Thermal Response of Laser-Irradiated Tissue*, A. J. Welch, and M. J. C. van Gemert, eds. (Plenum Press, New York, 1995), pp. 15-46.

151. J. T. Motz, M. Hunter, L. H. Galindo, J. A. Gardecki, J. R. Kramer, R. R. Dasari, and M. S. Feld, "Optical fiber probe for biomedical Raman spectroscopy," Appl. Opt. **43**, 542-554 (2004).

152. P. Matousek, M. D. Morris, N. Everall, I. P. Clark, M. Towrie, E. Draper, A. Goodship, and A. W. Parker, "Numerical simulations of subsurface probing in diffusely scattering media using spatially offset Raman spectroscopy," Appl. Spectrosc. **59**, 1485-1492 (2005).

153. W. C. Shih, K. L. Bechtel, and M. S. Feld, "Intrinsic Raman spectroscopy for quantitative biological spectroscopy Part 1: Theory and simulations," Opt. Express **16**, 12726–12736 (2008).

154. R. H. Wilson, K. A. Dooley, M. D. Morris, and M.-A. Mycek, "Monte Carlo modeling of photon transport in buried bone tissue layer for quantitative Raman spectroscopy," Proc. SPIE Int. Soc. Opt. Eng. **7166**, 716604 (2009).

155. J. W. Pickering, S. A. Prahl, N. van Wieringen, J. F. Beek, H. J. Sterenborg, and M. J. van Gemert, "Double integrating sphere system for measuring the optical properties of tissue," Appl. Opt. **32**, 399-410 (1993).

156. T. Moffitt, Y. C. Chen, and S. A. Prahl, "Preparation and characterization of polyurethane optical phantoms," J. Biomed. Opt. **11**, 041103 (2006).

157. S. A. Prahl, M. J. C. van Gemert, and A. J. Welch, "Determining the optical properties of turbid media by using the adding-doubling method," Appl. Opt. **32**, 559-568 (1993).

158. S. Döpner, F. Müller, P. Hildebrandt, and R. T. Müller, "Integration of metallic endoprotheses in dog femur studied by near-infrared Fourier-transform Raman microscopy," Biomaterials **23**, 1337-1345 (2002).

159. C. R. Simpson, M. Kohl, M. Essenpreis, and M. Cope, "Near-infrared optical properties of *ex vivo* human skin and subcutaneous tissues measured using the Monte Carlo inversion technique," Phys. Med. Biol. **43**, 2465-2478 (1998).

160. J. J. Dirckx, L. C. Kuypers, and W. F. Decraemer, "Refractive index of tissue measured with confocal microscopy," J. Biomed. Opt. **10**, 044014 (2005).

161. N. Stone, R. Baker, K. Rogers, A. W. Parker, and P. Matousek, "Subsurface probing of calcifications with spatially offset Raman spectroscopy (SORS): future possibilities for the diagnosis of breast cancer," Analyst **132**, 899-905 (2007).

162. M. V. Schulmerich, W. F. Finney, R. A. Fredricks, and M. D. Morris, "Subsurface Raman spectroscopy and mapping using a globally illuminated non-confocal fiber-optic array probe in the presence of Raman photon migration," Appl. Spectrosc. **60**, 109-114 (2006).

163. P. Matousek, "Inverse spatially offset Raman spectroscopy for deep noninvasive probing of turbid media," Appl. Spectrosc. **60**, 1341-1347 (2006).

164. P. Matousek, I. P. Clark, E. R. Draper, M. D. Morris, A. E. Goodship, N. Everall, M. Towrie, W. F. Finney, and A. W. Parker, "Subsurface probing in diffusely scattering media using spatially offset Raman spectroscopy," Appl. Spectrosc. **59**, 393-400 (2005).

165. M. D. Keller, S. K. Majumder, and A. Mahadevan-Jansen, "Spatially offset Raman spectroscopy of layered soft tissues," Opt. Lett. **34**, 926-928 (2009).

166. M. V. Schulmerich, J. H. Cole, J. M. Kreider, F. Esmonde-White, K. A. Dooley, S. A. Goldstein, and M. D. Morris, "Transcutaneous Raman spectroscopy of murine bone *in vivo*," Appl. Spectrosc. **63**, 286-295 (2009).

167. N. A. Macleod and P. Matousek, "Deep noninvasive Raman spectroscopy of turbid media," Appl. Spectrosc. **62**, 291A-304A (2008).

168. N. A. Macleod, A. Goodship, A. W. Parker, and P. Matousek, "Prediction of sublayer depth in turbid media using spatially offset Raman spectroscopy," Anal. Chem. **80**, 8146-8152 (2008).

169. M. D. Keller, R. H. Wilson, M.-A. Mycek, and A. Mahadevan-Jansen, "Monte Carlo model of spatially offset Raman spectroscopy for breast tumor margin analysis," Appl. Spectrosc. **64**, 607-614 (2010).

170. "Cancer Facts & Figures 2009" (American Cancer Society), *www.cancer.org*.

171. C. Dunne, J. P. Burke, M. Morrow, and M. R. Kell, "Effect of margin status on local recurrence after breast conservation and radiation therapy for ductal carcinoma *in situ*," J. Clin. Oncol. **27**, 1615-1620 (2009).

172. K. C. Horst, M. C. Smitt, D. R. Goffinet, and R. W. Carlson, "Predictors of local recurrence after breast-conservation therapy," Clin. Breast Cancer **5**, 425-438 (2005).

173. A. Taghian, M. Mohiuddin, R. Jagsi, S. Goldberg, E. Ceilley, and S. Powell, "Current perceptions regarding surgical margin status after breast-conserving therapy: results of a survey," Ann. Surg. **241**, 629-639 (2005).

174. N. Cabioglu, K. K. Hunt, A. A. Sahin, H. M. Kuerer, G. V. Babiera, S. E. Singletary, G. J. Whitman, M. I. Ross, F. C. Ames, B. W. Feig, T. A. Buchholz, and F. Meric-Bernstam, "Role for intraoperative margin assessment in patients undergoing breast-conserving surgery," Ann. Surg. Oncol. **14**, 1458-1471 (2007).

175. E. K. Valdes, S. K. Boolbol, I. Ali, S. M. Feldman, and J. M. Cohen, "Intraoperative touch preparation cytology for margin assessment in breast-conservation surgery: does it work for lobular carcinoma?" Ann. Surg. Oncol. **14**, 2940-2945 (2007).

176. T. P. Olson, J. Harter, A. Muñoz, D. M. Mahvi, and T. Breslin, "Frozen section analysis for intraoperative margin assessment during breast-conserving surgery results in low rates of re-excision and local recurrence," Ann. Surg. Oncol. **14**, 2953-2960 (2007).

177. G. C. Balch, S. K. Mithani, J. F. Simpson, and M. C. Kelley, "Accuracy of intraoperative gross examination of surgical margin status in women undergoing partial mastectomy for breast malignancy," Am. Surg. **71**, 22-27; discussion 27-28 (2005).

178. A. M. K. Enejder, T.-W. Koo, J. Oh, M. Hunter, S. Sasic, M. S. Feld, and G. L. Horowitz, "Blood analysis by Raman spectroscopy," Opt. Lett. **27**, 2004-2006 (2002).

179. A. Mahadevan-Jansen, "Raman Spectroscopy: From Benchtop to Bedside," in *Biomedical Photonics Handbook*, T. Vo-Dinh, ed. (CRC Press, Washington DC, 2003).

180. S. Sathyendranath and T. Platt, "Ocean-color model incorporating transspectral processes," Appl. Opt. **37**, 2216-2227 (1998).

181. D. Passos, J. C. Hebden, P. N. Pinto, and R. Guerra, "Tissue phantom for optical diagnostics based on a suspension of microspheres with a fractal size distribution," J. Biomed. Opt. **10**, 064036 (2005).

182. M. R. Arnfield, J. Tulip, and M. S. McPhee, "Optical propagation in tissue with anisotropic scattering," IEEE Trans. Biomed. Eng. **35**, 372-381 (1988).

183. D. Grosenick, H. Wabnitz, K. T. Moesta, J. Mucke, P. M. Schlag, and H. Rinneberg, "Time-domain scanning optical mammography: II. Optical properties and tissue parameters of 87 carcinomas," Phys. Med. Biol. **50**, 2451-2468 (2005).

184. A. Cerussi, N. Shah, D. Hsiang, A. Durkin, J. Butler, and B. J. Tromberg, "*In vivo* absorption, scattering, and physiologic properties of 58 malignant breast tumors determined by broadband diffuse optical spectroscopy," J. Biomed. Opt. **11**, 044005 (2006).

185. B. J. Tromberg, N. Shah, R. Lanning, A. Cerussi, J. Espinoza, T. Pham, L. Svaasand, and J. Butler, "Non-invasive *in vivo* characterization of breast tumors using photon migration spectroscopy," Neoplasia **2**, 26-40 (2000).

186. S. Srinivasan, M. Schulmerich, J. H. Cole, K. A. Dooley, J. M. Kreider, B. W. Pogue, M. D. Morris, and S. A. Goldstein, "Image-guided Raman spectroscopic recovery of canine cortical bone contrast *in situ*," Opt. Express **16**, 12190-12200 (2008).

187. N. Everall, P. Matousek, N. MacLeod, K. L. Ronayne, and I. P. Clark, "Temporal and spatial resolution in transmission Raman spectroscopy," Appl. Spectrosc. **64**, 52-60 (2010).

188. "Cancer Facts & Figures 2010" (American Cancer Society), *www.cancer.org*.

189. K. I. Bland and E. M. Copeland 3rd, eds., *The Breast: Comprehensive Management of Benign and Malignant Disorders* (Saunders, St. Louis, 2004).

190. J. C. Cendán, D. Coco, and E. M. Copeland 3rd, "Accuracy of intraoperative frozen-section analysis of breast cancer lumpectomy-bed margins," J. Am. Coll. Surg. **201**, 194-198 (2005).

191. P. Matousek, "Deep non-invasive Raman spectroscopy of living tissue and powders," Chem. Soc. Rev. **36**, 1292-1304 (2007).

192. M. D. Keller, E. Vargis, N. de Matos Granja, R. H. Wilson, M.-A. Mycek, M. C. Kelley, and A. Mahadevan-Jansen, "Development of a spatially offset Raman spectroscopy probe for breast tumor surgical margin evaluation," J. Biomed. Opt. **16**, 077006 (2011).

193. C. A. Lieber and A. Mahadevan-Jansen, "Automated method for subtraction of fluorescence from biological Raman spectra," Appl. Spectrosc. **57**, 1363-1367 (2003).

194. A. Mahadevan-Jansen and R. Richards-Kortum, "Raman spectroscopy for the detection of cancers and precancers," J. Biomed. Opt. **1**, 31-70 (1996).

195. C. Reble, I. Gersonde, C. A. Lieber, and J. Helfmann, "Influence of tissue absorption and scattering on the depth dependent sensitivity of Raman fiber probes investigated by Monte Carlo simulations," Biomed. Opt. Express **2**, 520-533 (2011).

196. C. M. Krishna, J. Kurien, S. Mathew, L. Rao, K. Maheedhar, K. K. Kumar, and M. V. Chowdary, "Raman spectroscopy of breast tissues," Expert Rev. Mol. Diagn. **8**, 149-166 (2008).

197. A. S. Haka, Z. Volynskaya, J. A. Gardecki, J. Nazemi, R. Shenk, N. Wang, R. R. Dasari, M. Fitzmaurice, and M. S. Feld, "Diagnosing breast cancer using Raman spectroscopy: prospective analysis," J. Biomed. Opt. **14**, 054023 (2009).

198. B. Krishnapuram, L. Carin, M. A. Figueiredo, and A. J. Hartemink, "Sparse multinomial logistic regression: fast algorithms and generalization bounds," IEEE Trans. Pattern Anal. Mach. Intell. **27**, 957-968 (2005).

199. B. H. Yeap, S. Muniandy, S. K. Lee, S. Sabaratnam, and M. Singh, "Specimen shrinkage and its influence on margin assessment in breast cancer," Asian J. Surg. **30**, 183-187 (2007).

200. L. G. Wilke, J. Q. Brown, T. M. Bydlon, S. A. Kennedy, L. M. Richards, M. K. Junker, J. Gallagher, W. T. Barry, J. Geradts, and N. Ramanujam, "Rapid noninvasive optical imaging of tissue composition in breast tumor margins," Am. J. Surg. **198**, 566-574 (2009).

201. F. T. Nguyen, A. M. Zysk, E. J. Chaney, J. G. Kotynek, U. J. Oliphant, F. J. Bellafiore, K. M. Rowland, P. A. Johnson, and S. A. Boppart, "Intraoperative evaluation of breast tumor margins with optical coherence tomography," Cancer Res. **69**, 8790-8796 (2009).

202. J.-F. Delorme, G. Ma, F. Lesage, F. Leblond, and A. Benyamin-Seyar, "Full path Monte Carlo simulation of fluorescence in non-voxelized complex heterogeneous mouse model," Proc. SPIE Int. Soc. Opt. Eng. **6854**, 68541M (2008).

203. R. H. Wilson, V. Schweller, and M.-A. Mycek, "User-friendly Monte Carlo code for time-resolved fluorescence models of tissues with irregular interfaces," Biomedical Optics 2010 Technical Digest (Optical Society of America), BME8 (2010).

204. R. H. Wilson, L.-C. Chen, W. Lloyd, S. Kuo, C. Marcelo, S. E. Feinberg, and M. A. Mycek, "Mesh-based Monte Carlo code for fluorescence modeling in complex tissues with irregular boundaries," Proc. SPIE Int. Soc. Opt. Eng. **8090**, 80900E (2011).

205. W. R. Lloyd, R. H. Wilson, L.-C. Chen, G. D. Gillispie, and M.-A. Mycek, "Fluorescence wavelength-time matrix acquisition for biomedical tissue diagnostics," Proc. SPIE Int. Soc. Opt. Eng. **8087**, 80870Y (2011).

206. T. Li, Q. Luo and H. Gong, "MCVM: Monte Carlo modeling of photon migration in voxelized media," J. Innov. Opt. Health Sci. **3**, 91-102 (2010).

207. R. M. Valentine, C. T. A. Brown, K. Wood, H. Moseley, and S. Ibbotson, "Monte Carlo modeling of *in vivo* protoporphyrin IX fluorescence and singlet oxygen production during photodynamic therapy for patients presenting with superficial basal cell carcinomas," J. Biomed. Opt. **16**, 048002 (2011).

208. K. Izumi, S. E. Feinberg, A. Iida, and M. Yoshizawa, "Intraoral grafting of an *ex vivo* produced oral mucosa equivalent: a preliminary report," Int. J. Oral Maxillofac. Surg. **32**, 188-197 (2003).

209. K. Izumi, J. Song, and S. E. Feinberg, "Development of a tissue-engineered human oral mucosa: from the bench to the bed side," Cells Tissues Organs **176**, 134-152 (2004).

210. L.-C. Chen, W. R. Lloyd, R. H. Wilson, S. Kuo, C. L. Marcelo, S. E. Feinberg, and M.-A. Mycek, "Nonlinear optical molecular imaging enables metabolic redox sensing in tissue-engineered constructs," Proc. SPIE Int. Soc. Opt. Eng. **8089**, 80890J (2011).